MAX-PLANCK-INSTITUT FÜR RADIOASTRONOMIE
BONN

Understanding the impact of massive star formation on its surroundings in Messier 8

Dissertation

zur

Erlangung des Doktorgrades (*Dr. rer. nat.*)

der

Mathematisch-Naturwissenschaftlichen Fakultät

der

Rheinischen Friedrich-Wilhelms-Universität, Bonn

vorgelegt von
Maitraiyee TIWARI
aus
Bhopal, India

Bonn 2019

Angefertigt mit Genehmigung der Mathematisch-Naturwissenschaftlichen Fakultät
der Rheinischen Friedrich–Wilhelms–Universität Bonn
Prepared with the permission from the Faculty of Mathematics and Natural Sciences of the University of Bonn

1. Referent: Prof. Dr. Karl M. Menten
2. Referent: Prof. Dr. Pavel Kroupa
Tag der Promotion: 28^{th} January, 2020
Erscheinungsjahr: 2020

Abstract

by Maitraiyee Tiwari

for the degree of

Doctor rerum naturalium

Massive stars inject an immense amount of energy into their surroundings, which affect the physics and chemistry of the interstellar medium (ISM). Massive stars play a significant role in the evolution of galaxies. The best laboratories to study the effects of massive stars on their surrounding medium are massive star-forming regions. The emission of the UV and FUV photons from massive stars give rise to hot ionised HII regions and warm photodissociation regions (PDRs), respectively. PDRs comprise the neutral atomic gas and most of the molecular gas in the galaxies, where FUV photons dominate the heating and regulate the chemistry. With the advent of high resolution observing facilities in the Far-Infrared (FIR) and (sub)millimeter (submm) wavelengths, we are now able to study PDRs in great detail. Cooling in PDRs occurs mainly through the fine structure lines of [C II], [O I] and through rotational transitions of CO, which are observable at FIR and submm wavelengths.

Interaction of FUV photons with different chemical species in the vicinity of massive stars results into a rich hydrocarbon chemistry and the formation processes of the observed small hydrocarbons (species like C_2H and c-C_3H_2, observable at submm wavelengths) in PDRs can be understood by comparing the observational data with the PDR modeling results.

Messier 8 (M8) is one of the brightest massive star-forming regions known in our galaxy and it hosts high-UV flux PDRs and HII regions. We performed a detailed survey toward M8, using the world's leading FIR and submm wavelength observing facilities, the Institut de Radioastronomie Millimétrique (IRAM) 30 m, the Atacama Pathfinder EXperiment (APEX) 12 m and the Stratospheric Observatory for Infrared Astronomy (SOFIA). We were able to quantify the physical conditions of the PDR of M8 and of the gas in the star-forming region of M8 east. From the kinetic information obtained from our data sets and from the ancillary data, we explored the morphology of the region around the bright ionising stellar system of M8. We found that gas phase chemistry is responsible for the observed hydrocarbon abundances in M8. Furthermore, a more embedded star formation is taking place in M8 E compared to M8.

Acknowledgements

As I am about to submit my thesis and this exciting journey of my PhD will soon come to an end, I would like to thank everyone for making this possible.

First and foremost, I want to thank Prof. Dr. Karl Menten, who gave me the opportunity to be a part of his research group. He trusted me with the responsibility to work on one of his scientific ideas and this thesis is a result of that. His passion for science and constant guidance has encouraged me to do better. Although I might seem intimidated by him, but I've always found comfort in his extremely caring and impartial nature.
A special thanks goes to my supervisor, Dr. Friedrich Wyrowski, who guided me at every step of my journey from learning the basics of radio astronomy to finishing this thesis. He always had suggestions and answers to all of my scientific ideas and questions (regardless of how silly they were). I absolutely enjoyed our observing sessions at APEX.
Next, I would like to thank Dr. J. P. Pérez-Beaupuits and Dr. Min Young Lee for always being friendly and giving me constructive feedback to reach my goals.
I would like to thank Dirk for always having a solution to all my IT problems.
Thanks to Eva, Le and Barbara for helping me deal with the German bureaucracy.

I had a great time living in Bonn and it's mainly because of the friends I made. I thank my closest friends (alphabetically): Fateme for always understanding me, Hans for being the best roommate, Joseph for being so caring and supporting me in every way he could, Laura for always being ready with a plan to explore nature, Laure for reminding me that wine is the ultimate solution to everything, and Wonju for always checking up on me, no matter the distance.
Thanks to Marion and Manali for happily indulging in long hours of discussions on everything under the sun.
I also want to thank Eric, Nabhojeet, Alexandra, Devina, Nina, Ka Tat, Emilio, Mahasweta, Tobi, Gül, Eleni, Shampa, Prajwal, Ripunjay, Arshia, Carsten, Richa and Michael for making my time in Bonn an enjoyable one.
I thank Gautam for always being by my side and for reminding me that there is always something to laugh about. Thanks for helping and motivating me to finish my thesis on time (a week late). Most importantly, thanks for your patience!

Finally, I thank my family and Arpita for their selfless love and their support in every possible way to help me pursue my dreams. Words can't express my gratitude to them.

List of publications related to this PhD thesis

1. **Unveiling the remarkable photodissociation region of Messier 8**

   M. Tiwari, K. M. Menten, F. Wyrowski, J.P. Pérez-Beaupuits, H. Wiesemeyer, R. Güsten, B. Klein and C. Henkel, A&A 615, A158 (2018)

   DOI: 10.1051/0004-6361/201732437 [arXiv:1803.10164]

2. **Observational study of hydrocarbons in the bright photodissociation region of Messier 8**

   M. Tiwari, K. M. Menten, F. Wyrowski, J.P. Pérez-Beaupuits, M.-Y. Lee and W.-J. Kim, A&A 626, A28 (2019)

   DOI: 10.1051/0004-6361/201834567 [arXiv:1903.10444]

Contents

List of Figures

List of Tables

Chapter 1

Introduction

1.1 Stars and the interstellar medium

Stars are glowing masses of gas, radiating their internal energy and are held together under their own gravity. The process of nucleosynthesis occurring in a star's core produces an immense amount of energy that facilitates more reactions, producing heavier elements. Hence, stars are the building blocks of galaxies. Stars form in the dense interstellar medium, in molecular clouds, parts of which collapse under their own gravity. The newly formed stars feed back energy and momentum into their surroundings. Stars are classified based on their masses mainly as low mass ($M < 8\ M_\odot$, where $M_\odot$ is solar mass) and high mass (so-called massive, $M > 8\ M_\odot$) stars (Shu et al. 1999 & Zinnecker & Yorke 2007). The 8 $M_\odot$ limit decides the fate of a star. The upper mass limit for a star that will go on to form a white dwarf (death of a low mass star) rather than a neutron star (death of a massive star) is about $\sim 8\ M_\odot$. Low mass stars have a longer formation time scale and a longer lifetime compared to massive stars, for example Sun is supposed to survive for 10 billion years compared to a few million years of a massive star.

In a galaxy like the Milky Way, the stars contribute most to its baryonic mass (Kippenhahn et al., 2012) but occupy only a very small fraction of the volume. To put it simply, everything that is between the stars is interstellar medium (ISM). It has a low density and comprises 99% of gas (mainly hydrogen and helium, which are also the most abundant elements in stars) and the remaining 1% of dust. Dust is made up of heavier elements, which are released by stars into the ISM. Species contributing to the gas and dust composition can be neutral, ionised or in molecular form that is in gaseous or in solid state (dust), depending on the excitation conditions of the medium. The number density of the ISM is so low that for our Galaxy, there is $\sim$ 1 gaseous atom per cm^3 and $\sim$ 100–1000 dust grains per km^3. Despite its low density, the ISM covers a huge volume of space and hence has a substantial mass.

1.2 Nebulae

Giant clouds, known as nebulae, are sites of highly concentrated interstellar material. Here, the density of gas and dust may be much higher than the average by as much as a thousand times or more, depending on the physical properties, distribution, volume

filling factor, morphology, physical processes and the interaction with the stellar component. Some nebulae are formed from the gas and dust expelled out by the explosion of a dying star (known as a supernova explosion), while other nebulae are sites of star-formation. If a nebula is close to a star that is emitting ultraviolet (UV) radiation, its gas gets heated up to $\sim$ 10,000 K. At such high temperatures, the hydrogen gas gets excited and starts to glow. Such a nebula is called an emission nebula, e.g. the Orion Nebula. When the star is not hot enough or the nebula is farther away from it, the radiation from the star could be blocked or reflected. If the nebula's dust grains reflect the starlight, it is called a reflection nebula, e.g. NGC 1999, a nebula in the constellation Orion. While if the nebula's dust is optically thick (i.e. a photon gets absorbed while passing through the medium), the clouds do not glow and hence this nebula is called a dark nebula, e.g. the Horsehead Nebula.

1.3 Massive star formation

In order to present the work done in this thesis, we will focus on massive stars and their formation process.

The effect of massive stars on their surroundings is immense. They play a major role in the evolution of the galaxies through their energy output, ionizing radiation, supernovae explosions and heavy element enrichment (Kennicutt, 2005). The structure and chemical composition of the ISM gets changed by the injection of radiative and mechanical energy from the stars. The evolution of star formation is regulated by massive stars by either halting the process or by triggering it. Stellar winds can lead to the formation of cloud and intercloud phases by fragmenting the molecular clouds, resulting in halting of star formation, called negative feedback. On the other hand, the shocks that are induced from photoionization of the medium around massive stars, compress the surroundings, setting off star formation, called positive feedback (Urquhart et al. 2007 & Kim et al. 2013). An evolutionary sequence of star formation is presented in Fig. 1.1 and the evolutionary stages that are important pertaining to this work are described below.

1.3.1 Giant molecular clouds

Star formation takes place in dense concentrations of interstellar gas and dust i.e. molecular clouds. In particular, Giant Molecular Clouds (GMCs) have been identified as ideal sites for massive star formation (Zuckerman & Evans, 1974). Both agglomeration and self-gravity are believed to be responsible for the formation of GMCs, such that self-gravity dominates giving rise to disc structure when surface density increases (Dobbs, 2008). Bronfman et al. (2000) showed that at large scales, the radial distribution of massive star formation follows the molecular gas distribution in the inner Galactic disk at all galactocentric radii. GMCs have radii ranging from 10–160 pc, velocity widths of 1–10 kms^{-1} and have masses $\sim$ 10^4–10^7 M$_\odot$. These regions have extremely cold temperatures of about $\sim$ 10–20 K, where atomic gas

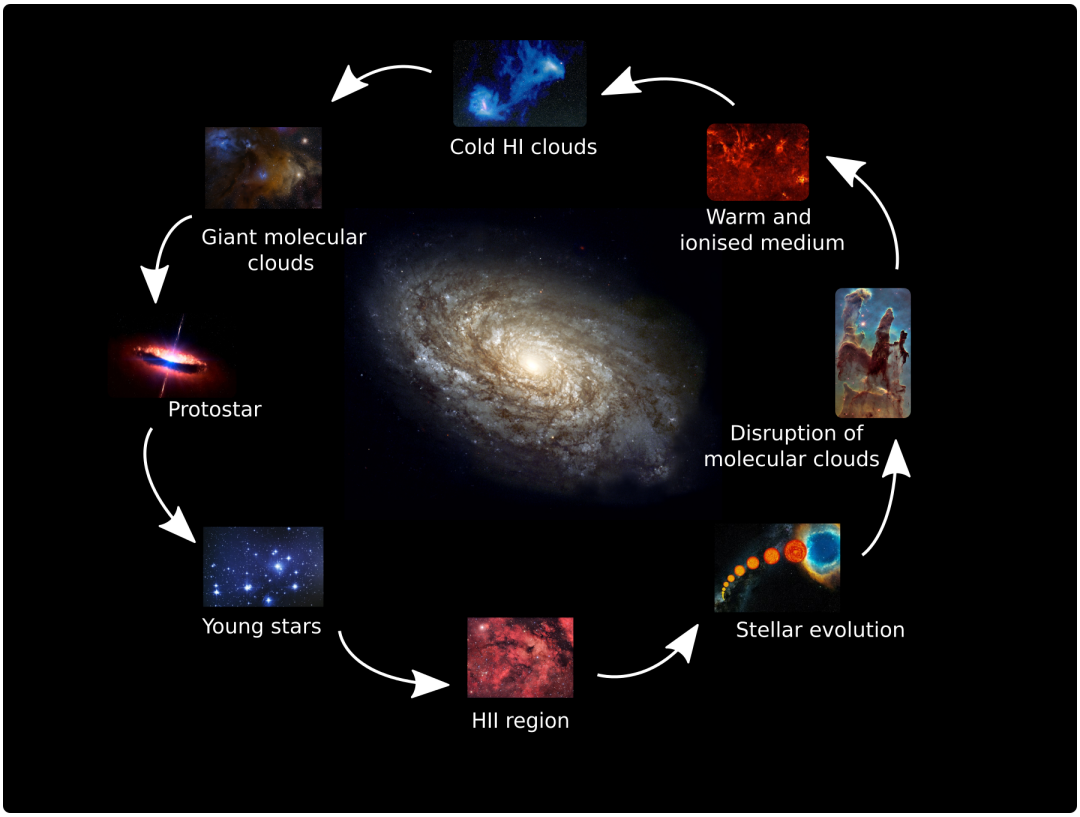

Figure 1.1: The different evolutionary stages of massive star formation and stellar feedback.

becomes molecular. CO and H_2 are the most common molecular cloud tracers.

Many galactic surveys of dust continuum tracing the cold, optically thin dust: the Bolocam Galactic Plane Survey (BGPS, 1.1 mm continuum survey, Ginsburg et al. 2013), APEX Telescope Large Area Survey of the GALaxy (ATLASGAL, 870 μm continuum survey, Schuller et al. 2009) and the Herschel Infrared Galactic Plane Survey (Hi-GAL, photometric imaging survey at 70, 160, 250, 350, and 500 μm, Molinari et al. 2010) also suggest that massive stars and stellar clusters form in cold, high density clouds.

Furthermore, massive stars are also believed to be formed in a special class of cold dense molecular clouds called the infrared dark clouds (IRDCs), which are defined as regions of high extinction observed against the bright, diffuse infrared (IR) emission from the Galactic background (Rathborne et al. 2006 & Battersby et al. 2014). Several dust continuum observations found that the IRDCs have cold temperatures (< 20 K), contain dense ($n > 10^5$ cm^{-3}) dust cores with sizes (< 0.1 pc, 1 pc $= 2.1 \times 10^5$ astronomical units $= 3.1 \times 10^{16}$ m), which are suitable conditions for star formation (Rathborne et al. 2006 & Fallscheer et al. 2009). At these conditions, the cloud cores

exceed the Jeans limit (for a cloud core to collapse, $M_{core} > \left(\frac{5k_BT}{Gm}\right)^{3/2}\left(\frac{3}{4\pi\rho}\right)^{1/2}$), implying that they are created by turbulent fragmentation rather than thermal fragmentation. Typical mass of such cores is $\sim 10^4$ $M_\odot$ and they collapse to fragment into denser clumps.

1.3.2 Protostars

Dense cores (size $\sim$ 0.1 pc and mass $\sim$ 10–50 $M_\odot$) evolve to become protostars and the whole process takes $\sim 10^6$ years. Protostars have higher gas temperatures, broader spectral line widths of the molecular emission and detection of many more distinct molecular species compared to their previous evolutionary stage. It is indicative of the development of a characteristic hot core chemistry as a growing massive protostar heats its surroundings (Beuther et al. 2009 & Zhang et al. 2009). Gas and dust accrete onto the protostar in form of a rotating disk. Usually a bipolar molecular outflow is produced with a strong protostellar wind resulting from the strong magnetic field generated from the rotating molecular material around the protostar.

The molecules that were formed in the ice mantles of dust grains during the prestellar phase and the warming-up period of the protostellar phase, sublimate from the high kinetic temperatures (150–200 K) of the hot cores. Both the high temperatures and high densities lead to the formation and detection of numerous complex organic molecules (Belloche et al., 2016). A complex organic molecule (COM) is an organic molecule with six atoms or more (Herbst & van Dishoeck, 2009). One of the fundamental goals of astrochemistry is to understand how, when, and where COMs (potential prebiotic molecules) are formed, which is also an integral part of the origin of life. Regions around protostars are ideal sites to study the formation and destruction process of these COMs. Several studies have been performed in millimeter (mm) and submillimeter (submm) wavelengths toward several hot cores (e.g. van der Wiel et al. 2019 & Csengeri et al. 2018) to understand the role they play in star formation and also to explore the rich chemistry which they give rise to.

1.3.3 HII regions

Massive stars reach very high stellar temperatures when they begin core nuclear-burning and emit UV radiation (photons with $h\nu > 13.6$ eV), which are energetic enough to ionize H (HI) $\rightarrow H^+$ (HII), around them, giving rise to HII regions. Moreover, massive stars affect the ISM through stellar feedback and one such process is to inject energy by the emission of UV radiation into their surrounding medium playing an important role in the formation and evolution of HII regions. Usually HII regions have temperatures $\sim 10^4$ K, high pressures and large thermal velocities such that they expand into their surrounding medium by destroying and disrupting molecular clouds that are gravitationally bound (Hollenbach & Tielens, 1999). Kurtz & Franco (2002) classified HII regions based on their physical parameters: hypercompact (size $\sim$

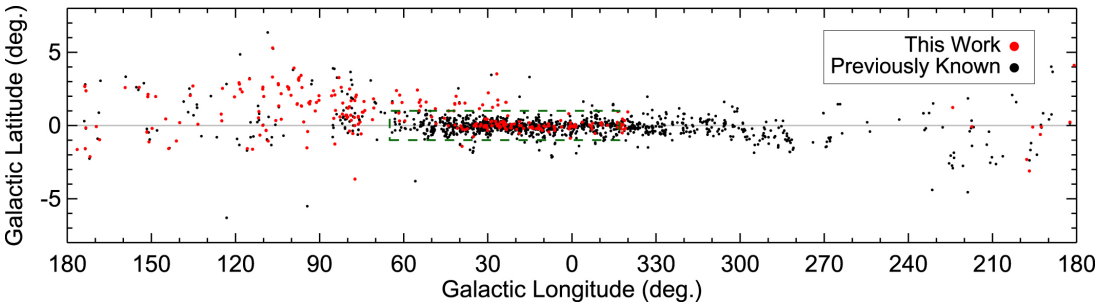

Figure 1.2: Galactic distribution of all of the newly detected (in red) and previously known (in black) HII regions as reported by Anderson et al. (2015). The previously known HII regions are taken from Anderson et al. (2014) and that covered area is shown within the green dashed box, while the new detections were a part of the Green Bank Telescope hydrogen radio recombination line and radio continuum survey performed in the 3 cm band.

0.003 pc, n $\gtrsim 10^6$ cm^{-3}), ultracompact (UC) (size $\lesssim$ 0.1 pc, n $\gtrsim 10^4$ cm^{-3}), compact (size $\lesssim$ 0.5 pc, n $\gtrsim 5 \times 10^3$ cm^{-3}), classical (size $\sim$ 10 pc, n $\sim$ 100 cm^{-3}), giant (size $\sim$ 100 pc, n $\sim$ 30 cm^{-3}) and supergiant (size $>$ 100 pc, n $\sim$ 10 cm^{-3}). In our galaxy, the larger HII regions (classical and giant), have structures that are diffuse, irregular and contain low excitation filaments and condensations. On the other hand, the smaller HII regions (UC and hypercompact) are believed to be excited by newly formed massive stars (early on, they might still be accreting material from their surroundings, Keto et al. 2008) and are found in regions of high visual extinction. They can have spherical, bipolar, cometary, core-halo and shell-like structures. Lastly, the intermediate sized HII regions (so-called compact HII regions) are assumed to represent a later phase of evolution of the UC and hypercompact HII regions. They usually have spheriodal morphology (Phillips & Ramos-Larios, 2008). A wide range of physical processes are responsible for the formation of HII regions. The inner part of an HII region is formed when protostars or newly formed massive stars ionize the dense molecular gas. The interaction between stellar winds and exterior neutral molecular envelopes gives rise to shocks. The molecular shells which surround these regions have gas temperatures in the range 20–100 K (Turner et al., 1998).

1.3.3.1 Locating HII regions

HII regions are the most luminous objects in the galaxy at radio and infrared (IR) wavelengths, and are detected across the entire galactic disk. It is believed that detection of an HII region unambiguously locates massive star formation. The thermal bremsstrahlung and radio recombination lines (RRL) are responsible for HII regions' emission at radio wavelengths. The thermal bremsstrahlung from an HII region is termed free-free emission. It is produced by free electrons, which get scattered from interaction with ions while not being captured. The electrons are free both before and after the interaction and hence the name. An HII region consists of an ionised

plasma of hydrogen and other ions that recombine with free electrons. After the recombination, the electrons are still in highly excited states and energy is emitted when they step down the energy ladder. Emission at low quantum numbers give rise to optical and near-IR recombination lines, while at higher quantum numbers the spacing between energy levels decreases and the photon emitted due to such a recombination line transition will be at radio wavelengths. Therefore, the recombination lines with high quantum numbers (close to 100) are called RRLs.

RRLs provide information about the velocity of the nebula and their kinematic distances, which can then place the HII regions onto the galactic plane tracing the structure of the galaxy (Anderson & Bania, 2009). Free-free emission from the HII regions is measured by radio continuum observations, which provide us with the radio flux and the angular size. Combined together with the distance estimates, these parameters give a luminosity (constraining the spectral type of the ionizing star) and a physical size (informing about the type of HII region) (Anderson et al., 2011). Electron temperatures of HII regions can be estimated from line-to-continuum ratios, which measure the turbulent and thermal energies in the HII regions.

Radio continuum observations of the Milky Way started in the 1950s and most of the bright, discrete radio continuum sources were thermally emitting HII regions (Westerhout, 1958). Hoglund & Mezger (1965) detected the first unambiguous RRL (H 109 α) emission from M17 and Orion A. Since galactic ISM is optically thin at radio wavelengths, RRL surveys were able to detect large numbers of HII regions spread throughout the entire galactic disk and play an important role in exploring the galactic structure and the spatial distribution of massive star formation (Hoglund & Mezger 1965, Wilson et al. 1970, Reifenstein et al. 1970, Downes et al. 1980, Lockman 1989 & Lockman et al. 1996). Recent developments in instrumentation and telescope construction lead to a more precise census of galactic HII regions. Bania et al. (2010) & Anderson et al. (2011) used the high spectral sensitivity offered by the NRAO Green Bank Telescope (GBT), to provide a catalog of the measured properties of the RRl and continuum emission from Galactic HII regions. Relatively newer surveys like THOR (The HI/OH/Recombination line survey of the Milky Way, Beuther et al. 2016) and GLOSTAR (GLObal view onSTAR formation in the Milky Way galaxy, Brunthaler et al. in prep.) use the Karl G. Jansky Very Large Array (VLA) telescope to observe several RRLs and radio continuum. Besides their main goal of studying the star-forming regions, both THOR and GLOSTAR surveys help us in identifying HII galactic regions and to understand their dynamics.

The radiation from the ionising source of an HII region is absorbed by local dust, which thermally gets re-emitted at IR wavelengths. In order to find UC HII regions, Wood & Churchwell (1989) & Hughes & MacLeod (1989) used flux ratio colours from the InfraRed Astronomical Satellite (IRAS) point-source catalog (Beichman, 1988). The MIPSGAL survey of the inner Galactic plane using the Multiband Infrared Photometer for Spitzer aboard the Spitzer Space Telescope (MIPSGAL,

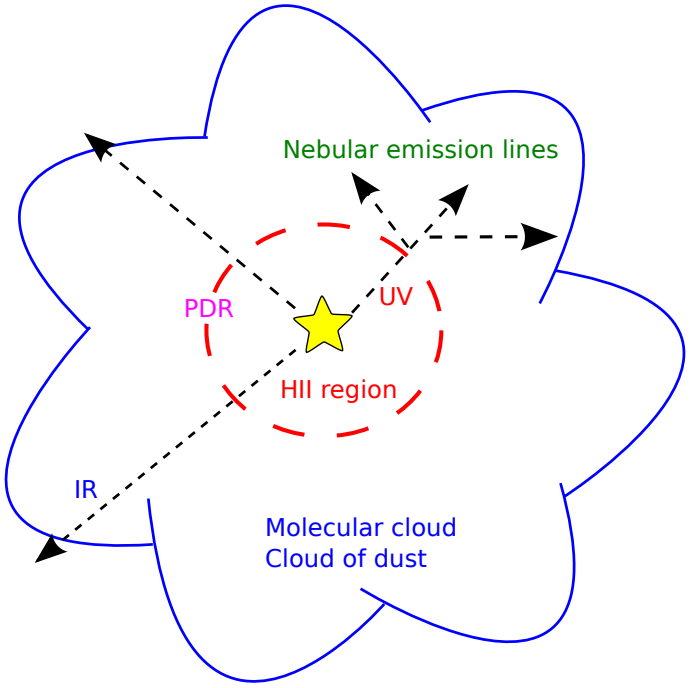

Figure 1.3: Sketch presenting the HII region, PDR and the molecular clouds around an ionising source.

Carey et al. 2009) observes the 24 μm dust continuum in mid IR, which is found to be a direct tracer of the HII regions. The spatial distribution of the mid IR emission coincides very well with the free-free thermal emission at radio wavelengths. This is because the hot plasma that gives rise to the free-free emission is ionised by the same source, which is responsible for the IR emission. It is also coincident with 21 cm radio continuum emission Benjamin et al. 2003) emission (Anderson et al., 2011). WISE (Wide-Field Infrared Survey Explorer, Wright et al. 2010) data maps the entire sky in four photometric bands: 3.4 μm, 4.6 μm, 12 μm, and 12 μm, among which the 12 μm band of WISE contains emission from polycyclic aromatic hydrocarbons (PAHs) at 11.2 μm and 12.7 μm (Tielens, 2008) and the WISE 22 μm band is similar to the MIPSGAL 24 μm band, hence WISE can trace HII regions.

A complete galactic distribution of detected HII regions (taken from Anderson et al. 2015) is shown in Fig. 1.2.

1.4 Photodissociation regions

Photodissociation regions (PDRs) are neutral regions of the ISM that lie between the HII regions and the cold molecular cloud shielded from the illuminating star/ protostar (Hollenbach & Tielens, 1999). Figure 1.3 is a sketch presenting a simplistic view of how the illuminating source gives rise to HII regions and PDRs. In PDRs, the thermal and

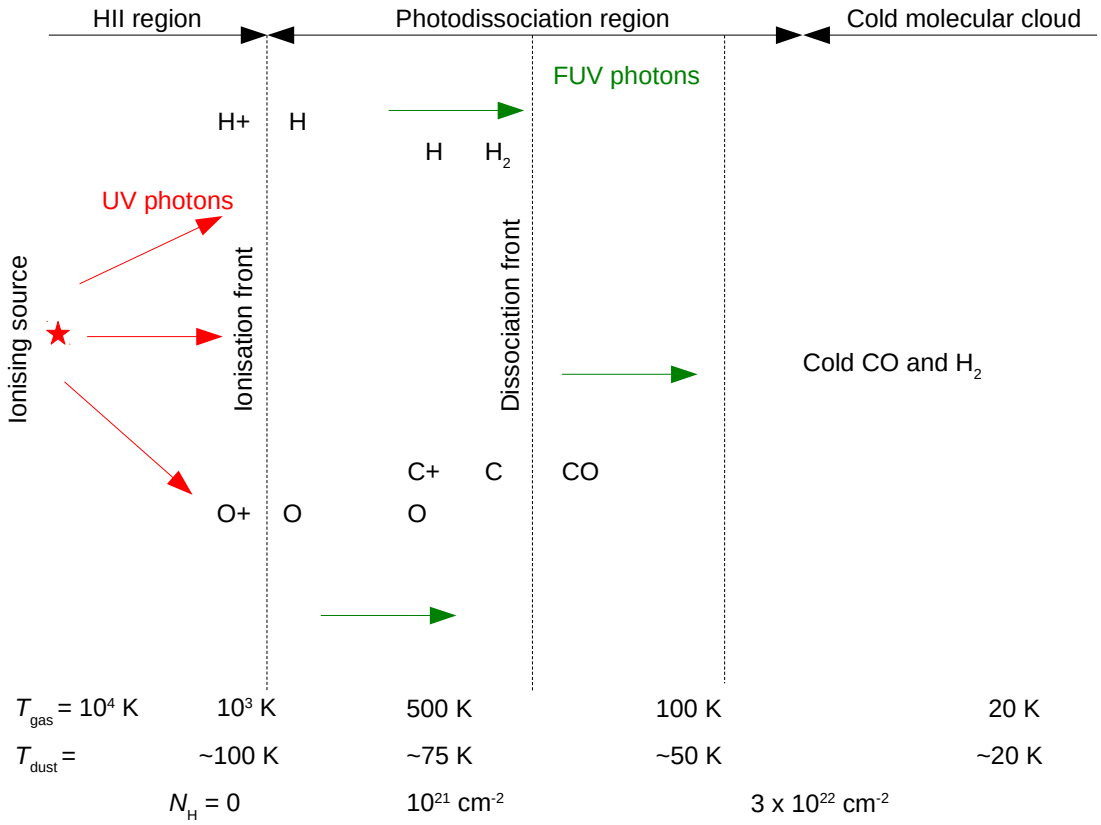

Figure 1.4: Structure of a PDR adapted from Hollenbach & Tielens (1999) & Goicoechea et al. (2016). Radiation is incident from the left.

chemical processes are regulated by the far-UV (FUV) radiation (6 eV $<$ hν $<$ 13.6 eV, 6 eV is the work function of most of the metals taking part in the photoelectric heating of a PDR and 13.6 eV is the ionisation energy of H). The most widely distributed general diffuse ISM consisting of diffuse and translucent interstellar clouds is by definition a PDR. Even in dense molecular clouds (A_ν $<$ 8), the FUV photons still influence the chemistry and physics through ionisation of trace species. Hence, the study of HII regions and PDRs is the study of the structure, chemistry, thermal balance and evolution of the ISM (Tielens, 2010). These regions are interfacing between regions of still dust embedded star formation and newly formed energetic young stars. Most of the mass of the ISM resides in the neutral regions i.e. in the cold neutral medium or in the dense molecular clouds, where star formation takes place. Observational and theoretical studies of PDRs allow us to understand the radiation-induced feedback mechanisms, which can explain the formation and destruction of star-forming molecular clouds and how they regulate the star formation rates and the gas column densities in giant molecular clouds (described in detail in Hollenbach & Tielens 1999).

1.4.1 Characterisation of a PDR

Figure 1.4 shows the 1D structure of a PDR. The ionising source, a massive star or a massive protostar, emits radiation from the left. The emitted UV photons are energetic enough to ionise the H and O atoms. The transition from the warm atomic gas to the ionised gas occurs at the ionisation front, which has temperatures as high as $T_{\rm gas} = 10^4$ K and $T_{\rm dust} = 100$ K. It is the FUV photons that dissociate the H_2 and CO molecules to H, C and O; and this transition of molecular gas to the atomic gas occurs at the dissociation front ($T_{\rm gas} = 500$ K and $T_{\rm dust} = 75$ K). FUV photons also ionise the C [C I] $\rightarrow$ C^+ [C II] (ionisation energy of carbon = 11.3 eV). As the flux of the dissociating photons is attenuated, the gas composition is dominated by H_2 and deep into the molecular cloud ($T_{\rm gas} = 20$ K and $T_{\rm dust} = 20$ K), the carbon-ionising flux gets reduced and C^+ recombines with O to form CO.

The two major mechanisms responsible for the heating in PDRs are, firstly, the photoelectric effect on PAHs and small dust grains, and secondly, the photopumping of H_2 molecules followed by collisional deexcitation (Tielens, 2010). Cooling in PDRs occurs mainly through far-IR [C II] and [O I] fine structure lines, which absorb most of the FUV flux at the PDR surface. In PDRs, [C II] is the dominant cooling line at relatively low densities and FUV radiation field ($n \leq 10^4$ cm^{-3}, $G_0 \leq 10^4$), while at higher densities and FUV radiation field ($n \geq 10^4$ cm^{-3}, $G_0 \geq 10^4$), [O I] becomes the dominant cooling line. The other cooling lines are [C I] and molecular rotational lines, particularly of CO and H_2 (Hollenbach & Tielens, 1999). Hence, these species (mainly [C II] and [O I]) characterise a PDR.

The FUV radiation field penetrating deep into the molecular clouds, gets attenuated mainly by absorption on dust grains. This gives rise to a layered structure of various chemical transitions, called as chemical stratification (Simon et al., 1997). Chemical stratification is observed in many different PDRs (e.g. in the Orion Bar, Tielens & Hollenbach 1985 and M 17 Pérez-Beaupuits et al. 2012), which have also been found to be clumpy (Stutzki et al., 1988) and show spatial coexistence of different PDR tracers. Their geometries indicate the presence of fractal surfaces throughout the region, which is a result of exposure to FUV radiation deep within the molecular clouds.

1.4.2 Chemistry in PDRs

Heating in PDRs cause the gas to heat up from 85 K (interclump, Hogerheijde et al. 1995) to $>$ 500 K (dissociation front, van der Werf et al. 2013). When the collisional deexcitation of vibrationally excited H_2 dominates the heating, the temperatures at the surface of dense clumps (extinction coefficient, $A_{\rm v} < 1$) can go $>$ 1000 K (Burton et al., 1990). In presence of hot FUV excited gas, the vibrationally excited H_2 allows reactions that are highly endothermic and with large activation barriers to proceed quickly, hence setting off a distinctive chemistry (Agúndez et al., 2010). Formation of CH^+, OH and SH^+ takes place when H_2 reacts with C^+, O and S^+, which are all

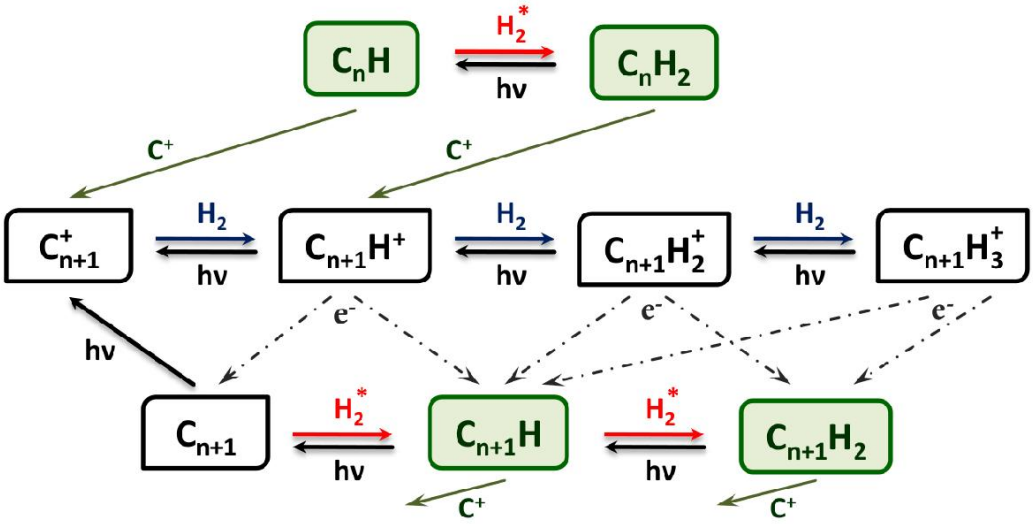

Figure 1.5: Network of small hydrocarbons including their main gas-phase formation and destruction reactions predicted by Meudon code (Le Petit et al. 2006 & Le Bourlot et al. 2012) for the Orion Bar, taken from Cuadrado et al. (2015, Fig. 16). Red arrows indicate the reactions with activation energy barriers and the blue arrows for barrierless hydrogenation reactions.

quite abundant in PDRs. Also, carbon bearing radicals like CN, C_2H, c-C_3H_2, HC_3N have been detected in PDRs since 1990s (Jansen et al. 1995 & Fuente et al. 1996). A network of small hydrocarbon chemistry for the Orion Bar PDR is shown in Fig. 1.5.

In addition to the above mentioned simple molecules, Guzmán et al. (2014) & Gratier et al. (2013) detected COMs like HCOOH, CH_2CO, CH_3CN, CH_3OH, CH_3CHO, and CH_3CCH, in the PDR of the Horsehead Nebula, which is a low UV-flux PDR with ($G_0 \leq 100$). In PDRs with high UV flux ($G_0 \geq 10^4$) like the Orion Bar, more than 250 transitions from various COMs and related organic precursors (with upto seven atoms) are detected (Cuadrado et al., 2017). The formation of COMs in PDRs is still not understood but their high abundances in various environments suggest a complicated relation between gas and grain surface chemistry.

1.5 Messier 8

Messier 8 (M8), the Lagoon Nebula, hosts one of the brightest HII regions and PDRs in our galaxy, located in the Sagittarius-Carina arm, near our line of sight toward the Galactic Center. It is situated at $\sim$ 1.25 kpc (such that $1'$ corresponds to 0.36 pc) away from the Sun (Damiani et al. 2004 & Arias et al. 2006) and is about 34 $\times$ 12 pc in diameter. The error on the distance estimate is $\sim$ 0.1 kpc (Tothill et al., 2008). Figure 1.6 shows M8 in both optical and submm wavelengths. M8 consists of a rich open cluster, NGC 6530, with several O stars and about

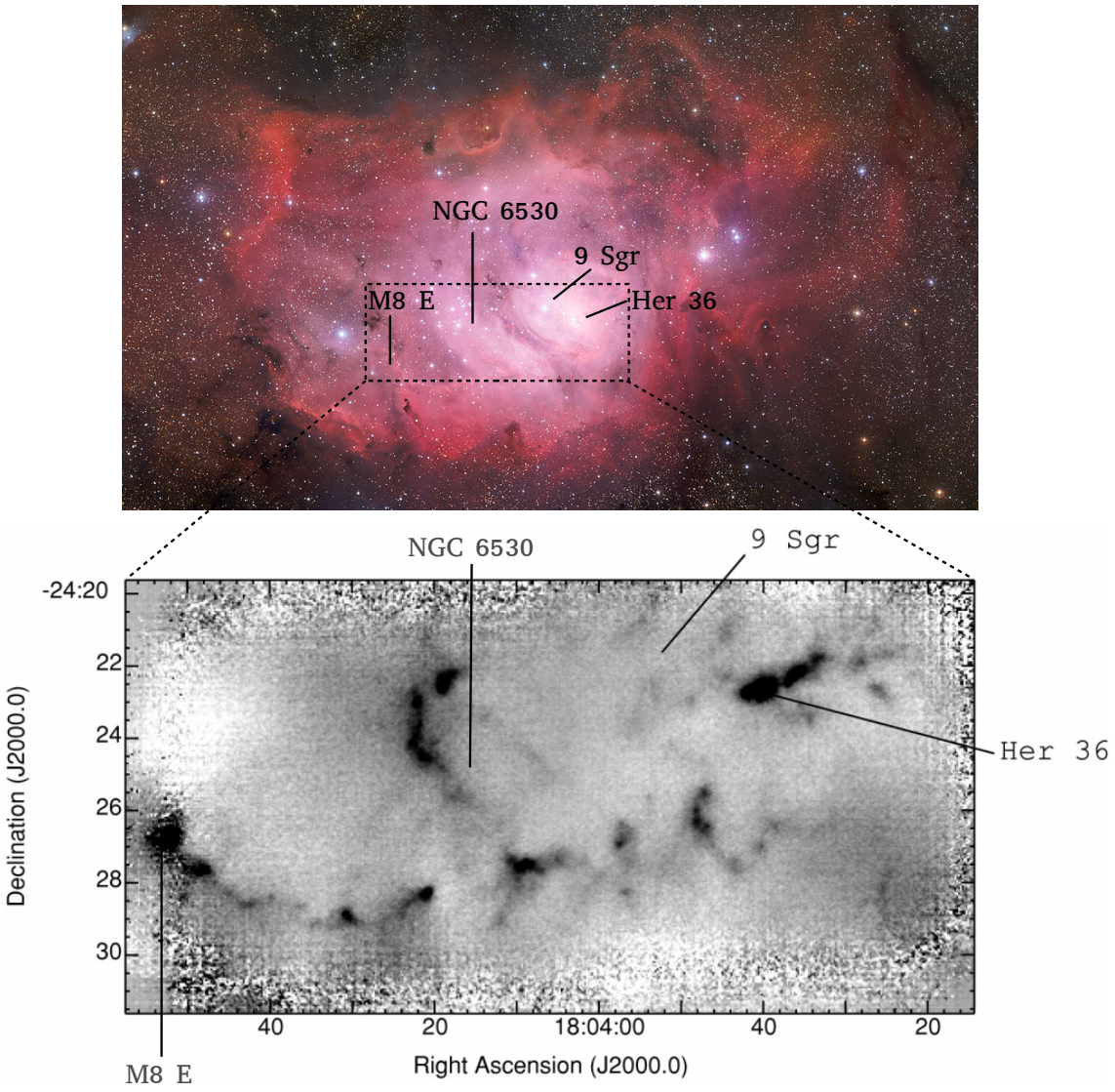

Figure 1.6: Upper panel: Image of M8 taken with Wide Field Imager (WFI) attached to the MPG/ESO 2.2 m telescope at the La Silla Observatory. The image is based on the maps observed by using three different broadband filters: B (at $\sim$ 456.252 nm), V (at 539.562 nm), R (at 651.725 nm) and one narrow-band filter: H α (at 658.827 nm). Lower panel: Single-beam map of M8 at 450 μm adopted from Tothill et al. (2002, Fig. 2). The bright stellar systems (Her 36 and 9 Sgr) of the central bright region of M8 are marked along with the eastern (M8 E) star forming region of M8.

60 B stars. It is centered on R.A. (α, J2000) = $18^h04^m24^s$ and Dec. (δ, J2000) = $-24°21'12''$ and has a radius of $\sim 30'$, while the core radius is $\sim 4'$ (Chen et al., 2007). In the west of this core lies an IR dark structure called the elephant trunk, which surrounds an HII region lying further in the west. The eastern half of the HII region is illuminated by 9 Sagitarri (9 Sgr), which is a stellar system consisting of an O3.5 V primary and an O5-5.5 V secondary (Rauw et al., 2012). The western half of the HII region is powered by Herschel 36 (Her 36), which is the brightest stellar system in M8 and consists of an O9 V and a B0.5 V star and a more distant companion O7.5 V star (Arias et al. 2010 & Sanchez-Bermudez et al. 2014). Her 36 also powers the bright Hourglass Nebula, which is a window shaped structure in a much denser compact HII region compared to its surroundings (Tothill et al., 2008).

To the south-east of the open cluster core is a dense large ($\sim$ few arcmins) molecular cloud comprising a small but rich embedded cluster with seven IR sources. M8 East (M8 E) is a massive star-forming region with atleast two massive stars being formed in it (see Tothill et al. 2008 and the references therein). The main ionising source, M8E IR, is a young stellar object (YSO) that is about to become a BO star, which dominates the cluster luminosity till ~ 24 μm (Linz et al., 2008).

1.6 About this thesis

In this work, we unveiled one of the brightest regions in our Galaxy with new, high resolution observations in the FIR and submm wavelengths.

1.6.1 Motivation

M8 hosts one of the brightest PDRs in our galaxy. It has been extensively studied in the X-ray, optical and IR regimes but despite being associated with bright PDRs, HII regions and star forming regions, only a few studies have been performed at mm and submm wavelengths. Interestingly, the second strongest source of mm and submm wavelength CO line emission in our Galaxy has been reported toward Her 36 in M8 (White et al., 1997). Owing to its brightness and the fact that it has been explored so little, M8 acts as a perfect laboratory to study different evolutionary stages of star formation and the hydrocarbon chemistry in the PDRs.

The rationale behind studying the star-forming region associated with HII regions and PDRs of the bright M8 is described briefly as follows:

- Understanding the physics of the ISM: Massive stars are responsible for injecting a considerable amount of energy into the ISM causing, several heating and cooling processes to set in motion. This mechanical and radiative feedback both stimulates and ceases star formation giving rise to protostars, HII regions and PDRs. These different evolutionary stages of star formation not only differ in their physical environments but also result in different chemical composition throughout

the ISM. The questions we want to address are: how to identify and characterise these different evolutionary stages (HII region and PDR of M8)? How do these evolutionary stages affect the ISM?

- Exploring the hydrocarbon chemistry in PDRs: Hydrocarbons are ubiquitous in the ISM, yet the chemical pathways leading to their formation in the ISM are not completely understood. We make an attempt to know how the FUV photons affect the formation and destruction processes of hydrocarbons in PDRs (M8).

1.6.2 Goals

Withholding the above mentioned motivation, the scientific objectives for carrying out this research work are described within the following lines:

- To explore the geometry and kinematics of M8 and to quantify its molecular cloud mass, gas temperatures and densities.
- To establish an inventory of hydrocarbons in M8 and to understand their formation process in PDRs by comparing observations to PDR modeling results.
- To study how different molecules can be used as diffuse and dense gas tracers to characterise regions of different physical conditions in M8 E.
- Finally, to compare M8 with M8 E and other well known PDRs (such as the Orion Bar, M17) in order to find the Lagoon Nebula's place in the universal picture of PDRs.

1.6.3 Outline

The organisation of this thesis is as follows: we describe the observations and the theory behind the data analysis in chapter 2. In chapter 3, we characterise the PDR of M8 by presenting the observed maps of the fine structure lines of [C II] , [C I] and rotational transitions of CO. To explore the distribution of the molecular cloud, the HII region and the PDR around Her 36, we compare the velocity channel maps of [C II] with optical, IR and radio images of the nebula. In chapter 4, we present the spectra of the observed hydrocarbons and their maps overlaid with dust continuum images at different wavelengths toward M8. We constrain the physical conditions of the gas responsible for the emission of hydrocarbons and also discuss about the formation mechanisms of hydrocarbons in PDRs. In chapter 5, we explore the star-forming region of M8 E by analysing the diffuse and dense gas tracers observed toward it. We also compare the different star-forming environments of M8 and M8 E. The main conclusions and outlook of this work are summarised in chapter 6.

Chapter 2

Observations and theoretical background

2.1 Observations

For much of the last 70 years (since Bok & Reilly 1947 studied the dark clouds in M8), it has been a struggle to observe the star formation process and to develop a theory to explain it due to the fact that most stars form in dark clouds and they are optically invisible during their formative stages. T Tauri stars were the first low mass stars identified as young stellar objects because they could be detected in optical wavelengths. Objects in earlier evolutionary stages, which are still embedded in their natal clouds and thus blocked by dust and could not be observed. But in the last 30 years or so, the advancement in observational astronomy has lead to the opening of the IR, submm and mm wavelength windows to the astronomers and this has resulted in direct observations of star-forming regions, which has significantly enhanced our knowledge of the star formation process and their feedback mechanisms.

For the data presented in this thesis, we performed observations using world class telescope facilities (telescope images are shown in Fig. 2.1):

1) **The Institut de Radioastronomie Millimétrique (IRAM[1]) 30 m telescope** is situated on Pico Veleta in the Spanish Sierra Nevada. It is one of today's largest and most sensitive radio telescopes for tracing mm waves. It can observe in the 3, 2, 1, and 0.9 mm wavelength windows, with its two receivers: EMIR[2] (Eight MIxer Receiver) and HERA (HEterodyne Receiver Array). We used EMIR to perform a line survey in the complete 3 mm window using its E090 band.
2) **The Atacama Pathfinder Experiment (APEX)** is a 12 m dish telescope located in the Llano de Chajnantor at 5104 m altitude in the Chilean Atacama desert, an excellent site for submm astronomy. It currently offers the instruments: SEPIA (Swedish ESO PI receiver for APEX) at 159–211, 272–376 (in construction) and 578–738 GHz, PI230 at 200–270 GHz, LASMA at 262–374 GHz, FLASH (First Light APEX Submillimeter Heterodyne receiver) at 262–374 and 374–516 GHz and CHAMP (The Carbon Heterodyne Array of the MPIfR) at 620–720 and 780–950 GHz. Among these, we observed several transitions of various molecules (like CO, HCN, HNC, N_2H^+, C_2H, c-C_3H_2, etc.) using the following receivers:

[1] https://www.iram-institute.org
[2] http://www.iram.es/IRAMES/mainWiki/EmirforAstronomers

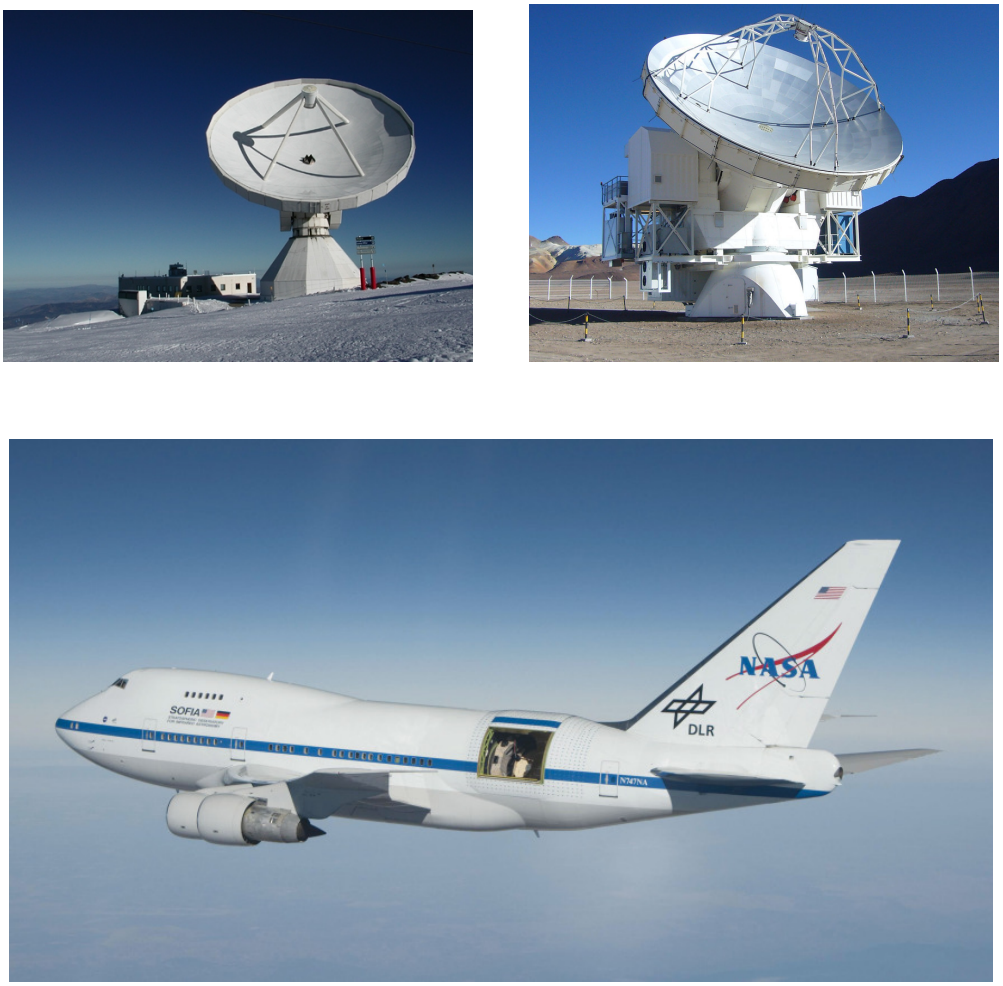

Figure 2.1: Telescopes used for performing a comprehensive survey to observe various species in submm, mm and IR wavelengths toward M8. Upper panel (left to right): IRAM 30 m and APEX 12 m telescopes, lower panel: SOFIA 2.5 m telescope.

- PI230: It is a dual polarisation receiver that covers the entire spectral window of 195–270 Ghz in sky frequency and has two separate side bands of 8 GHz each.

- FLASH: It is a dual frequency receiver that operates simultaneously in the 345 and 460 GHz atmospheric windows providing a continuous sky frequency coverage from 268–516 GHz. It works at orthogonal polarization. It also has two separate side bands of 4 GHz each.

- CHAMP: Similar to FLASH, CHAMP operates simultaneously in the 690 and 810 GHz atmospheric windows at orthogonal polarization. It provides the highest spatial resolution (8.8″ at 692 GHz and 7.7″ at 806 GHz) among the other receivers operating at APEX. The receiver is currently being rectified with new mixers, IF and electronics.

3) **The Stratospheric Observatory for Infrared Astronomy (SOFIA[3])** is a Boeing 747SP aircraft carrying a telescope with an effective diameter of 2.5 m. It observes from 12 and 14 km altitudes, which is above 99% of earth's water vapour. It can observe at IR and submm wavelengths (from $\sim$ 0.36 μm to 612 μm), with its seven receivers: EXES (Echelon-Cross-Echelle Spectrograph), FIFI-LS (Field Imaging Far-Infrared Line Spectrometer), FORCAST (Faint Object InfraRed CAmera for the SOFIA Telescope), FPI+ (Focal Plane Imager), GREAT (German Receiver for Astronomy at Terahertz Frequencies), HAWC+ (High-resolution Airborne Wideband Camera) and HIRMES (HIgh Resolution Mid-infrarEd Spectrometer, in construction). Figure 2.2 shows the atmospheric transmission plot for SOFIA compared to that of APEX, which is one of the best sites for ground based astronomy. It is clear that at low wavelengths/ high frequencies, observations are possible only from high altitudes and SOFIA is one such facility.

We observed the [C II] fine structure line and high J CO transitions using the GREAT receiver, which is a dual channel heterodyne instrument, offering high resolution observing capabilities (upto R = 10^8) in a variety of frequency windows in the 0.490–4.74477749 THz range. The observing channels offered by GREAT are:

- upGREAT Low Frequency Array (LFA): The LFA is a 7 pixel array with 2 polarizations (14 pixels in total) positioned in a hexagonal setting with a central beam. It can be tuned in a frequency range of 1.810–2.070 THz.
- upGREAT High Frequency Array (HFA): The HFA has a similar configuration as LFA, but with a single polarization, hence has a total of 7 pixels. It's tuning range is limited to the [O I] frequency of 4.74477749 THz.
- 4GREAT: The 4GREAT comprises 4 closely spaced (within few arcsecs) co-aligned pixels at 4 different frequency ranges: the Herschel/HIFI band 1 at 490–635 GHz, the Herschel/HIFI band 4 at 890–1100 GHz, the GREAT L1 channel at 1200–1500 GHz and the GREAT M channel at 2490–2590 GHz.

Table 2.1: Line parameters of observed transitions.

Species	Transition	Frequency (GHz)	$\theta_{\rm mb}('')$	Telescope
CO	$J = 1 \rightarrow 0$	115.271	22.5	IRAM 30m/EMIR
CO	$J = 3 \rightarrow 2$	345.796	19.2	APEX/FLASH$^+$
[C II]	$^2P_{3/2} \rightarrow {}^2P_{1/2}$	1900.53	14.8	SOFIA/GREAT

Table 2.1 shows some of the observed species with IRAM 30 m, APEX and SOFIA telescopes. The angular resolutions at which these observations were made are comparable to each other, making it easy to combine them in order to draw inferences

[3]https://www.sofia.usra.edu/science/instruments/great

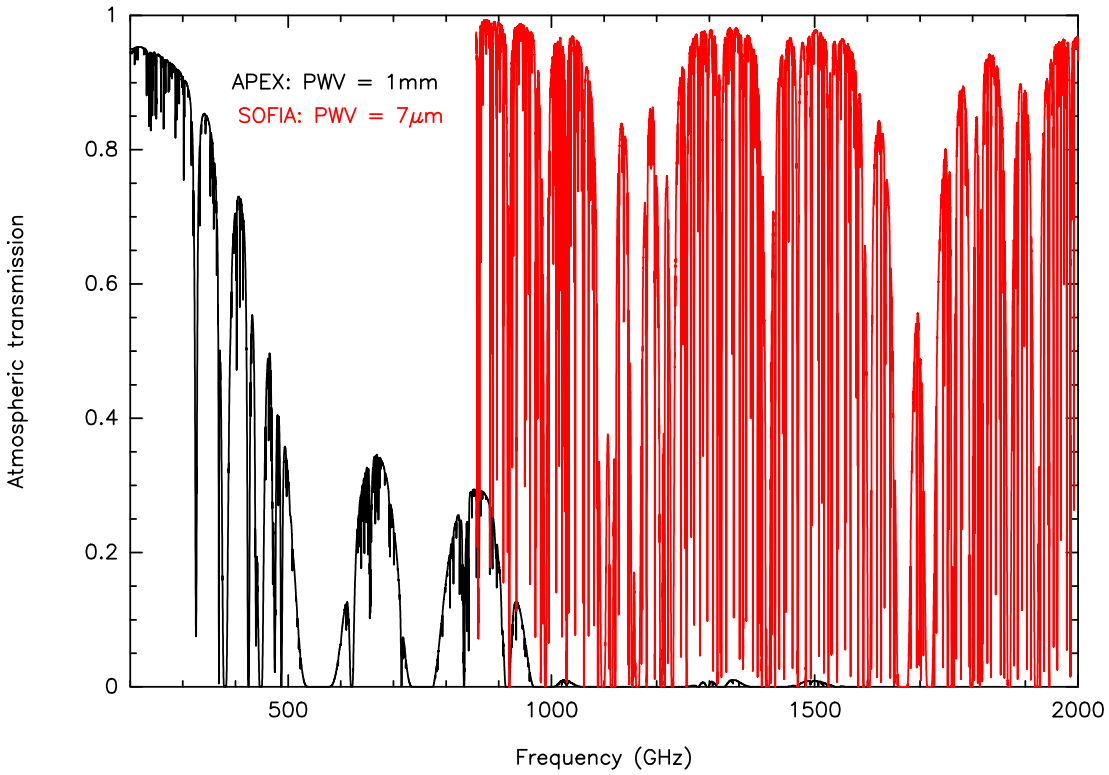

Figure 2.2: Atmospheric transmission plot for SOFIA (in red) at an altitude of $\sim$ 12.5 km and 7 μm of precipitable water vapor (PWV) compared to APEX (in black) at an altitude of 5 km and 1 mm of PWV. Values close to 1, represent 100% transmittance i.e. all the radiation is able to pass through the atmosphere at the given wavelength/frequency.

from the analysed data.

Deeply integrated point observations toward Her 36 and M8E IR were performed along with mapping observations of about few arcmins around these ionising sources. The details of individual observing runs are given in subsequent chapters. We combined our observations with other surveys done in the optical radio and IR regimes allowing a multi-wavelength view of M8 to explore the evolution of gas from the hot ionized HII region to the warm PDR to further into the dense cold molecular cloud.

2.2 Theoretical background

In order to study the physical and chemical conditions in different regions of the ISM, it is fundamental to determine the temperatures and densities of the clouds of gas and the column densities (N) of the observed species. Several works (for e.g. Goldsmith & Langer 1999, Draine 2011, Mangum & Shirley 2015) have been published addressing this subject. Here, we describe a step by step method to calculate these quantities

summarizing their approaches.

A telescope receives energy (E) that can be divided by the observing time (t), collecting area (A) and bandwidth (ν) giving the flux density:

$$F_\nu = \frac{dE}{dtdAd\nu}, \tag{2.1}$$

and the flux (F) is directly connected to the luminosity (L) as

$$F = \frac{L}{4\pi D^2}, \tag{2.2}$$

where, D is the distance to the object. The specific intensity is defined as the flux density within the solid angle, Ω, the source subtends:

$$I_\nu = \frac{dE}{dtdAd\nu d\Omega}. \tag{2.3}$$

If we assume that a source of size R emits a constant luminosity (L_ν) at a frequency ν at its surface, then the flux density and specific intensity are

$$F_\nu = \iint I_\nu d\Omega = \frac{L_\nu}{4\pi D^2} \tag{2.4}$$

$$I_\nu = \frac{F_\nu}{\Delta\Omega} = \frac{L_\nu}{4R^2}. \tag{2.5}$$

The amount of power received by a radio telescope from a source in terms of flux or the antenna temperature and without any contribution from the background

$$P^{\text{source}} = \frac{1}{2} A\eta F_\nu \Delta\nu = kT_\text{A}\Delta\nu \tag{2.6}$$

where, the factor $1/2$ accounts for the fact that a single polarisation is observed (Kraus, 1966), k is the Boltzmann constant and and η is the beam efficiency of the telescope, such that the main beam temperature $T_\text{mb} = T_\text{A}/\eta$. This gives:

$$T_\text{mb} = \frac{A}{2k} F_\nu^{\text{source}}. \tag{2.7}$$

In the case when the source is completely resolved, the T_mb will be equal to the radiation temperature (T_R) in the Rayleigh-Jeans approximation (of the intensity of a black body emission at very low frequencies $h\nu << kT$; h is Planck's constant), but otherwise the inferred temperature from the telescope is only a lower limit to the actual source brightness:

$$T_\text{mb} \leq \frac{c^2}{2\nu^2 k} I_\nu^{\text{source}}. \tag{2.8}$$

2.2.1 Radiative transfer

A beam of radiation with intensity I_ν propagates through a medium of path length s (along the direction of propagation). Assuming that this process is only affected by absorption and emission (scattering neglected), the variation in intensity occurs according to the radiative transfer equation:

$$dI_\nu = -I_\nu \kappa_\nu ds + j_\nu ds \tag{2.9}$$

where, κ_ν is the absorption coefficient and j_ν is the emissivity. A relatively easy to determine physical quantity, optical depth, can be defined in terms of the path length $d\tau_\nu \equiv \kappa_\nu ds$, such that the equation of radiative transfer becomes:

$$dI_\nu = -I_\nu d\tau_\nu + S_\nu d\tau_\nu \tag{2.10}$$

where, we introduce a source term, $S_\nu \equiv \frac{j_\nu}{\kappa_\nu}$, which is devoid of any dependence on scattering processes. On integrating the above equation after multiplying with a factor of e^{τ_ν} and then diving by it after the integration, we get:

$$I_\nu(\tau_\nu) = I_\nu(bg)e^{-\tau_\nu} + \int_0^{\tau_\nu} e^{-(\tau_\nu - \tau')} S_\nu d\tau' \tag{2.11}$$

Since, we are interested in studying emission of photons when an atom or molecule makes a transition form a higher excited state, u, to a lower one, l, we define κ_ν and j_ν in terms of Einstein coefficients:

$$\kappa_\nu = \frac{h\nu\phi_\nu}{4\pi}(n_\mathrm{l}B_\mathrm{lu} - n_\mathrm{u}B_\mathrm{ul}) \tag{2.12}$$

$$j_\nu = \frac{1}{4\pi} n_\mathrm{u} A_\mathrm{ul} h\nu\phi_\nu \tag{2.13}$$

where, n is the level population, the Einstein coefficients A is a measure of probability of spontaneous emission of photons while B is related to the absorption and stimulated emission of photons. ϕ determines the spectral line profile of the observed emission. Assuming thermal equilibrium, the level populations must follow the Boltzmann distribution such that the Einstein coefficients are related to each other by:

$$g_\mathrm{l}B_\mathrm{lu} = g_\mathrm{u}B_\mathrm{ul} \tag{2.14}$$

$$A_\mathrm{ul} = \frac{2h\nu^3}{c^2} B_\mathrm{ul}. \tag{2.15}$$

where, g is the degeneracy of a given level. So, the source term can be written as

$$S_\nu = \frac{A_\mathrm{ul}}{B_\mathrm{ul}} \frac{1}{\frac{n_\mathrm{l} g_\mathrm{u}}{n_\mathrm{u} g_\mathrm{l}} - 1}. \tag{2.16}$$

Now, we can define the excitation temperature (T_ex) at which two levels are populated according to the Boltzmann distribution:

$$\frac{n_{\rm u}}{n_{\rm l}} = \frac{g_{\rm u}}{g_{\rm l}} e^{-\frac{h\nu}{kT_{\rm ex}}} \tag{2.17}$$

so the source function becomes: $S_\nu = B_\nu(T_{\rm ex})$, where $B_\nu(T)$ is the Planck function at temperature T:

$$B_\nu(T_{\rm ex}) = \frac{2h\nu^3}{c^2} \frac{1}{e^{\frac{h\nu}{kT}} - 1}. \tag{2.18}$$

Assuming $T_{\rm ex}$ is constant and substituting $S_\nu = B_\nu(T_{\rm ex})$ in eq. 2.11, we get:

$$I_\nu(\tau_\nu) = I_\nu(bg) e^{-\tau_\nu} + B_\nu(T_{\rm ex})(1 - e^{-\tau_\nu}). \tag{2.19}$$

In the process of detecting an emission line, we are interested in the difference between the intensity measured toward a molecular line source position and measured toward an emission free reference position:

$$\Delta I_\nu \equiv I_\nu - I_{\rm bg} \tag{2.20}$$

$$\Delta I_\nu = [B_\nu(T_{\rm ex}) - B_\nu(T_{\rm bg})](1 - e^{-\tau_\nu}) \tag{2.21}$$

If we now substitute eq. 2.18 and write I_ν in terms of T (as shown in eq. 2.8) in eq. 2.19, we get a relation between excitation temperature and the observed main beam temperature:

$$T_{\rm mb} = \frac{h\nu}{k} \left[\frac{1}{e^{\frac{h\nu}{kT_{\rm ex}}} - 1} - \frac{1}{e^{\frac{h\nu}{kT_{\rm bg}}} - 1} \right] (1 - e^{-\tau_\nu}) \tag{2.22}$$

2.2.2 Column density estimation

Column density is defined as the number of atoms or molecules (in a certain energy level) per unit area along the line of sight. Determination of it is the most basic step in calculating important physical quantities like abundances of observed species, spatial density and kinetic temperature of the ISM. Based on the calculations presented in Goldsmith & Langer (1999) and Peng (2010), we describe a methodology to define total column density in terms of measurable quantities: $T_{\rm mb}$ and the line's width, Δv.

Column density in the upper level can be derived in terms of velocity integrated intensity:

$$N_{\rm u} = \frac{8\pi k\nu^2}{hc^3 A_{\rm ul}} \left(\frac{\Delta\Omega_{\rm s}}{\Delta\Omega_{\rm a}} \right) \left(\frac{\tau_\nu}{1 - e^{-\tau_\nu}} \right) \int T_{\rm mb} dv \tag{2.23}$$

where, $\Delta\Omega_{\rm s}$ and $\Delta\Omega_{\rm a}$ are source and antenna solid angle, respectively, such that the second term in the above equation takes into account the beam dilution effects, while the third term accounts for the optical depth effects. In the case where a molecule is

in local thermodynamic equilibrium (LTE), its total column density integrated over all energy levels can be written as:

$$N_{\rm tot} = \frac{N_{\rm u}}{g_{\rm u}} Q_{\rm rot} e^{\frac{E_{\rm u}}{kT_{\rm mb}}}, \tag{2.24}$$

where $Q_{\rm rot}$ is the rotational partition function, which represents a statistical sum over all rotational energy levels in the molecule. For a linear molecule, we can compute $A_{\rm ul}$ for every rotational level J in terms of ν and dipole moment, μ. For a transition $J \rightarrow J-1$:

$$A_{\rm J,J-1} = \frac{64\pi^4\nu^3\mu^2}{3hc^3}\frac{J}{2J+1}. \tag{2.25}$$

We assume the source to fill the beam and the emission to be optically thin such that the second and third terms in eq. 2.23 are equal to unity. Further substituting eq. 2.23 and eq. 2.25 in eq. 2.24, we get:

$$N_{\rm tot} = \frac{3k}{8\pi^3\nu}\frac{Q_{\rm rot}}{\mu^2 J} e^{\frac{E_{\rm u}}{kT_{\rm mb}}} \int T_{\rm mb} dv. \tag{2.26}$$

2.2.3 PDR modeling

A comparison between observations and theoretical models of PDRs is very important for a deeper understanding of the formation and destruction processes of various species observed in the ISM and to study the heating and cooling of the ISM. Modeling plays a major role in determining the level of ionisation, gas temperatures and in exploring the density structure of PDRs. These models are able to constrain the physical and chemical conditions of all the regions that are affected by FUV photons i.e. most of the atomic gas (in diffuse and dense regions), regions containing molecules like H_2 and CO, which are dissociated by FUV photons. Hence, PDR models are basically used to study the molecular clouds, regions surrounding young and protostellar objects, interfaces with HII regions, massive star forming regions and gas near planetary nebulae i.e. most of the ISM!

Theoretical models relate the observations to the modelled physical parameters, which help us to predict the nature of the regions in the ISM responsible for the line and continuum emission/absorption. These modelled parameters unveil the nature, structure and evolutionary sequence of the ISM (Tielens & Hollenbach, 1985).

Over the last 40 years, a huge effort has been made to construct PDR models. From Hollenbach & Salpeter (1971) to Le Bourlot et al. (2012) a variety of different models have been developed and updated to provide better understanding of the ISM. Röllig et al. (2007) summarises how various computer codes have been designed with different aims like some models focus on exploring a particular type of region such as HII regions, protoplanetary disks, diffuse clouds, etc. Some model precisely manage micro-physical

processes, while others emphasize computing model grids to estimate the physical conditions of various regions from comparison with observational data. Röllig et al. (2007) reported a detailed comparison study of different PDR models based on different model setups. Here, we briefly summarise the important modeling features and describe the codes that are crucial for this thesis:

- The chosen geometry: The most common morphological setups are plane parallel slab and spherical geometries. The plane parallel slab can be illuminated from one or both sides and the illumination is perpendicular to the cloud surface, which simplifies solving the radiative transfer equation as there is only one line of sight. The slab can be infinite or of finite length. In the spherical geometry, illumination is either uni-directional or isotropical causing differences in attenuation of the radiation. In finite plane parallel and spherical models, radiation is impinged on the cloud surface from multiple directions and hence iterations over depth or radius are required as the physical and chemical structure and the opacities are calculated only after several iterations.

- Chemical network: The rich PDR chemistry has been studied in great detail by many authors (for e.g. Tielens & Hollenbach 1985, Pety et al. 2005, Meijerink & Spaans 2005, Le Petit et al. 2006, Le Bourlot et al. 2012, Cuadrado et al. 2017). The most important aspects while including a chemical network in a code are to decide which species are to be included, what kind of reactions are to be considered and with what reaction rates. The number of species included depends on the code's applicability. But it is crucial to include the main species, which characterise the physical structure of the PDRs namely [C II] , [C I] , [O I] , CO and H_2. It is also important to include all the known chemical reactions for a given species with their accurate rate coefficients. Several databases that are created by including both theoretical and experimental results, are available (e.g. LAMDA, Schöier et al. 2005).

- Heating and cooling processes: There are many heating processes like photo-electric heating through dust and PAHs, collisional de-excitation of vibrationally excited H_2, cosmic ray ionisation, H_2 formation and dissociation, turbulence and grain-grain collisions. Similarly, many cooling processes are possible such as IR emission of fine structure lines of [C II] 158 μm, [O I] 63 and 145 μm, [C I] 370 and 610 μm, [S II] 35 μm, submm emission of CO, H_2O and gas-grain collisions. The degree of detail in which these processes are modeled have a huge impact on the results of the code.

- Dust properties: PAHs and dust grains affect the ISM in multiple ways by taking part in photo electric heating, by absorbing and scattering photons (influencing radiative transfer) and by acting on the cloud chemistry through grain surface reactions. Overviews on PAHs and dust grains can be found in Draine (2003) and Tielens (2008). Inclusion of dust properties in varying degrees influences the modeling results by for increasing or decreasing the photodissociation rates, etc.

- Radiative transfer: The computation of emission and absorption of radiation throughout the model code is done by radiative transfer methods. Non-LTE radiative transfer programs are used to determine level populations and resulting output spectra, which can then be compared to the observational data. Depending on the above mentioned modeling aspects, these programs are responsible for coupling the physical and chemical conditions of different parts of the PDR together. An overview examining and comparing different radiative transfer methods is given by van Zadelhoff et al. (2002).

We will now describe a few steady state, stationary PDR models that we have used (in the next two chapters) to compare with our observations.

- HTBKW (D. Hollenbach, A.G.G.M. Tielens, M.G. Burton, M.J. Kaufman, M.G. Wolfire): Tielens & Hollenbach (1985) provided the first detailed PDR code to study the transition of H to H_2 and C^+ to CO in the neutral ISM. The code uses a finite or semi-infinite plane parallel slab geometry where the radiation field is impinging on the cloud surface from one direction. Both Habing (Habing, 1968) and Draine (Draine, 1978) fields are considered while including the wavelength dependence of the incident FUV flux. The code has a fixed number of species, H_2 formation takes place on grains. Density and pressure are constant. The model makes predictions for line profiles emitted intensities, opacities, abundance and temperature profiles as a function of A_v.

- Meijerink and Spaans: Apart from all the modeling features stated above for HTBKW, Meijerink & Spaans (2005) presented a PDR code containing a more elaborate chemical network with more than 300 species. Temperature is fixed. More species contribute to heating and cooling processes (e.g. cooling via H_2 rotational lines and heating via grain-grain collisions). In addition to the HTBKW model outcomes, column densities, heating & cooling rates and chemical rates as a function of A_v are also predicted.

- Meudon: Le Petit et al. (2006) presented the Meudon PDR code, which is an upgrade to the old code by Le Bourlot et al. (1993). Several updates have been made to the model since then by Goicoechea & Le Bourlot (2007), Gonzalez Garcia et al. (2008), Le Petit et al. (2009), Bron et al. (2014) & Bron et al. (2016). This code is similar to its counterparts summarised above but has many additional features. Radiation can illuminate the slab uni-directionally or isotropically or by a combination of both. The model can simulate any number of species. Molecules other than H_2 can be formed on grains and they can get desorbed by several mechanisms like photoevaporation and CR spot heating. It includes various isotopomers of C and O. The code has more cooling and heating mechanisms compared to HTBKW and Meijerink Spaans models. Many more dust properties like grain size distribution and extinction/scattering laws are included in the code. The code's output also includes excitation of H_2, which is missing in the other codes.

We run these codes for different physical parameters suited to match our observational results. Choice of physical parameters and their interpretation is described in detail in Chapter 3 and 4.

Chapter 3

Unveiling the remarkable photodissociation region of Messier 8

Abstract

Aims. Messier 8 (M8) is one of the brightest HII regions in the sky. We collected an extensive dataset comprising multiple submillimeter spectral lines from neutral and ionized carbon and from CO. Based on this dataset, we aim to understand the morphology of M8 and that of its associated photodissociation region (PDR) and to carry out a quantitative analysis of the physical conditions of these regions such as kinetic temperatures and volume densities.

Methods. We used the Stratospheric Observatory For Infrared Astronomy (SOFIA), the Atacama Pathfinder Experiment (APEX) 12 m, and the Institut de Radioastronomie Millimétrique (IRAM) 30 m telescopes to perform a comprehensive imaging survey of the emission from the fine structure lines of [C II] and [C I] and multiple rotational transitions of carbon monoxide (CO) isotopologs within 1.3 × 1.3 pc around the dominant Herschel 36 (Her 36) system, which is composed of at least three massive stars. To further explore the morphology of the region, we compared archival infrared, optical, and radio images of the nebula with our newly obtained fine structure line and CO data, and in particular with the velocity information these data provide. We performed a quantitative analysis, using both LTE and non-LTE methods to determine the abundances of some of the observed species, kinetic temperatures, and volume densities.

Results. Bright CO, [C II] and [C I] emission have been found toward the HII region and the PDR in M8. Our analysis places the bulk of the molecular material in the background of the nebulosity illuminated by the bright stellar systems Her 36 and 9 Sagitarii. Since the emission from all observed atomic and molecular tracers peaks at or close to the position of Her 36, we conclude that the star is still physically close to its natal dense cloud core and heats it. A veil of warm gas moves away from Her 36 toward the Sun and its associated dust contributes to the foreground extinction in the region. One of the most prominent star forming regions in M8, the Hourglass Nebula, is particularly bright due to cracks in this veil close to Her 36. We obtain H_2 densities ranging from $\sim 10^4$ – 10^6 cm^{-3} and kinetic temperatures of 100 – 150 K in the bright PDR caused by Her 36 using radiative transfer modeling of various transitions of CO isotopologs.

3.1 Introduction

The influence of bright stars on their surrounding interstellar medium (ISM) is immense. Their strong ultraviolet and far-ultraviolet (FUV) fields give rise to bright HII regions and photodissociation regions (PDRs). These are the best grounds to study the effect of UV and FUV photons on the heating and chemistry of ISM. The fine structure lines of C^+ and O, observable at far-infrared (FIR) wavelengths, are mainly responsible for the cooling in these regions (Tielens & Hollenbach, 1985), which allow us to deduce the amount and sometimes the source of heating as well. The fine structure line of C^+ at 158 μm is one of the brightest lines in PDRs and traces the transition from H^+ to H and H_2 as C has an ionization potential of 11.3 eV (e.g., Pabst et al. 2017). In PDRs, a C^+ layer extends to a depth of $A_v \sim 2 - 4$, after which C^+ recombines to C probing the interface to CO (Hollenbach & Tielens, 1999). Deeper into the associated molecular clouds, cooling is dominated by the transitions of CO, observable at (sub)millimeter and FIR wavelengths. Modeling the relative intensity distributions of multiple lines from various molecular and atomic species allows us to derive the physical conditions in PDRs.

Messier 8 (M8) is located in the Sagittarius-Carina arm, near our line of sight toward the Galactic center. It is located at a distance ∼1.25 kpc ($1'$ corresponds to 0.36 pc) from the Sun (Damiani et al. 2004 and Arias et al. 2006) with an error of ∼ 0.1 kpc (Tothill et al., 2008) and is about 34 × 12 pc in diameter. M8 is associated with the open young stellar cluster NGC6530, the HII region NGC6523/33, and large quantities of molecular gas (Tothill et al., 2008).

The open cluster NGC 6530 (centered at R.A. $18^h04^m24^s$, Dec. $-24°21'12''$(J2000)) is a relatively young cluster (formed about 2 – 4 Myrs ago, Chen et al., 2007) and contains several bright O-type stars. The brightest among them is Her 36 (Woolf, 1961) at R.A. $18^h03^m40^s.3$, Dec. $-24°22'43''$(J2000). It is resolved into three main components: a close massive binary consisting of an O9 V and a B0.5 V star and a more distant companion O7.5 V star (Arias et al. 2010 and Sanchez-Bermudez et al. 2014). Her 36 is responsible for ionizing the gas in the western half of the HII region of NGC 6523 including the bright Hourglass Nebula (Woolf 1961, Lada et al. 1976, and Woodward et al. 1986). Lada et al. (1976) compared the optical and millimeter-wave observations of the M8 region and suggested the molecular cloud is located behind the HII region of the nebula, similar to the Orion-KL nebula. An ultracompact HII region, G5.97–1.17 is also very close to Her 36 at (R.A. $18^h03^m40.5^s$, Dec. $-24°22'44.3''$(J2000)) (Masqué et al., 2014).

A multiband near-IR image of Her 36 and its surroundings presented in Goto et al. (2006) shows the IR source Her 36 SE lying $0.25''$ SE of Her 36 and it is completely obscured. It is inferred to be an early-type B star with a visual extinction $A_V > 60$ mag that is deeply embedded in dense, warm dust and is powering the ultracompact HII region G5.97–1.17. The morphology of H_2 and CO $J = 3 \rightarrow 2$ emission around Her 36

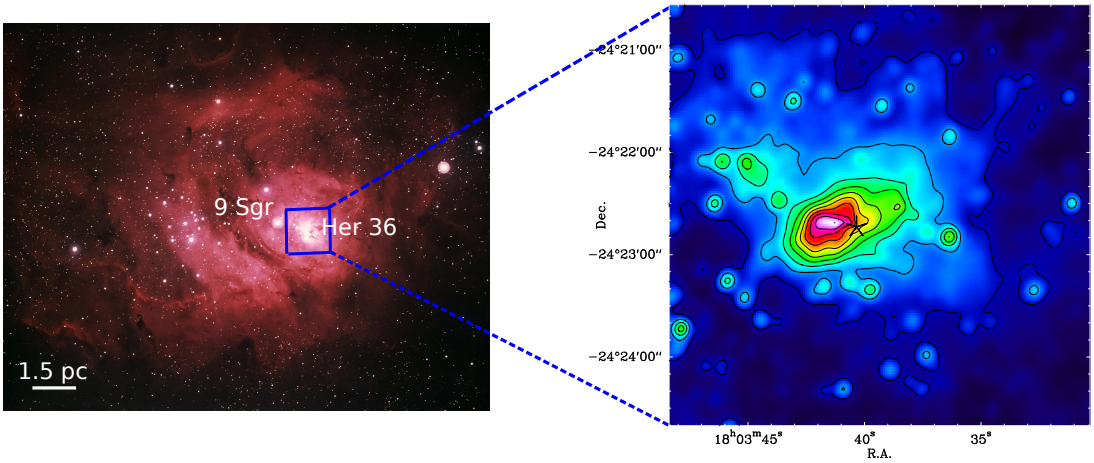

Figure 3.1: Left panel: Lagoon Nebula, Messier object 8 (M8), or NGC 6523 in the constellation of Sagittarius, as seen by the Kitt Peak 4 m Mayall telescope in 1973. North is up, east to left. Credits to National Optical Astronomy Observatory/Association of Universities for Research in Astronomy/National Science Foundation Copyright WIYN Consortium, Inc., all rights reserved. The right panel shows the WISE 3.4 μm image of the M8 region around Her 36 (denoted with a star) investigated in this paper. The contour levels are 10% to 100% in steps of 10% of the peak emission $\sim$ 4000 data number. The 1.5 pc indicated in the lower left correspond to 4′.

(White et al. 1997 and Burton 2002) is in accordance with the Hubble Space Telescope (HST) jet-like feature detections extending 0.5″ southeast of Her 36 (Stecklum et al., 1995), which suggest there might be a molecular outflow in the core of M8 (Burton, 2002). X-ray emission from Her 36 and diffuse X-ray emission from the Hourglass region, which is the brightest part of the optically visible nebula located $\sim$ 15″ east from Her 36 (Rauw et al., 2002), suggest the presence of a bubble of hot gas of size 0.4 pc that is produced by the interaction of the stellar wind of Her 36 with the denser part of the molecular cloud in the background. Anomalously broad diffuse interstellar bands (DIBs) at 5780.5, 5797.1, 6196.0, and 6613.6 Å along with CH^+ and CH are found in absorption along the line of sight to Her 36 (Dahlstrom et al., 2013). CH^+ and CH are radiatively excited by strong FIR emission from the adjacent IR source Her 36 SE (Goto et al., 2006) and the broadening of DIBs is attributed to radiative pumping of closely spaced high-J rotational levels of small polar carrier molecules (Dahlstrom et al. 2013, Oka et al. 2014, and York et al. 2014). We performed (sub)millimeter observations related to these species that will be discussed in a future paper.

The eastern half of the HII region is illuminated by the 9 Sgr stellar system, as shown in Fig. 3.1. 9 Sgr is a well-known binary with an orbit of $\sim$ 9 yr duration, consisting of an O3.5 V primary and an O5-5.5 V secondary (Rauw et al., 2012). Southeast of the cluster core (NGC 6530), another cluster, M8E, although optically invisible, is associated with two massive star forming regions (Tothill et al., 2008). A superposition

of four HII regions seems to be responsible for the ionization of the gas in M8: the Hourglass Nebula illuminated by Her 36, the core of NGC 6523 illuminated by Her 36, the remaining parts of NGC 6523 and NGC 6533 illuminated by 9 Sgr (O4V) (Tothill et al., 2008), and M8E illuminated by HD 165052 (Lynds & Oneil 1982 and Woodward et al. 1986).

Although M8 has been studied extensively in the X-ray, optical, and IR regimes (Stecklum et al. 1995, Damiani et al. 2004, Arias et al. 2006, Goto et al. 2006, and Damiani et al. 2017), only few studies have been performed at millimeter and submillimeter wavelengths. White et al. (1997) reported the discovery of the second strongest source of millimeter and submillimeter wavelength CO line emission in our Galaxy toward Her 36 in M8 (White et al., 1997). Lada et al. (1976) compared optical and millimeter-wave observations to sketch the morphology of M8 where the core surrounding Her 36, the hourglass nebula with its structure and the eastern part of M8 are described. Tothill et al. (2002) presented submillimeter- and millimeter-wave maps of the $J = 2 \rightarrow 1$ and $J = 3 \rightarrow 2$ transitions of ^{12}CO tracing the molecular gas and dust around Her 36.

We report a comprehensive survey of the 1.5 × 1.5 pc ($4' \times 4'$) region around Her 36 (as shown by the blue square in Fig. 3.1) at FIR, millimeter- and submillimeter wavelengths to probe the physical conditions and image the morphology of this exceptional PDR. We present for the first time extended maps of this region in the 158 μm fine structure line of C^+, high-J transitions of ^{12}CO emission observed with the GREAT[1] receiver on board SOFIA observatory, the mid-J transitions of ^{12}CO and ^{13}CO using the PI230, FLASH$^+$, and CHAMP$^+$ receivers of the APEX[2] telescope, and low-J transitions of ^{12}CO and ^{13}CO using the EMIR receiver of the IRAM[3] 30 m telescope.

3.2 Observations

3.2.1 SOFIA/GREAT data

The high-J CO and [C II] 158 μm observations summarized in Table 3.1 were conducted with the L1 channel of the German Receiver for Astronomy at Terahertz frequencies (GREAT; Heyminck et al. 2012) and the upGREAT LFA arrays (Risacher et al., 2016) on board the Stratospheric Observatory for Infrared Astronomy (SOFIA; Young et al. 2012). The data was acquired during observatory flight #297 on 2016 May 14 at 14.2 km altitude and under a median water vapor column of 11 μm. The upGREAT was

[1]GREAT is a development by the MPI für Radioastronomie and KOSMA/Universität zu Köln, in cooperation with the MPI für Sonnensystemforschung and the DLR Institut für Planetenforschung.

[2]This publication is based on data acquired with the Atacama Pathfinder EXperiment (APEX). APEX is a collaboration between the Max-Planck-Institut für Radioastronomie, the European Southern Observatory, and the Onsala Space Observatory.

[3]Based on observations carried out with the IRAM 30 m telescope. IRAM is supported by INSU/CNRS (France), the MPG (Germany), and IGN (Spain).

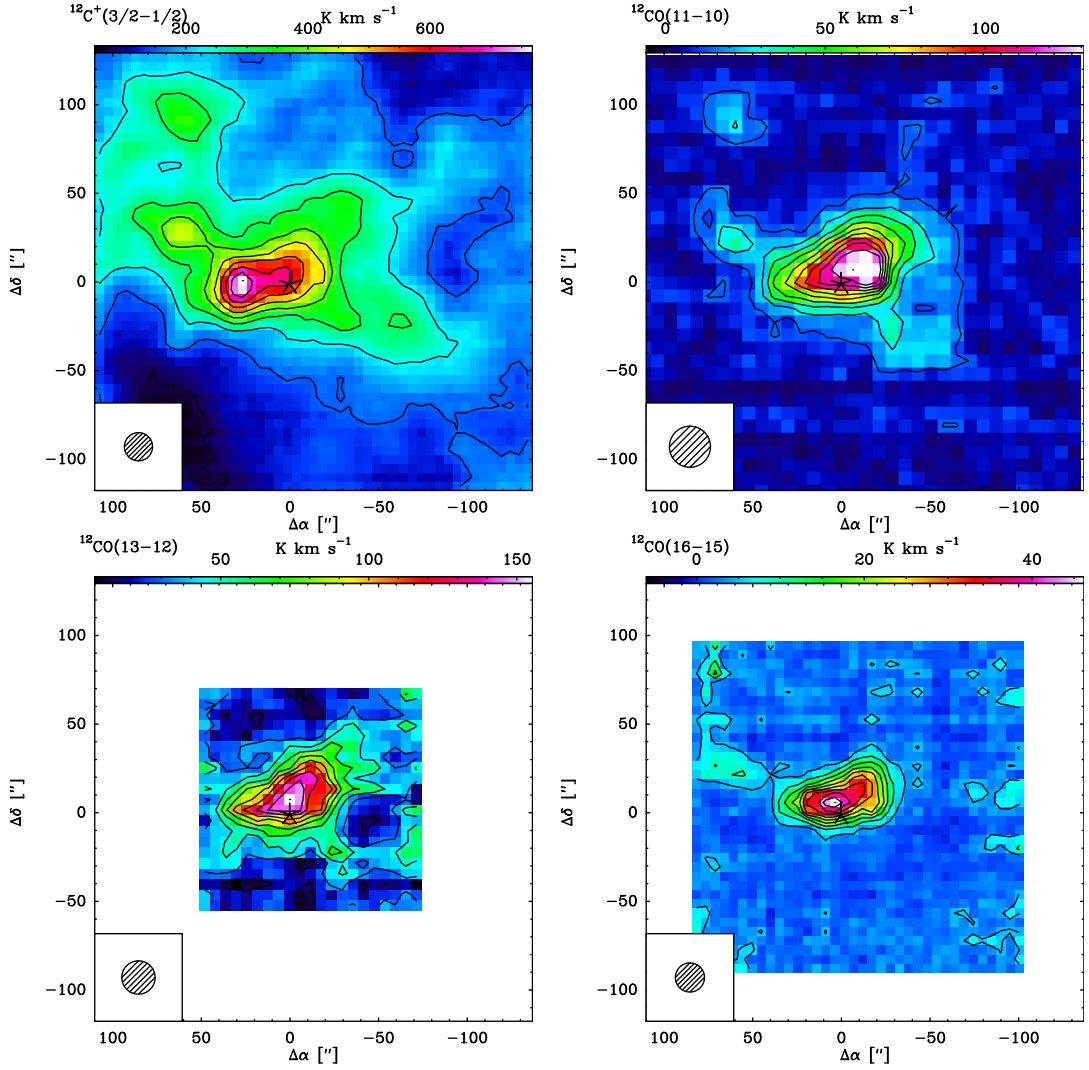

Figure 3.2: Color maps of the integrated intensity of the [C II] 158 μm and $J = 11 \rightarrow 10$, $J = 13 \rightarrow 12$, and $J = 16 \rightarrow 15$ transitions of ^{12}CO toward Her 36, which is the central position ($\Delta\alpha = 0$, $\Delta\delta = 0$) at R.A.(J2000) = $18^{\rm h}03^{\rm m}40.3^{\rm s}$ and Dec.(J2000) = $-24°22'43''$, denoted with an asterisk. The contour levels are 10% ($> 3 \times$ rms, given in Table 3.1) to 100% in steps of 10% of the corresponding peak emission given in Table 3.1. All maps are plotted using original beam sizes shown in the lower left of each map.

employed with 14 pixels (seven pixels for each polarization, with a hexagonal layout). The spectral analysis was performed by means of fast Fourier transform spectrometers (Klein et al., 2012), in a mode providing 4.0 GHz bandwidth with 2^{14} spectral channels.

In the first setup we simultaneously mapped the ^{12}CO $J = 11 \rightarrow 10$ transition at 1267.014.486 GHz and the [C II] $^2P_{3/2} \rightarrow {}^2P_{1/2}$ fine structure line at 1900.537 GHz. In a second setup the ^{12}CO $J = 13 \rightarrow 12$ and $J = 16 \rightarrow 15$ transitions at 1496.923 GHz and 1841.345 GHz were mapped, respectively. Typical single-sideband system temperatures ranged between 1600 and 1800 K for the lower frequency L1 channel and between 2080 and 2260 K for the higher frequency upGREAT array with atmospheric transmissions of 0.90 to 0.94 and 0.85 to 0.88, respectively. All maps shown in Fig. 3.2 were observed in on-the-fly (OTF) total power mode with a sampling of 6″ centered on R.A. $18^{\rm h}03^{\rm m}40^{\rm s}33$, Dec. $-24°22'42\farcs7$ (J2000), the Her 36 location. We integrated 0.4 s per record for the CO $(11 \rightarrow 10)$/[C II] setup, and 0.8 s for the CO $(13 \rightarrow 12)/(16 \rightarrow 15)$ setup. The originally chosen reference position at $(\Delta\alpha, \Delta\delta) = (+500'', -500'')$ (relative to the map center) was found to be contaminated in both transitions of the first setup and was therefore changed in favor of a second, clean reference at offset $(+30', -30')$, while the pointing accuracy of $< 3''$ was maintained.

The raw data was calibrated with the program kalibrate (Guan et al., 2012), which is part of the KOSMA software package. The resulting antenna temperatures $T_{\rm A}^*$ were converted to main beam brightness temperatures $T_{\rm mb} = T_{\rm A}^* \cdot F_{\rm eff}/B_{\rm eff}$ using a forward efficiency $F_{\rm eff} = 0.97$ and beam efficiencies of 0.66 for the L1 channel of GREAT, and 0.58 to 0.68 for the upGREAT pixels, with a median value of 0.65. In order to optimize the signal-to-noise ratio per channel, the spectra were smoothed to a resolution of 2.44 MHz, corresponding to 0.4 km s^{-1} for upGREAT and 0.6 km s^{-1} for the L1 channel. We subtracted spectral baselines of first order and subsequently produced data cubes with beam/3 sampling. For the beam sizes, see Table 3.1.

3.2.2 APEX data

Observations of low- and mid-J ^{12}CO and ^{13}CO transitions were performed with the Atacama Pathfinder Experiment (APEX) 12 m submillimeter telescope (Güsten et al., 2006) during 2015 June - August and 2016 July, September, and October. As shown in Table 1, we used the following receivers: PI230 to map the low-J ^{12}CO and ^{13}CO transitions, FLASH$^+$ in the 345 and 460 GHz bands to map the mid-J CO transitions, and CHAMP$^+$ in low- and high-frequency subarrays to map the higher frequency mid-J CO transitions.

We used the PI230 receiver to map C^{18}O $J = 2 \rightarrow 1$ at 219.560 GHz , ^{13}CO $J = 2 \rightarrow 1$ at 220.398 GHz, and ^{12}CO $J = 2 \rightarrow 1$ at 230.538 GHz. FLASH$^+$ was used in the 345 GHz band to map the ^{12}CO $J = 3 \rightarrow 2$ transition at 345.795 GHz. FLASH$^+$ was

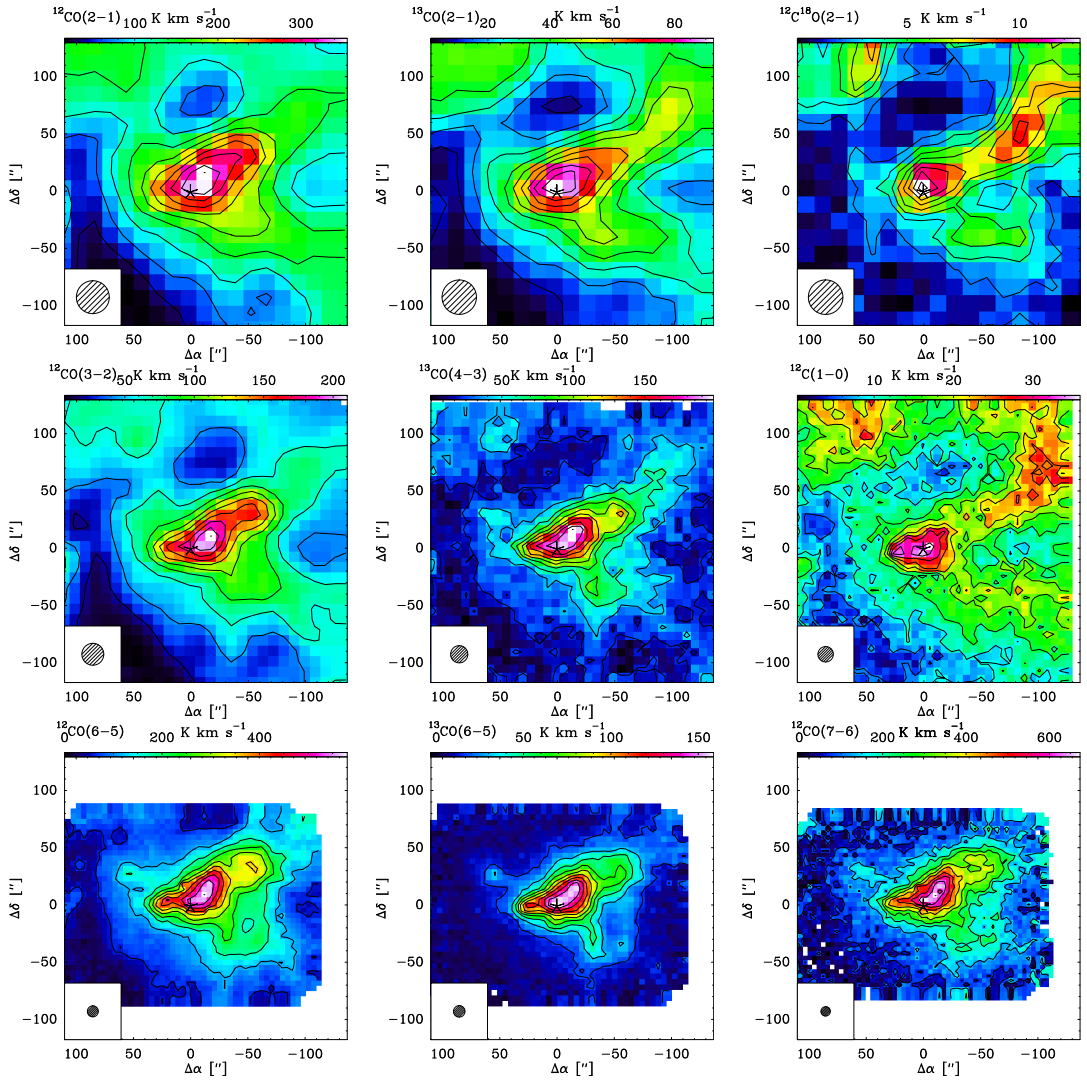

Figure 3.3: Colour maps of the integrated intensity of the $J = 2 \rightarrow 1$, $J = 3 \rightarrow 2$, $J = 6 \rightarrow 5$, and $J = 7 \rightarrow 6$ transitions of ^{12}CO, the $J = 2 \rightarrow 1$, $J = 4 \rightarrow 3$, and $J = 6 \rightarrow 5$ transitions of ^{13}CO, the $J = 2 \rightarrow 1$ line of C^{18}O and [C I] $1 \rightarrow 0$ toward Her 36. This corresponds to the central position ($\Delta\alpha = 0$, $\Delta\delta = 0$) at R.A.(J2000) = $18^{\rm h}03^{\rm m}40.3^{\rm s}$ and Dec.(J2000) = $-24°22'43''$, denoted with an asterisk. The contour levels of ^{12}C^{18}O and [C I] are 3 × rms in steps of 2 × rms, while those of other molecules are from 10% (> 3 × rms, given in Table 3.1) to 100% in steps of 10% of the corresponding peak emission given in Table 3.1. All maps are plotted using original beam sizes shown in the lower left of each map.

also used in the 460 GHz band to map the ^{13}CO $J = 4 \rightarrow 3$ transition at 440.765 GHz, C^{18}O $J = 4 \rightarrow 3$ at 439.088 GHz, and [C I] $^3P_1 \rightarrow {}^3P_0$ fine structure line at 492.160 GHz. The CHAMP$^+$ receiver was used to map ^{12}CO $J = 6 \rightarrow 5$ at 691.473 GHz and ^{13}CO $J = 6 \rightarrow 5$ at 661.067 GHz in the low-frequency subarray complemented by ^{12}CO $J = 7 \rightarrow 6$ at 806.651 GHz and ^{13}CO $J = 8 \rightarrow 7$ at 881.272 GHz in the high-frequency subarray.

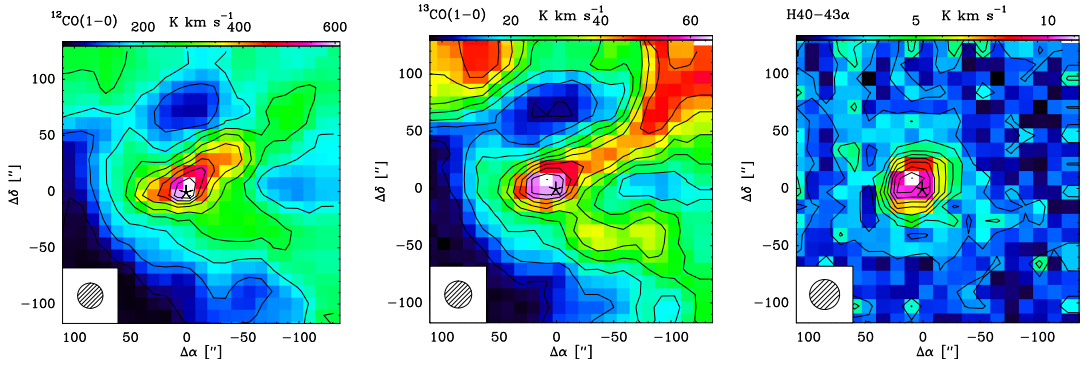

Figure 3.4: Color maps of the integrated intensity (left to right) of the $J = 1 \rightarrow 0$ transition of ^{12}CO, ^{13}CO and average of Hα40, 41, 42, and 43 lines toward Her 36, which is the central position ($\Delta\alpha = 0$, $\Delta\delta = 0$) at R.A.(J2000) = $18^h03^m40.3^s$ and Dec.(J2000) = $-24°22'43''$, denoted with an asterisk. The contour levels are 10% (> 3 $\times$ rms, given in Table 3.1) to 100% in steps of 10% of the corresponding peak emission given in Table 3.1. All maps are plotted using original beam sizes shown in the lower left of each map.

All maps shown in Fig. 3.3 were observed in OTF total power mode centered on R.A. $18^h03^m40^s.3$, Dec. $-24°22'43''$(J2000), which corresponds to the position of Her 36. The maps obtained from the observations carried out in July, September, and October 2016 have a size of 240″ x 240″. Maps that were obtained from the observations carried out in 2015 are comparatively smaller in size. We integrated 0.7 s per dump for all maps and enough coverages were performed to reach the rms noise levels as mentioned in Table 3.1. The offset position relative to the center at ($30'$, $-30'$) was chosen as reference, similar to the SOFIA observations. The pointing accuracy ($< 3''$) was maintained by pointing at bright sources such as RAFGL5254 and R Dor every 1 – 1.5 hrs. A forward efficiency $F_{\rm eff} = 0.95$ was used for all receivers, and the beam coupling efficiencies $B_{\rm eff} = 0.62$, 0.69, 0.63, 0.43, and 0.32 were used for the PI230, FLASH$^+$340, FLASH$^+$460, CHAMP$^+$660, and CHAMP$^+$810 receivers, respectively.

3.2.3 IRAM 30 m data

Observations of low-J ^{12}CO, ^{13}CO, and hydrogen recombination line observations were performed with the IRAM 30 m telescope in August 2016. We observed the whole 3 mm

Table 3.1: Line parameters of observed transitions.

Transition	Frequency (GHz)	$\eta_{\rm mb}$	$\theta_{\rm mb}('')$	Peak line flux (K km s^{-1})	rms (K km s^{-1})	Telescope
			^{12}CO			
$J = 1 \rightarrow 0$	115.271	0.73	22.5	610.2	1.1	IRAM 30m/EMIR
$J = 2 \rightarrow 1$	230.538	0.65	28.7	355.5	0.4	APEX/PI230
$J = 3 \rightarrow 2$	345.796	0.73	19.2	210.2	0.8	APEX/FLASH$^+$
$J = 6 \rightarrow 5$	691.473	0.43	9.6	580.1	4.0	APEX/CHAMP$^+$
$J = 7 \rightarrow 6$	806.652	0.34	8.2	673.4	19.0	APEX/CHAMP$^+$
$J = 11 \rightarrow 10$	1267.014	0.68	22.9	130.9	3.5	SOFIA/GREAT
$J = 13 \rightarrow 12$	1496.923	0.68	19.1	155.3	2.4	SOFIA/GREAT
$J = 16 \rightarrow 15$	1841.346	0.70	14.8	46.2	1.8	SOFIA/GREAT
			^{13}CO			
$J = 1 \rightarrow 0$	110.201	0.73	23.5	64.9	0.4	IRAM 30m/EMIR
$J = 2 \rightarrow 1$	220.399	0.65	30.1	92.6	0.6	APEX/PI230
$J = 4 \rightarrow 3$	440.765	0.59	15.0	198.1	2.5	APEX/FLASH$^+$
$J = 6 \rightarrow 5$	661.067	0.45	10.0	158.8	3.2	APEX/CHAMP$^+$
			C^{18}O			
$J = 2 \rightarrow 1$	219.561	0.65	30.2	12.7	0.6	APEX/PI230
			^{12}C			
$^3P_1 \rightarrow {}^3P_0$	492.160	0.59	13.5	34.0	1.8	APEX/FLASH$^+$
			^{12}C$^+$			
$^2P_{3/2} \rightarrow {}^2P_{1/2}$	1900.53	0.70	14.8	728.5	2.1	SOFIA/GREAT
			Hα			
H40 – 43α	80–90	0.73	≈ 26	11.2	0.2	IRAM 30m/EMIR

range using the EMIR receivers (Carter et al., 2012). We simultaneously mapped a region of 240″ x 240″, which is similar to the size of most other maps previously observed with SOFIA and APEX in the ^{12}CO and ^{13}CO $J = 1 \rightarrow 0$ transitions (Table 3.1) and the hydrogen recombination lines H40α to H43α at 99.023 GHz, 92.034 GHz, 85.688 GHz, and 79.912 GHz, respectively. Molecular high density tracers, which were also detected in our wide spectral band observation, will be analyzed in a subsequent paper.

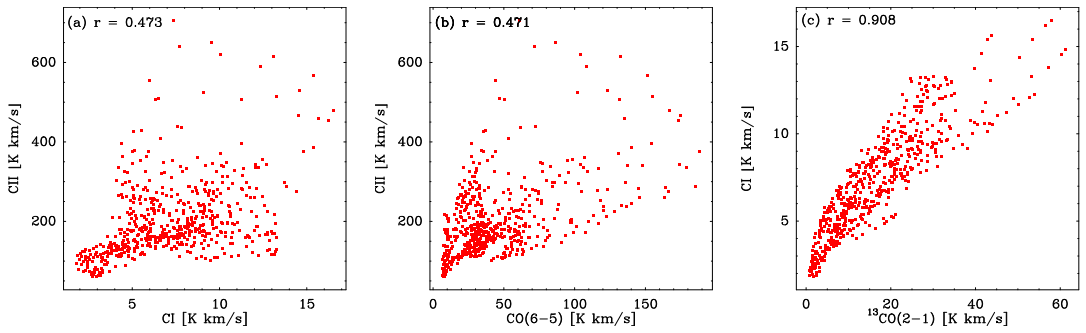

Figure 3.5: Scatter plots and correlation coefficients r between the velocity integrated intensity of (a) [C II] and [C I] (b) [C II] and the J = 6 → 5 transition of ^{12}CO, and (c) [C I] and the J = 2 → 1 transition of ^{13}CO. All data points were extracted from velocity integrated intensity maps convolved to the same beam size of 31″.

All maps shown in Fig. 3.4 were observed in OTF total power mode centered on Her 36. Each subscan lasted 25 s and the integration time on the off-source reference position was 5 s. The offset position relative to the center at (30′, −30′) was similar to

that used for the SOFIA and APEX mapping and the pointing accuracy ($< 3''$) was maintained by pointing at the bright calibrator 1757-240 every 1 – 1.5 hrs. A forward efficiency $F_{\rm eff} = 0.95$ and a beam coupling efficiency $B_{\rm eff} = 0.69$ were adopted for the EMIR receivers. These values were taken from the latest (2015) commissioning report[4].

All data reduction was performed using the CLASS and MIRA programs that are a part of the GILDAS[5] software package and all the observations are summarized in Table 3.1.

3.3 Results

3.3.1 Peak intensities of the molecular line emission

The maxima of the distributions of the velocity integrated intensities of the emission in the [C I] and [C II] lines and different transitions of ^{12}CO, ^{13}CO, and C^{18}O are presented in Table 3.1. Fig. 3.2 shows velocity integrated intensity maps of the ^{12}CO $J = 11 \rightarrow 10$, $13 \rightarrow 12$, and $16 \rightarrow 15$ transitions. The emission in all the lines has a similar spatial distribution and peaks are found at about the same offset position ($\Delta\alpha = 5.0''$, $\Delta\delta = 5.0''$) northwest of Her 36.

Figs. 3.3 and 3.4 show velocity integrated intensity maps of low- and mid-J transitions of ^{12}CO, ^{13}CO, and C^{18}O, i.e., the $J = 1 \rightarrow 0$, $2 \rightarrow 1$, $3 \rightarrow 2$, $6 \rightarrow 5$, $7 \rightarrow 6$ transitions of ^{12}CO, the $J = 1 \rightarrow 0$, $2 \rightarrow 1$, $4 \rightarrow 3$, and $6 \rightarrow 5$ transitions of ^{13}CO and the $J = 1 \rightarrow 0$ transition of C^{18}O. The intensities of the low-J transitions peak close to Her 36 ($\Delta\alpha = 0.0''$, $\Delta\delta = 0.0''$) for ^{12}CO mid-J transitions; the peaks shift toward the northwest of Her 36 with offsets of ($\Delta\alpha = -13.0''$, $\Delta\delta = 8.0''$). It seems like there is a systematic shift in the peak emission of CO transitions with low-J peaking near Her 36, mid-J peaking toward the northwest, while high-J lines peak again closer to Her 36. Nevertheless, all maps show at least a small offset toward the northwest and the emission from CO transitions becomes more and more compact with increasing J.

Figs. 3.2 and 3.3 show velocity integrated intensity maps of the [C II] $^2P_{3/2} \rightarrow {}^2P_{1/2}$ and [C I] $^3P_1 \rightarrow {}^3P_0$ transitions. [C I] peaks at Her 36 and is very bright toward the northwest of Her 36. [C II] peaks at an offset of ($\Delta\alpha = 30.6''$, $\Delta\delta = -1.6''$), which is toward the east of Her 36 and the emission extends even further. This extended emission comes from the part of the HII region that is illuminated by the stellar system 9 Sgr (Tothill et al., 2008).

Fig. 3.4 shows a velocity integrated intensity map of an average of the H40α to H43α hydrogen recombination lines. We have taken the average to obtain a better signal-to-noise ratio. The distribution or the radio recombination line emission agrees well with the 5 GHz continuum Very Large Array (VLA) interferometric map in

[4] www.iram.es/IRAMES/mainWIKI/IRAM30mEfficiencies
[5] www.iram.fr/IRAMFR/GILDAS/

Fig. 3.4 of Woodward et al. (1986) and the peak of the Hα lines is at ($\Delta\alpha = 10.0''$, $\Delta\delta = 9.0''$), close to the center of the Hourglass Nebula, which indicates the presence of hot ionized gas in the east of Her 36.

3.3.2 Correlation between ^{12}CO, ^{13}CO, [C I] and [C II]

As can be seen from the velocity integrated intensity maps, emission from [C II] is spread out the most as compared to [C I], ^{12}CO, and ^{13}CO. In order to visualize the correlation between these species, scatter plots of [C II] versus [C I], [C II] versus ^{12}CO $J = 6 \rightarrow 5$, and [C I] versus ^{13}CO $J = 2 \rightarrow 1$ are shown in Fig. 3.5. We chose CO 6 $\rightarrow$ 5 owing to its association with the warm PDR due to its higher upper level energy compared to low-J CO transitions, while we chose ^{13}CO 2 $\rightarrow$ 1 in particular, as its critical density is comparable to that of [C I]. [C II] is correlated the least with ^{12}CO $J = 6 \rightarrow 5$. The Pearson correlation coefficient is $r = 0.471$. Two branches appear to bud out in the upper left and lower right of this correlation. The upper left, where the [C II] emission intensifies for a slowly strengthening ^{12}CO $J = 6 \rightarrow 5$ emission, corresponds to the northeast of Her 36 where [C II] is more extended. The lower right, where ^{12}CO $J = 6 \rightarrow 5$ emission intensifies at a faster rate than [C II], corresponds to the southwest of Her 36, where ^{12}CO $J = 6 \rightarrow 5$ is much more prominent. The correlation of [C II] with [C I] has a correlation coefficient of $r = 0.473$ and again shows two different branches corresponding to different regions. The upper left, where [C II] emission gets brighter for an almost constant [C I] emission, corresponds to the northeast of Her 36. The branch in the lower right, similar to the situation shown in Fig. 3.5 (b), corresponds to the southwest of Her 36. In contrast to these correlations, [C I] is well correlated with ^{13}CO $J = 2 \rightarrow 1$ with $r = 0.908$. This resembles the case M17 SW, for which a correlation coefficient of [C I] with ^{13}CO $J = 2 \rightarrow 1$ was reported to be 0.942 (Pérez-Beaupuits et al., 2015).

3.3.3 Channel maps

In order to investigate the differences in the distribution of ionized and atomic carbon, channel maps of the $^2P_{3/2} \rightarrow ^2P_{1/2}$ transition of [C II] are compared to those of the [C I] $^3P_1 \rightarrow ^3P_0$ transition. Fig. 3.6 shows that the emission from [C II] (lower panels) is more spread out as compared to that from [C I] (upper panels). In the velocity range from 2 km s^{-1} to 6 km s^{-1} and 15 km s^{-1} to 17 km s^{-1} there is no emission from [C I] while there is emission from [C II] close to Her 36 and toward the east of it, respectively. In the range from 7 to 9 km s^{-1} both [C II] and [C I] emission are found toward the west. These structures extend further toward the northeast for higher velocities in the range of 12 km s^{-1} to 15 km s^{-1}. This is very similar to the case of M17 SW, where the [C II] channel map shows a strong spatial association with [C I] and CO channel maps only at intermediate 10 km s^{-1} to 24 km s^{-1} velocities. While at lower (<10 km s^{-1}) and higher (>24 km s^{-1}) velocity channels, [C II] emission is

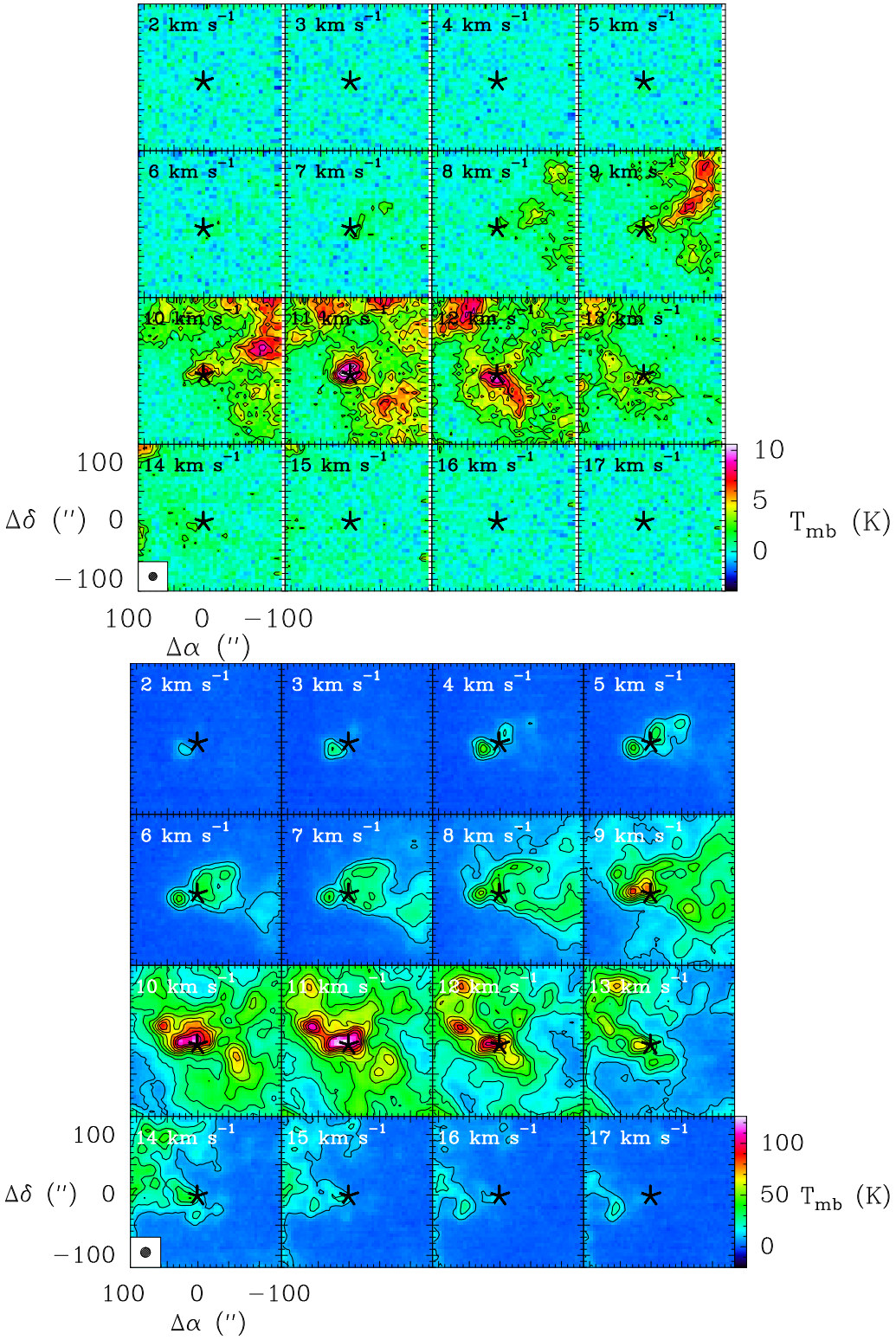

Figure 3.6: Velocity channel maps of the $^3P_1 \rightarrow {}^3P_0$ transition of [C I] (upper 16 panels) and the $^2P_{3/2} \rightarrow {}^2P_{1/2}$ transition of [C II] (lower 16 panels) in a range of 2 – 17 km s^{-1} with a channel width of 1 km s^{-1} toward Her 36, which is the central position ($\Delta\alpha$ = 0, $\Delta\delta$ = 0) at R.A.(J2000) = $18^h03^m40.3^s$ and Dec.(J2000) = $-24°22'43''$, denoted with a black asterisk. The contour levels of [C I] are 3 × rms in steps of 2 × rms, while those of [C II] are from 10% (> 3 × rms) to 100% in steps of 10% of the corresponding peak emission. All maps are plotted using original beam sizes shown in the lower left of both panels.

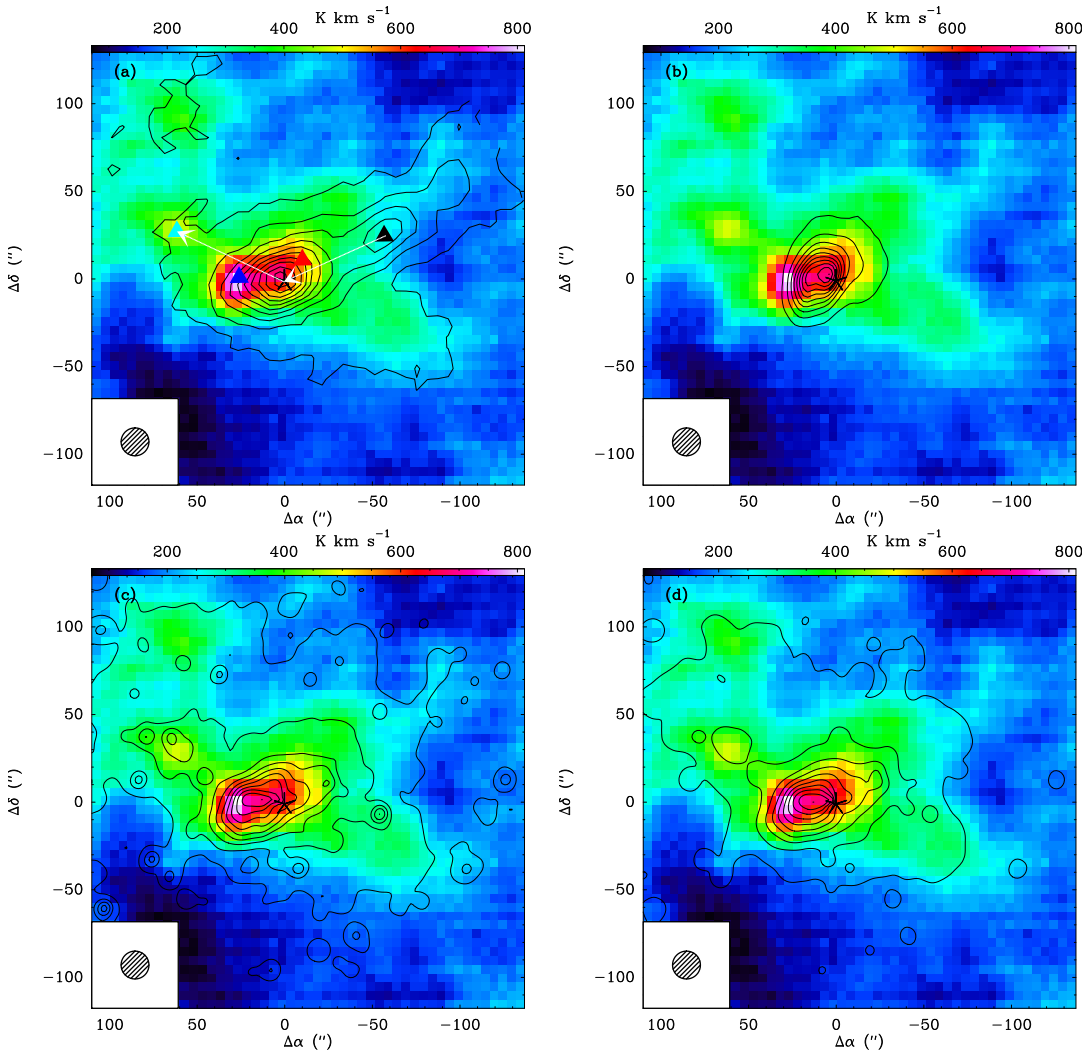

Figure 3.7: A [C II] velocity integrated intensity map overlaid with contours of (a) ATLASGAL 870 μm continuum emission. Important offset positions discussed in the text are indicated with triangles of different colors: black represents the secondary ATLASGAL peak deep inside the molecular cloud at ($\Delta\alpha$ =-53.0″, $\Delta\delta$ = 23.0″), red represents the emission peak of mid-J transitions of ^{12}CO and ^{13}CO at ($\Delta\alpha$ =-13.0″, $\Delta\delta$ = 8.0″), blue represents the peak of the [C II] 158 μm emission at ($\Delta\alpha$ = 30.0″, $\Delta\delta$ =-2.0″), and light blue represents the clump to the east of Her 36 observed in the channel maps of [C II] at ($\Delta\alpha$ = 60.0″, $\Delta\delta$ = 27.0″). The white arrows point along the molecular cloud in the west to the HII regions in the east of Her 36; (b) VLA 1.3 cm free-free continuum emission; (c) WISE 3.4 μm, and (d) WISE 4.6 μm mid-infrared continuum. Her 36 is the central position denoted with an asterisk. The contour levels are 5% to 95% in steps of 10% of the peak emission for (a) and 10% to 100% in steps of 10% of the peak emission for (b), (c), and (d).

mostly not associated with the other tracers of dense and diffuse gas (Pérez-Beaupuits et al., 2015). Notably, our [C II] channel maps show a clumpy structure at an offset of ($\Delta\alpha = 60.0''$, $\Delta\delta = 27.0''$) which is missing in the [C I] maps; this complements the argument that the east of Her 36 is comprised of hot gas and strong UV fields capable of ionizing carbon, i.e., it is part of an HII region. This is consistent with the Hα and 5 GHz continuum VLA interferometric maps presented by Woodward et al. (1986) in their figs. 1 and 4, which also have their peak intensities east from Her 36.

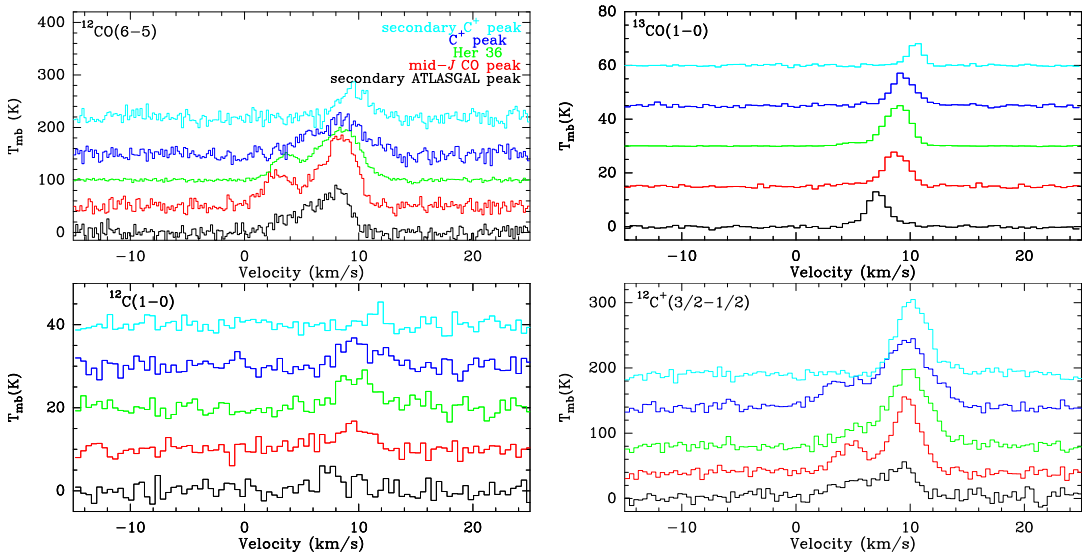

Figure 3.8: Line profiles at different offsets ($''$) relative to Her 36 are shown in different colors at five positions mentioned in the upper left plot. For the detailed positions, see Sect. 3.3.5. Upper panels: J = 6 → 5 ^{12}CO and J = 1 → 0 ^{13}CO spectra; lower panels: $^3P_1 \rightarrow {}^3P_0$ and $^2P_{3/2} \rightarrow {}^2P_{1/2}$ transitions of [C I] and [C II]. All spectra were extracted from their original beam sizes as mentioned in Table 3.1.

3.3.4 Ancillary data

For a multiwavelength view of M8 and in order to relate our observations to the dense and cold molecular cloud and the hot ionized gas in M8, we compared our data with observations obtained at other wavelength ranges. The surveys chosen for this comparison are as follows: Firstly, we extracted data from the 870 μm APEX Telescope Large Area Survey of the Galaxy (ATLASGAL) (**?**) performed with the APEX 12 m telescope using the Large APEX BOlometer CAmera (LABOCA). The dust continuum emission probes dense and cold clumps in the ISM of our Galaxy. Fig. 3.7 (a) shows our [C II] velocity integrated intensity map overlaid with the ATLASGAL dust continuum image that peaks at Her 36 and also traces the cold molecular cloud in the northwest. The dust emission morphology is similar to the ^{12}CO, ^{13}CO, and C^{18}O distribution. Secondly, we used data from the National Radio

Astronomy Observatory (NRAO)/ Very Large Array (VLA) Archive Survey (NVAS[6]). Fig. 3.7 (b) shows the [C II] velocity integrated intensity map overlaid with the 1.3 cm radio continuum image,[7] which peaks very close to Her 36 and traces free-free emission from the HII region NGC6523/33. This compact HII region, which is also traced by the H recombination lines with the IRAM 30 m telescope, is also shown in Fig. 3.4 (right panel). Thirdly, the Wide-field Infrared Survey Explorer (WISE) imaged the sky at four mid-infrared wavelengths. Fig. 3.7 (c) and (d) compare the [C II] velocity integrated intensity map with WISE 3.4 μm (band 1) and 4.6 μm (band 2) continuum images, which peak closer to the [C II] peak.

Overall, the mid-infrared emission that originates from hot dust shows the best agreement with the morphology seen in the [C II] image; both probe hot material from HII regions and warm surfaces of PDRs.

3.3.5 Spectra of ^{12}CO, ^{13}CO, [C I] and [C II] emission lines at different offsets

Fig. 3.8 shows a comparison between the spectra of ^{12}CO, ^{13}CO, [C I] and [C II] emission lines at different offsets relative to Her 36. Line parameters of Gaussian fits to profiles are reported in Table 3.2. In several cases the profiles show evidence of two velocity components that were fit separately. The ^{12}CO $J = 6 \rightarrow 5$ and ^{13}CO $J = 1 \rightarrow 0$ transitions are representative of the general appearance of all ^{12}CO and ^{13}CO line profiles discussed in this paper. The different offsets were chosen along a curved line from the molecular cloud in the west to the east of Her 36 (see Fig. 3.7 (a)): the secondary C^+ peak, which corresponds to the clump observed in the channel map of [C II] at ($\Delta\alpha = 60.0''$, $\Delta\delta = 27.0''$); the C^+ peak, which is the emission peak of the $^2P_{3/2} \rightarrow {}^2P_{1/2}$ transition of [C II] at ($\Delta\alpha = 30.0''$, $\Delta\delta = -2.0''$); Her 36 is located at ($\Delta\alpha = 0.0''$, $\Delta\delta = 0.0''$); the mid-J CO peak, which is the mid-J transition emission peak of ^{12}CO and ^{13}CO at ($\Delta\alpha = -13.0''$, $\Delta\delta = 8.0''$); and the secondary ATLASGAL peak arises from deep into the molecular cloud to the west traced by ATLASGAL at ($\Delta\alpha = -53.0''$, $\Delta\delta = 23.0''$).

A lower velocity (2 km s^{-1} – 6 km s^{-1}) component is spectrally resolved at several positions. The higher velocity component emission lines have blue-shifted wings in the molecular cloud in the west, while the emission is red-shifted toward the [C II] peak toward the east compared to their emission peaking at 9 km s^{-1} toward our reference position, Her 36. Furthermore, the peak of the lines shifts from the east to the west to lower velocities. The ^{12}CO and ^{13}CO line profiles are similar in being most intense with broadest line widths at the the mid-J transition emission peak of ^{12}CO and ^{13}CO ($\Delta\alpha = -13.0''$, $\Delta\delta = 8.0''$) and at Her 36 itself, while getting less intense with narrower line widths at the [C II] peak. The [C I] line profile gets most intense with

[6] http://archive.nrao.edu/nvas/

[7] NRAO/VLA Archive Survey, (c) 2005-2007 AUI/NRAO

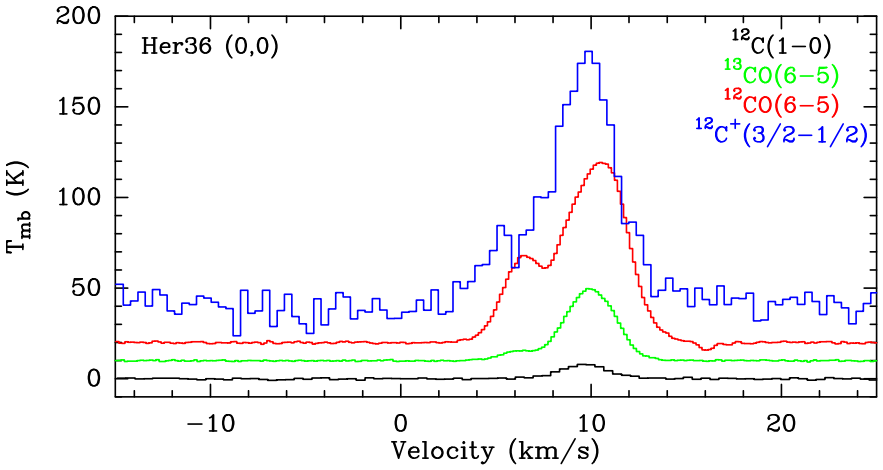

Figure 3.9: Line profiles toward Her 36 for [C I] $^3P_1 \rightarrow {}^3P_0$, ^{13}CO $J = 6 \rightarrow 5$, ^{12}CO $J = 6 \rightarrow 5$, and [C II] $^2P_{3/2} \rightarrow {}^2P_{1/2}$. All spectra are extracted from maps that were convolved to the same beam size of 15″.

broadest line width toward Her 36 itself with almost no emission from the clumpy structure in the HII region at an offset of ($\Delta\alpha = 60.0''$, $\Delta\delta = 27.0''$). As can also be seen from the comparison of various molecular transitions at Her 36 in Fig. 3.9, CO and [C I] are not associated with [C II] at lower and higher velocities (see also Figs. 3.5 and 3.6). This is very similar to M17 SW as reported by Pérez-Beaupuits et al. (2015), where [C II] is not associated with other gas tracers at lower and higher velocities.

3.4 Analysis

In this section we determine the temperature and density in the PDR of M8 with several complementary methods. We start by using the data for the $J = 6 \rightarrow 5$ transition of CO, which has the highest angular resolution, to estimate excitation temperatures and column densities throughout the PDR as probed by the mid-J CO emission.

3.4.1 Excitation temperature and column density estimates

A detailed description of spectral line radiative transfer relevant here can be found in Draine (2011) and Mangum & Shirley (2016). For a constant excitation temperature $T_{\rm ex}$, we can integrate the radiative transfer equation to obtain the observable Rayleigh-Jeans equivalent temperature $T_{\rm R}^{*}$ (Eq. 1 in Peng et al., 2012). The background radiation temperature comprises the cosmic background radiation of 2.73 K and the radiation from warm dust. The latter was calculated using the results from the Spectral and Photometric Imaging Receiver (SPIRE) of the European Space Agency (ESA) Herschel Space observatory. Data obtained in the second band at 350 μm (close to the ^{12}CO $7 \rightarrow 6$ line) wavelength was used. The maximum intensity in the analyzed

Table 3.2: ^{12}CO, ^{13}CO, [C I] and [C II] line parameters.

Offset (″)[a]	V (km s^{-1})	ΔV (km s^{-1})	$T_{\rm peak}$[b](K)
^{12}CO $J = 6 \rightarrow 5$			
(−40, 35)	10.33 (0.06)	3.62 (0.16)	77.24
(−13, 8)	5.92 (0.10)	3.30 (0.26)	58.41
	10.43 (0.04)	2.92 (0.10)	134.43
(0, 0)	6.39 (0.03)	2.42 (0.07)	45.67
	10.42 (0.02)	3.58 (0.04)	97.94
(30, −2)	10.28 (0.09)	4.73 (0.20)	62.60
(60, 27)	11.49 (0.07)	2.51 (0.17)	53.77
^{13}CO $J = 1 \rightarrow 0$			
(−40, 35)	8.47 (0.04)	3.00 (0.11)	8.26
(−13, 8)	8.76 (0.03)	2.58 (0.08)	12.61
(0, 0)	8.91 (0.01)	2.68 (0.03)	15.16
(30, −2)	9.37 (0.03)	2.48 (0.09)	11.15
(60, 27)	10.48 (0.02)	1.45 (0.05)	8.46
^{12}C $^3P_1 \rightarrow {}^3P_0$			
(−40, 35)	9.40 (0.63)	5.91 (2.16)	2.84
(−13, 8)	9.47 (0.25)	3.63 (0.63)	5.62
(0, 0)	9.89 (0.18)	3.86 (0.47)	7.65
(30, −2)	10.05 (0.30)	4.01 (0.64)	5.45
(60, 27)	11.80 (0.09)	0.68 (0.35)	5.85
^{12}C$^+$ $^2P_{3/2} \rightarrow {}^2P_{1/2}$			
(−40, 35)	5.40 (0.14)	2.84 (0.30)	33.45
	9.76 (0.11)	3.80 (0.31)	45.05
(−13, 8)	4.92 (0.10)	3.18 (0.25)	43.04
	9.71 (0.04)	2.89 (0.10)	110.50
(0, 0)	5.12 (0.23)	3.31 (0.57)	24.97
	9.94 (0.06)	4.11 (0.14)	114.49
(30, −2)	3.88 (0.16)	4.01 (0.36)	37.66
	9.72 (0.07)	4.86 (0.16)	100.10
(60, 27)	10.22 (0.04)	3.34 (0.09)	112.83

[a] The reference position is that of Her 36.
[b] In units of main beam brightness temperature.

region around Her 36 is about 1200 MJy/sr near the dense molecular cloud, which corresponds to a Rayleigh-Jeans equivalent brightness temperature of about 0.06 K from dust. Thus, the total contribution from dust and background can be neglected as it contributes $\leq 1\%$ to the resulting $T_{\rm R}^*$.

Assuming that the excitation temperature for ^{12}CO and ^{13}CO is the same and ^{12}CO is optically thick,

$$\frac{T_{\rm R}^{*}(^{12}{\rm CO})}{T_{\rm R}^{*}(^{13}{\rm CO})} = \frac{1}{1 - e^{-\tau(^{13}{\rm CO})}}\,. \tag{3.1}$$

The excitation temperature of the ^{12}CO $J = 6 \rightarrow 5$ transition can be estimated by further assuming a beam filling factor of unity, i.e., $T_{\rm R}^{*} = T_{\rm MB}$. This equation is written as

$$T_{\rm ex} = 33.2 \left[\ln\left(1 + \frac{33.2}{{\rm T_{MB}}(^{12}{\rm CO})}\right)\right]^{-1} {\rm K}\,, \tag{3.2}$$

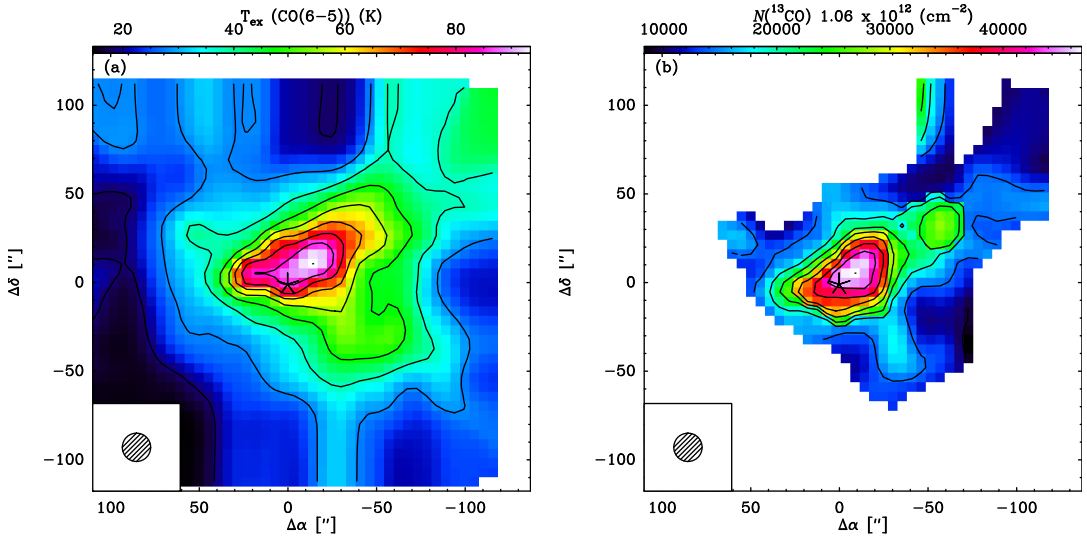

Figure 3.10: For the $J = 6 \rightarrow 5$ transition (a) shows the excitation temperature of ^{12}CO, which is assumed to be equal to that of ^{13}CO and (b) shows the column density of ^{13}CO. The asterisk represents Her 36, which is the central position ($\Delta\alpha = 0$, $\Delta\delta = 0$) at R.A.(J2000) = $18^{\rm h}03^{\rm m}40.3^{\rm s}$ and Dec.(J2000) = $-24°22'43''$. The contour levels are 10% to 100% in steps of 10% of the corresponding peak emissions. All maps are plotted using original beam sizes shown in the lower left of each map.

where $T_{\rm MB}$ is the main beam brightness temperature in K that is estimated from the peak temperature map of ^{12}CO $J = 6 \rightarrow 5$ transition. The resulting $T_{\rm ex}$ distribution is shown in Fig. 3.10 (a). Formally, we show lower limits to the excitation temperature due to the assumption of a beam filling factor of unity. It is highest immediately in the northwest of Her 36 and decreases with distance from the star.

Using the computed $T_{\rm ex}$ and the main beam brightness temperature $T_{\rm MB}$ estimated from the peak temperature map of ^{13}CO $J = 6 \rightarrow 5$, the total column density (Fig. 3.10 (b)) of ^{13}CO can be calculated over the complete velocity range of the source from

$$N(^{13}\mathrm{CO}) = 1.06 \times 10^{12}(T_{\rm ex} + 0.88)\ exp\left(\frac{116.2}{T_{\rm ex}}\right) \int T_{\rm MB}(^{13}\mathrm{CO})\mathrm{dv\ cm^{-2}}\,, \qquad (3.3)$$

where $T_{\rm ex}$ is in K and $T_{\rm MB}$ dv is in K kms^{-1}. Fig. 3.10 (b) shows the resulting ^{13}CO total column density with a peak value of $\sim 5 \times 10^{16}$ cm^{-2} northwest of Her 36. This results in a H_2 column density $N(H_2)$ of $\sim 3.7 \times 10^{22}$ cm^{-2} adopting an isotopic abundance ratio [^{12}CO/^{13}CO] of ~ 63 (Milam et al., 2005) and a CO abundance ratio [^{12}CO/H_2] of $\sim 8.5 \times 10^{-5}$ (Tielens, 2010). The mass of the warm CO gas can be computed by integrating the column density over the whole clump in a region of 3.12 arcmin^2, which results in a mass of ~ 467 M$_\odot$. Complementary to this, the cold gas mass in a region of 5.1 arcmin^2 has an estimated value of 10^3 M$_\odot$, calculated from a flux of ~ 133 Jy at 870 μm measured with ATLASGAL (Schuller et al., 2009) assuming an absorption coefficient of $k_\nu = 1.85$ g cm^2 and a temperature of 23 K (Urquhart et al., 2018), and not including potential uncertainties in the choice of these values. However, these mass estimations have an error of $\sim 26\%$, which accounts for errors of $\sim 16\%$ from the distance to the star (Tothill et al., 2008) and $\sim 20\%$ from the calibration.

3.4.2 Rotational diagrams of ^{13}CO

With observations of CO lines with different J, rotational diagrams can be used to study the excitation of the CO emitting gas. In a rotational diagram or Boltzmann plot the natural logarithm of the column density $N_{\rm u}/g_{\rm u}$ of different lines is plotted against their upper energies $E_{\rm up}/k$. Here $g_{\rm u}$ is the degeneracy of the upper energy level, ($\equiv 2J + 1$), and k is the Boltzmann constant. For a single temperature and optically thin emission these data points fall onto a straight line. Deviations from a straight line indicate then either optical depth effects or temperature gradients in the clouds. A complete derivation of rotational diagrams for a Local Thermodynamic Equilibrium (LTE) case can be found in Goldsmith & Langer (1999).

Firstly, by assuming ^{13}CO to be optically thin, i.e., the optical depth correction term, C_τ is unity in Eq. 24 of Goldsmith & Langer (1999), we plot $\ln N_{\rm u}^{\rm thin}/g_{\rm u}$ versus $E_{\rm u}/K$ as shown in Fig. 3.11 in black for the five ^{13}CO lines observed toward Her 36. A curvature in a rotational diagram can be due to optical depth effects, therefore we estimate the expected optical depths for the computed column density from Eq. 25 of Goldsmith & Langer (1999) and apply the optical depth corrections C_τ that lead to the corrected diagram as shown in red in Fig. 3.11. The new temperatures and column densities are then calculated as shown in Table 3.3. Further iterations would lead to corrections smaller than the error bars. After the optical depth correction the

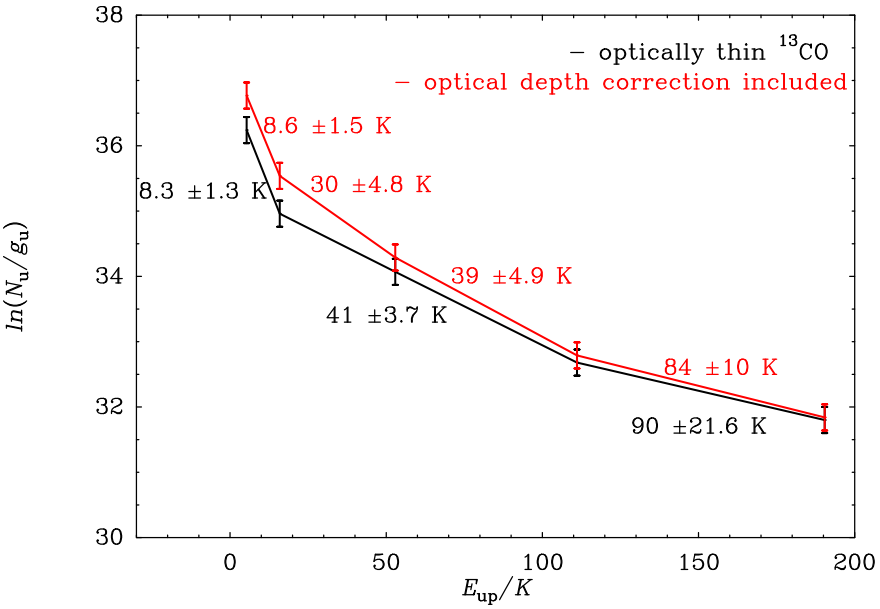

Figure 3.11: Rotational diagrams of $J = 1 \rightarrow 0$, $J = 2 \rightarrow 1$, $J = 4 \rightarrow 3$, $J = 6 \rightarrow 5$, and $J = 8 \rightarrow 7$ transitions of ^{13}CO at Her 36. Shown in black is the rotational diagram when ^{13}CO is assumed to be optically thin. In red the rotational diagram is shown including the optical depth correction factors. Rotation temperatures obtained from different slopes are indicated. Values of the velocity integrated intensities for different transitions were extracted from maps convolved to the same resolution of 31″. The error bars were calculated from the maximum noise level of the integrated intensities of individual transitions and from calibration uncertainties of 20%

.

curvature in the rotational diagram remains and indicates temperature gradients in the gas, as expected in a PDR.

The $J = 1 \rightarrow 0$ and $J = 2 \rightarrow 1$ transitions of ^{13}CO seem to originate from colder gas, while the $J = 4 \rightarrow 3$ and $J = 6 \rightarrow 5$ transitions probe hotter gas, which agrees with the analysis carried out for $J = 6 \rightarrow 5$ in Sect. 3.4.1. The $J = 8 \rightarrow 7$ transition appears to originate from the hottest gas.

3.4.3 RADEX modeling

We used the non-LTE radiative transfer program RADEX (van der Tak et al., 2007) to verify the calculations carried out in Sects. 3.4.1 and 3.4.2, which assumed LTE to determine the temperatures and densities. The RADEX program uses the escape probability approximation for a homogeneous medium and takes into account optical depth effects. We chose a uniform sphere geometry. The Leiden Molecular and Atomic Database[8] (LAMDA; Schöier et al. 2005) provides rates coefficients for collisions of

[8]http://www.strw.leidenuniv.nl/moldata/

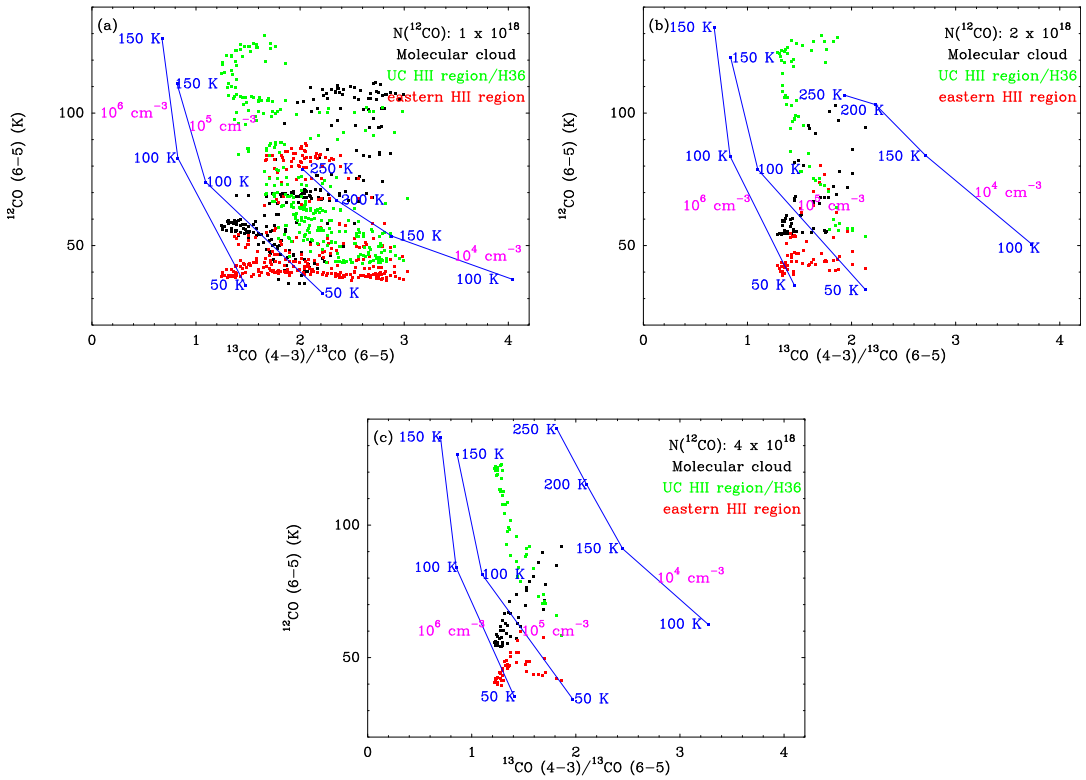

Figure 3.12: For 3 different ^{12}CO column densities, RADEX modeling results are shown for ^{12}CO $J = 6 \rightarrow 5$ peak main-beam brightness temperatures and corresponding ^{13}CO $J = 4 \rightarrow 3/^{13}$CO $J = 6 \rightarrow 5$ ratios. The blue lines denote the RADEX modeling results for different kinetic temperatures at 3 different volume densities, and color points represent data from near the HII region, PDR, and molecular cloud (see Sect. 3.4.3). Each point denotes a ^{12}CO $J = 6 \rightarrow 5$ temperature and ^{13}CO $J = 4 \rightarrow 3/^{13}$CO $J = 6 \rightarrow 5$ temperature ratio obtained from a single pixel. Data points are extracted from peak temperature maps convolved to the same resolution of 16″. (a) The data points plotted are obtained for a ^{12}CO column density range of 8×10^{17} – 1.8×10^{18} cm^{-2} and for modeling the chosen input ^{12}CO column density is 1×10^{18} cm^{-2}. (b) The data points plotted are obtained for a ^{12}CO column density range of 1.8×10^{18} – 3.5×10^{18} cm^{-2} and for the modeling the input ^{12}CO column density is 2×10^{18} cm^{-2}. (c) The data points plotted are obtained for a ^{12}CO column density range of 3.5×10^{18} – 5.1×10^{18} cm^{-2} and for the modeling input the ^{12}CO column density is 4×10^{18} cm^{-2}.

Table 3.3: Physical parameters calculated from rotational diagrams.

Optically thin ^{13}CO		Correction factor included	
$T_{\rm rot}$[a](K)	$N(^{13}\mathrm{CO})$ (cm^{-2})	$T_{\rm rot}$[a](K)	$N(^{13}\mathrm{CO})$ (cm^{-2})
8.3 ± 1.3	3.6×10^{16}	8.6 ± 1.5	6.2×10^{16}
41 ± 3.7	3.6×10^{16}	30 ± 4.8	5.4×10^{16}
90 ± 21.6	1.9×10^{16}	39 ± 4.9	4.6×10^{16}
		84 ± 10	2.1×10^{16}
Transition	τ	Transition	τ
$J = 1 \rightarrow 0$	1.68	J = 1 → 0	1.92
$J = 2 \rightarrow 1$	1.78	J = 2 → 1	2.20
$J = 4 \rightarrow 3$	1.25	J = 4 → 3	0.74
$J = 6 \rightarrow 5$	1.12	J = 6 → 5	0.28
$J = 8 \rightarrow 7$	1.04	J = 8 → 7	0.10

[a] Calculated for different gradients with their errors in the plot as indicated in Fig. 3.11.

CO and H_2 used in the modeling. ^{12}CO and ^{13}CO transitions were modeled taking their line width from the average spectra of our data, i.e., 4 and 3 km s^{-1}, respectively. As input parameters we computed grids in temperature and volume density with a background temperature of 2.73 K, kinetic temperatures in the range of 50 – 250 K and H_2 densities in the range of 10^4 – 10^8 cm^{-3}. For a linear molecule line ratios from different J depend on both temperature and density. To break this degeneracy, we computed with RADEX not only the line ratio of two ^{13}CO transitions but also the temperature of the ^{12}CO line. The latter is optically thick, probes the excitation temperature (cf. Sect. 3.4.1), and can therefore be used to break the degeneracy between temperature and density.

In our first approach to determine the dominant kinetic temperatures and densities in M8 near Her 36, we selected from the CO maps data points for column densities of ^{12}CO in three ranges as follows: (a) 8×10^{17} – 1.8×10^{18} cm^{-2}, (b) 1.8×10^{18} – 3.5×10^{18} cm^{-2}, and (c) 3.5×10^{18} – 5.1×10^{18} cm^{-2}. These ranges were estimated from the LTE calculations carried out in Sects. 3.4.1 and 3.4.2. Another criterium for selection of these data points aims at selecting the most conspicuous regions inside the maps. The molecular cloud region consists of all data points in an area of $15'' \times 15''$ around the mid-J CO peak, the UC HII region/ Her 36 encompasses all data points in an area of $20'' \times 20''$ around Her 36, and the eastern HII region has data points in an area of $20'' \times 20''$ around the [C II] peak.

Fig. 3.12 shows the $J = 4 \rightarrow 3$ and $J = 6 \rightarrow 5$ line ratios of ^{13}CO versus the $J = 6 \rightarrow 5$ ^{12}CO line temperature for both the measured data points in the maps and the

results of the RADEX computation of the density/temperature grid. The H_2 number densities in most of the regions are in the range of $\sim 10^4$ – 10^6 cm^{-3}. High densities are obtained for the molecular cloud and the eastern HII region, while the region consisting of the bright stellar system Her 36 and the ultracompact HII region has densities in the range of 10^4 – 10^5 cm^{-3}. The kinetic temperatures from the modeling results are in a range of 100 – 250 K for 10^4 cm^{-3} and in a range of 50 – 150 K for 10^5 – 10^6 cm^{-3}.

In order to include all CO lines toward several positions in the RADEX analysis, their intensities as a function of J are compared to RADEX results in Fig. 3.13. To fit the modeling results to the observed data points we varied the column densities of ^{12}CO and ^{13}CO. While for ^{12}CO a column density of 4×10^{18} cm^{-2} was chosen, for ^{13}CO a column density of 8×10^{16} cm^{-2} could make the modeling results fit the data points. This ^{13}CO column density exceeds the value obtained by the LTE calculations and corresponds to a ^{12}CO/^{13}CO ratio of 50. While this is lower than the assumed value of 63 in Sect. 3.4.1, it is still within the typical scatter of this ratio in the ISM (Milam et al., 2005). The ^{12}CO and ^{13}CO observed data is compared to the RADEX model at the peak of the mid-J CO transitions in the molecular cloud, at Her 36 and at the emission peak of [C II] . Panels (a) and (b) of Fig. 3.13 show results with the kinetic temperature varied from 50 – 250 K and keeping the H_2 density fixed at 10^5 cm^{-3}, while panels (c) and (d) show results in which the H_2 density is varied from 10^4 – 10^8 cm^{-3} while keeping the kinetic temperature fixed at 120 K.

It can be seen that no single kinetic temperature or H_2 density can fit all the observed data points. This suggests solutions with kinetic temperatures in the range of 100 – 150 K and H_2 densities to be in the range of 10^4 – 10^6 cm^{-3}. Such a spread in the ambient temperature was also implied by the rotational diagram analysis. Furthermore, these values are similar to the temperature and density ranges found in OMC 1 (Peng et al., 2012).

3.4.4 CO, [C I] and [C II] luminosities

We obtained the total luminosities of the CO spectral line energy distributions (SLED) and of the [C I] 609 μm and [C II] lines over the total observed region seen in the maps in Figs. 3.2, 3.3, and 3.4, as derived by Solomon et al. (1997); Carilli & Walter (2013). We scaled the luminosity for galactic sources, i.e.,

$$L = 1.04 \times 10^{-9} S \Delta V \nu D_{\rm L}^2 \,, \tag{3.4}$$

where L is the line luminosity in L$_\odot$, $S\ \Delta\ V$ is the velocity integrated flux in Jy km s^{-1}, ν is the transition frequency in GHz, and $D_{\rm L}$ is the distance in kpc. A total CO luminosity of $L_{\rm CO} = 9.5$ L$_\odot$ was calculated for the observed transitions and by accounting for the luminosities of the missing transitions. A [C I] 609 μm line luminosity of $L_{\rm [C\ I]} = 0.11$ L$_\odot$ was obtained, which is a lower limit to the total

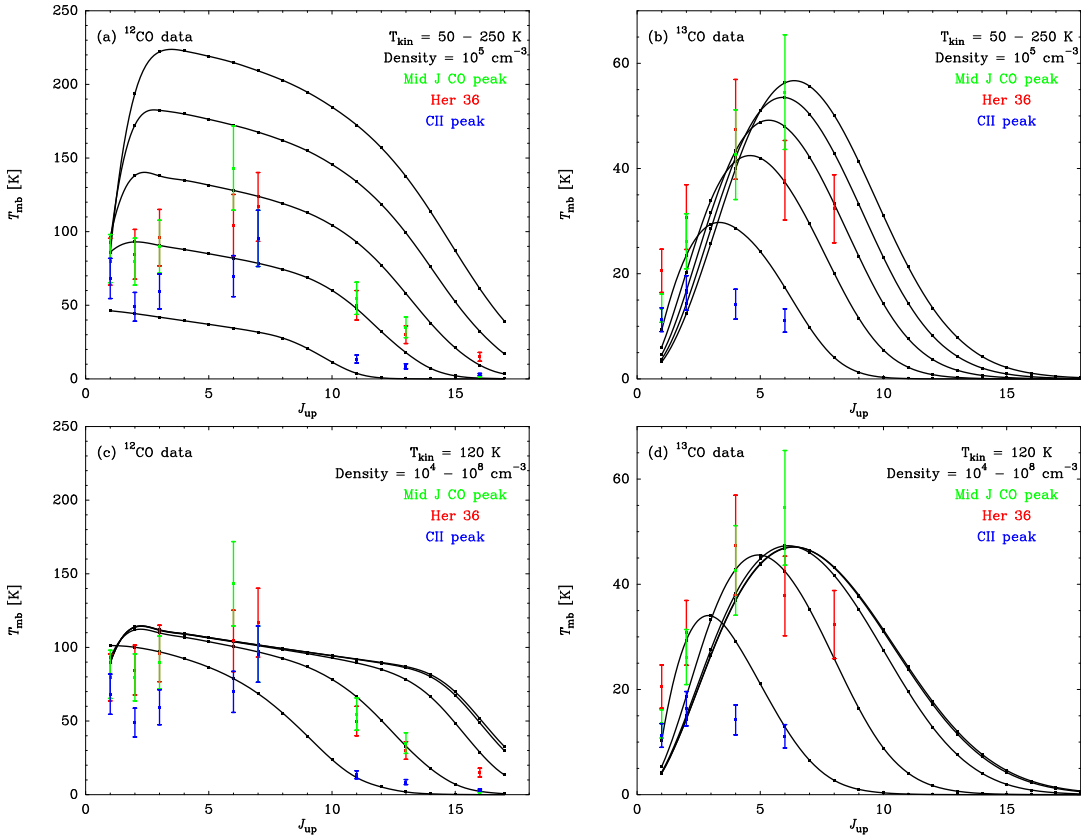

Figure 3.13: Results obtained from RADEX modeling for ^{12}CO and ^{13}CO at the mid-J CO peak ($\Delta\alpha = -13.0''$, $\Delta\delta = 8.0''$), at Her 36 ($\Delta\alpha = 0''$, $\Delta\delta = 0''$) and at the [C II] peak ($\Delta\alpha = 30.0''$, $\Delta\delta = -2.0''$). Our observed data points are in green, red, and blue and are extracted from peak temperature maps convolved to the same resolution of $31''$. The column densities used in the modeling are for ^{12}CO 4×10^{18} cm^{-2} and 8×10^{16} cm^{-2} for ^{13}CO. Panels (a) and (b) show results obtained by varying the kinetic temperature from 50 – 250 K in steps of 50 K and keeping the density fixed at 10^5 cm^{-3}; panels (c) and (d) show results obtained by varying the H_2 density from 10^4 – 10^8 cm^{-3} in steps by a factor of 10 and keeping the kinetic temperature fixed at 120 K.

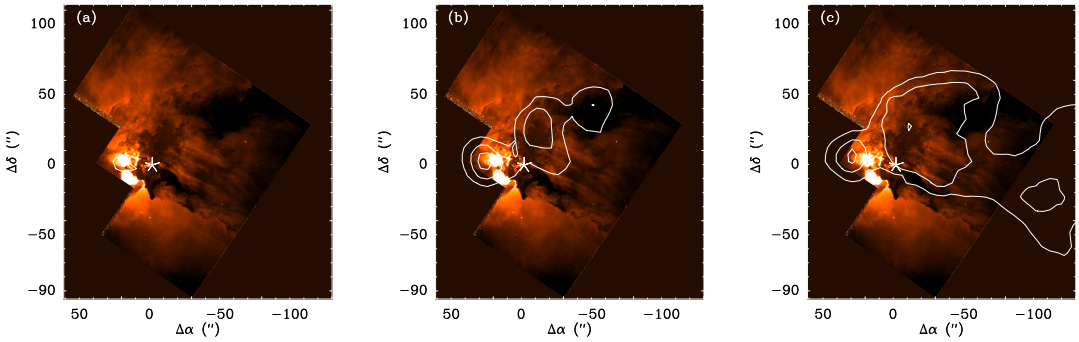

Figure 3.14: HST F487N (4865 Å) image of Her 36 and its surroundings overlaid with [C II] channel map contours (in white) at (a) 2 km s^{-1}, (b) 5 km s^{-1}, and (c) 7 km s^{-1} to show the progression of the foreground material at lower velocities. Her 36 is the central position ($\Delta\alpha = 0$, $\Delta\delta = 0$) at R.A.(J2000) denoted with an asterisk at R.A.(J2000) = $18^{h}03^{m}40.3^{s}$ and Dec.(J2000) = –24°22′43″, with the hourglass nebula representing the two bright hotspots about $\sim 15''$ to the east. Contour levels are 10% to 100% in steps of 10% of the peak emission observed at the channel with 10 km s^{-1} velocity.

[C I] luminosity since the [C I] 370 μm line was not observed. The estimated [C II] luminosity is $L_{[\mathrm{C\ II}]} = 95.8\ \mathrm{L}_{\odot}$. Similar to the mass estimations in Sect. 3.4.1, these luminosity estimations have an error of $\sim 26\%$.

3.5 Discussion

3.5.1 Overview of the PDR and HII region around Her 36

In Fig. 3.14, we present a F487N filtered 4865 Å HST image[9] (observation ID number: 6227, observed in the year 1995) of Her 36 and its surroundings overlaid with contours from low velocity [C II] channel maps. The [C II] at the lowest velocity (2 km s^{-1}) peaks at the Hourglass Nebula slightly to the east of Her 36. With increasing velocities, the [C II] follows the dark patches in the HST images that form a foreground veil covering parts of the bright nebulosity excited by Her 36. The strong correlation of [C II] and foreground absorption is particularly evident at the sharp southern edge of the veil seen at 7 km s^{-1}. Therefore we suggest that the low velocity [C II] probes directly the gas of the veil that forms a foreground PDR illuminated by Her 36. On a fainter level, weak emission from this veil is also seen in the CO maps at low velocities (5 – 7 km s^{-1}).

This foreground veil is receding away from Her 36 toward us and to the west with a change in the line-of-sight velocity. This is consistent with both high velocity

[9]Based on observations made with NASA/ESA Hubble Space Telescope, and obtained from the Hubble Legacy Archive, which is a collaboration between the Space Telescope Science Institute (STScI/NASA), the Space Telescope European Coordinating Facility (ST-ECF/ESA) and the Canadian Astronomy Data Centre (CADC/NRC/CSA).

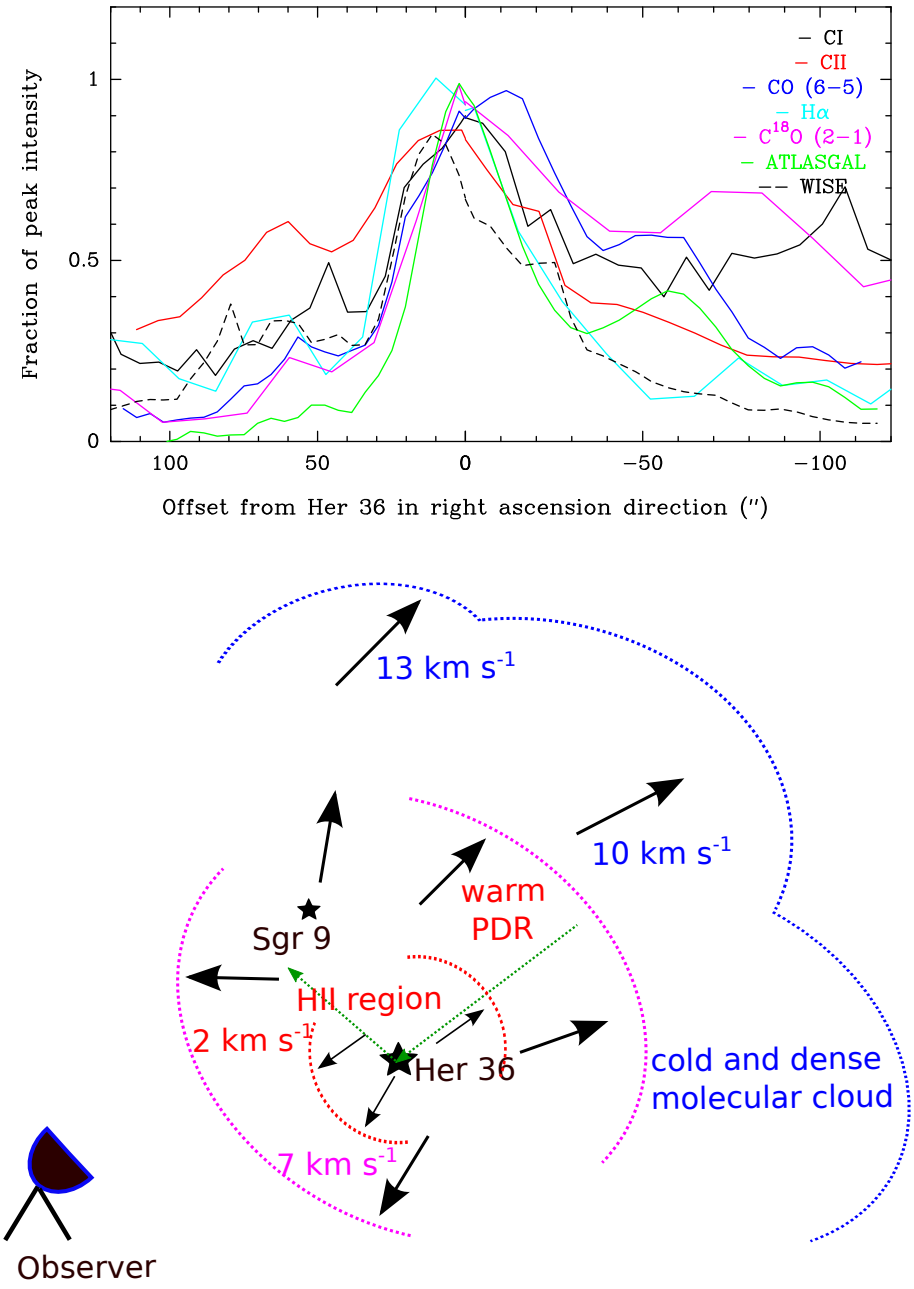

Figure 3.15: Left: Velocity integrated intensities normalized to their value at peak vs. offset (″) from Her 36 along the green arrows shown in the right. They follow a path from the second ATLASGAL peak at (−53″, 23″) to the second [C II] peak at (60″, 27″) via Her 36 at (0″, 0″). Plots are shown for [C II], [C I], $J = 6 \rightarrow 5$ ^{12}CO, $J = 2 \rightarrow 1$ C^{18}O, Hα, ATLASGAL 870 μm, and WISE 3.4 μm emission; Right: Schematic diagram of the prominent optical features of M8 pertinent to the discussion in this paper. The cold and dense molecular cloud is in the background shown in blue. The foreground gas of the warm PDR veil is receding away from Her 36 (~ 9 km s^{-1}) with lower velocities ($2 - 7$ km s^{-1}), while the HII region is powered by both stellar systems, Her 36 and 9 Sgr.

red-shifted and low velocity blue-shifted emission of Hα, [N II] and [S II] doublets, [O III], and absorption lines of the sodium D doublet as measured by Damiani et al. (2017). Assuming optically thin emission from [C II] in this warm veil in the velocity range of 2 – 7 km s^{-1} and a kinetic temperature of 500 K (Tielens & Hollenbach, 1985), we calculated the [C II] column density using Eq. A.1 with a peak value of $\sim 9.6 \times 10^{17}$ cm^{-2} at an offset of ($\Delta\ \alpha = 30''$, $\Delta\ \delta = 10''$) from Her 36. Taking C/H $\sim 1.2 \times 10^{-4}$, assuming that all the carbon is in ionized form and from the column density of H_2, $N(H_2) = 9.4 \times 10^{20}$ cm^{-2} (A_v/mag) (Kauffmann et al., 2008), we derived the visual extinction A_v. A maximum extinction of $A_v \sim 4.25$ is obtained at the same position where the [C II] column density peaks and the values get lower around it. This position is the same as position 13 in Fig. 5 of Woodward et al. (1986), where an $A_v \sim 3.9$ was calculated.

In Fig. 3.15 (left) we show how the intensity of various tracers evolves along a path from the direction of 9 Sgr to Her 36 and then continuing to the northwest along the molecular cloud. Toward the northeast [C II] and the mid-IR WISE emission dominate, probing the extended HII regions toward 9 Sgr and the resulting PDR. All of the tracers peak on or close to Her 36, showing the tight spatial correlation between the ultracompact HII region (as seen in the recombination line), a dense clump in the larger scale molecular cloud (870 μm dust and molecular emission), and the bright PDR illuminated by Her 36 ([C II] and WISE). To the northwest, emission from the molecular cloud dominates with the second dense but colder clump at an offset of about 70$''$ from Her 36. [C I] diffuse emission is very extended in this region.

Taking this into consideration along with our analysis of the morphology carried out in Sects. 3.3 and 3.4, we propose a geometry of the region illuminated by Her 36 and 9 Sgr as presented in Fig. 3.15 (right). We propose that the cold dense molecular cloud is behind the bright stars Her 36 and 9 Sgr. Her 36 is still much closer to the dense part of the cloud in which it was born; in fact the foreground veil is part of the original cloud accelerated toward us by the strong radiation and wind of Her 36, showing the expansion of the nebula, blue shifted with respect to the molecular cloud (3 – 7 km s^{-1}) moving away from Her 36 ($\sim$ 9 km s^{-1}) toward the observer and the west, while the red-shifted (11 – 13 km s^{-1}) [C II] probes the background material toward the northeast of Her 36. The ultracompact HII region is fueled by Her 36 around its vicinity and the more extended diffuse HII region by 9 Sgr toward the east (Tothill et al., 2008).

3.5.2 Comparison with PDR of the Orion Bar

The Orion Bar is a well-known PDR and its properties are described in depth by Hollenbach & Tielens (1997) and Walmsley et al. (2000). It is part of the OMC-1 core at the edge of M42 and is illuminated by young massive stars, which form a trapezium at the center of the Orion Nebular Cluster, mainly from θ^1 C, which is a O5 – O7 star. Also, the PDR appears to be located at the edge of the HII blister tangential to the line of sight (Peng et al., 2012). A comparison of L_{CO2-1}, $L_{[C\ II]}$ and L_{FIR} between

M8 and the Orion Bar is presented in Table 3.4. For M8, the $L_{\rm CO2-1} = 0.128\ L_{\odot}$ (calculated in a similar way as in Sect. 3.4.4), $L_{\rm [C\ II]}$ is calculated in Sect. 3.4.4 and $L_{\rm FIR} \sim 10^4\ L_{\odot}$ is obtained from White et al. (1998). The luminosities of the Orion Bar are taken from Goicoechea et al. (2015).

Table 3.4: CO $J = 2 \rightarrow 1$, [C II] and FIR luminosity ratios of M8 and the Orion Bar.

Luminosity ratio	M8	Orion Bar
$L_{\rm [C\ II]}/L_{\rm FIR}$	10^{-3}	1.1×10^{-3}
$L_{\rm [C\ II]}/L_{\rm CO2-1}$	7.5×10^{2}	1.6×10^{3}
$L_{\rm CO2-1}/L_{\rm FIR}$	1.3×10^{-6}	6.6×10^{-7}

We calculated the FUV radiation field, $G_0 \sim 0.6 - 1.12 \times 10^5$ in Habing units and density, $n \sim 0.97 - 1.93 \times 10^5$ cm^{-3} for the PDR of M8 by adopting an electron density $n_{\rm e}$ of 2000 – 4000 cm^{-3}, electron temperature $T_{\rm e}$ of 7000 – 9000 K (Woodward et al. 1986 and Esteban et al. 1999). We used the values of stellar luminosity and number of ionizing photons for an O7 star from Sect. 7.2.1 of Tielens (2010). The densities match well with the RADEX calculations carried out in Sect. 3.4.4. Interestingly, these calculated values of G_0 and n also match very well with those calculated for the Orion Bar. This leads us to a direct comparison of the results of the PDR models of the Orion Bar (Tielens & Hollenbach 1985, Jansen et al. 1995, Hogerheijde et al. 1995, Hollenbach & Tielens 1997, Hollenbach & Tielens 1999, and Andree-Labsch et al. 2017) with the PDR of M8 since we expect similar chemical and thermal conditions in both PDRs. Tielens & Hollenbach (1985) and Hollenbach & Tielens (1999) calculated the structure of the Orion Bar as a function of visual extinction $A_{\rm v}$. They show a typical case in which H_2 does not self-shield until dust attenuation of the FUV photons creates an atomic surface layer. According to this, in the PDR of M8 the transition of atomic H to molecular H_2 occurs at $A_{\rm v} = 2$, the carbon balance shifts from C^+ to C and CO at $A_{\rm v} = 4$, and except for the O in CO, all oxygen is in atomic form until very deep into the molecular cloud at $A_{\rm v} = 8$. The gas in the surface layer is much warmer at about $\sim$ 500 K than the dust, which is at about $\sim$ 30 – 75 K. Complementary to the H_2 column density calculation carried out in Sect. 3.4.1, assuming a dust temperature of 75 K and a maximum flux value of 5000 mJy/beam obtained from ATLASGAL data, allowed us to calculate the H_2 column density at Her 36, $N(H_2) \sim 3.75 \times 10^{22}$ cm^{-2} which is in reasonable agreement with that calculated in Sect. 3.4.1 within a factor $\sim$ 1.25.

Hogerheijde et al. (1995), Walmsley et al. (2000), and Andree-Labsch et al. (2017) described the geometry of the Orion Bar where the trapezium stars illuminate the PDR, which changes from a face-on to an edge-on orientation along the varying length of the line of sight. This geometry explains the [C I] peak that is symmetric around the peak of the CO emission (Tauber et al., 1994). The [C II] emission peak is also

distributed symmetrically around the ionization front (Stacey et al., 1993). Contrary to this, in M8, we see that [C II] peaks at the east of Her 36, [C I] peaks at Her 36, while the CO transitions peak in the northwest of Her 36, which supports the proposition of a face-on geometry.

3.5.3 Comparison with the PDR of M17 SW

M17, the Omega nebula is also among the best nearby laboratories to study star formation. It has an edge-on geometry in contrast to the face-on geometry of M8. It has a bright HII region ionized by the rich cluster NGC 6618 (Povich et al., 2009) and beyond this HII region lies the bright PDR in the southwest of M17 (M17 SW), which is responsible for the photoelectric heating of the warm gas (Pérez-Beaupuits et al., 2015). M17 SW also contains a wide ranged clumpy molecular cloud studied widely by Pérez-Beaupuits et al. (2010) and Pérez-Beaupuits et al. (2015).

In Sect. 3.3.2, the scatter plots related to M8 show only a weak correlation of [C II] with [C I] and ^{12}CO. The channel maps and line profiles at different offsets also show different morphologies of [C II] compared with those seen in [C I] and CO except in a small range of intermediate velocities toward Her 36. This suggests that [C II] and the molecular gas tracers on scales away from Her 36 do not originate from the same spatial region. This is similar to M17 SW as reported by Pérez-Beaupuits et al. (2015). In Sect. 3.4.3, the comparison between the observed ^{12}CO and ^{13}CO data with non-LTE RADEX modeling results show that the UC HII region or molecular gas near the Her 36 region has the highest density and kinetic temperature, while the molecular gas near the eastern HII region has low density and lower kinetic temperature. In contrast to M17 SW (Pérez-Beaupuits et al., 2015), the ^{12}CO SLED shapes we see in Fig. **??** toward Her 36 and mid-J CO positions follow a similar trend. Thus, they do not indicate large fluctuations in gas temperatures of the molecular gas. However, similarly to the case of M17 SW, the higher J CO lines show significantly lower intensities at the [C II] peak position. This is consistent with a PDR, where the [C II] peak emission is expected to arise from less dense gas than at the Her 36 position.

3.6 Conclusions

In this paper, we presented for the first time velocity integrated intensity maps of $J = 11 \rightarrow 10$, $J = 13 \rightarrow 12$, $J = 16 \rightarrow 15$ ^{12}CO and [C II] 158 μm, observed toward Her 36 in M8 using the dual-color Terahertz receiver GREAT on board the SOFIA telescope; $J = 2 \rightarrow 1$, $J = 3 \rightarrow 2$, $J = 6 \rightarrow 5$, and $J = 7 \rightarrow 6$ ^{12}CO transitions; $J = 2 \rightarrow 1$, $J = 4 \rightarrow 3$, and $J = 6 \rightarrow 5$ ^{13}CO transitions using the CHAMP$^+$, FLASH$^+$ and PI230 receivers of the APEX telescope; and $J = 1 \rightarrow 0$ transitions of ^{12}CO and ^{13}CO using the EMIR receiver of IRAM 30 m telescope.

Combining the information obtained from Sects. 3.3 and 3.5.1, we put forward the geometry of the region surrounding Her 36. M8 has a face-on geometry where the cold dense molecular cloud lies in the background with Her 36 being still very close to the dense core of the cloud from which it was born. Her 36 is powering the HII region toward the east of it along with 9 Sgr, while the foreground veil of a warm PDR is receding away (at lower velocities) from Her 36 toward the observer.

Using different techniques we studied the physical conditions in the molecular gas associated with M8. CO rotation diagrams indicate temperature gradients through the PDR. Low-J ^{13}CO transitions seem to originate from colder gas, while the $J = 8 \rightarrow 7$ transition seems to originate from the hottest gas. Quantitative analysis including LTE approximation methods and the non-LTE RADEX program were used to calculate the temperatures and H_2 number density in the PDR around Her 36. Kinetic temperatures ranging from 100 – 150 K and densities ranging from 10^4 – 10^6 cm^{-3} were obtained.

3.7 Acknowledgements

SOFIA is jointly operated by the Universities Space Research Association, Inc. (USRA), under NASA contract NAS2-97001, and the Deutsches SOFIA Institut (DSI) under DLR contract 50 OK 0901 and 50 OK 1301 to the University of Stuttgart. We are thankful to the SOFIA operations team for their help and support during and after the observations. M. Tiwari was supported for this research by the International Max-Planck-Research School (IMPRS) for Astronomy and Astrophysics at the Universities of Bonn and Cologne. We also thank Thushara Pillai for helpful discussions. The research reported here was motivated by a discussion between Don York and Karl Menten.

Chapter 4

Observational study of hydrocarbons in the bright photodissociation region of Messier 8

Abstract

Aims. Hydrocarbons are ubiquitous in the interstellar medium (ISM), but their formation is still not well understood, depending on the physical environment in which they are found. Messier 8 (M8) is host to one of the brightest [H II] regions and photodissociation regions (PDRs) in our galaxy. With the observed C_2H and c-C_3H_2 data toward M8, we aim at obtaining their densities and abundances and to shed some light on their formation mechanism.

Methods. Using the Atacama Pathfinder Experiment (APEX) 12 m, and the Institut de Radioastronomie Millimétrique (IRAM) 30 m telescopes, we performed a line survey toward Herschel 36 (Her 36), which is the main ionizing stellar system in M8, and an imaging survey within 1.3 × 1.3 pc around Her 36 of various transitions of C_2H and c-C_3H_2. We used both local thermodynamic equilibrium (LTE) and non-LTE methods to determine the physical conditions of the emitting gas along with the column densities and abundances of the observed species, which we compared with (updated) gas-phase photochemical PDR models. In order to examine the role of polycyclic aromatic hydrocarbons (PAHs) in the formation of small hydrocarbons and to investigate their association with the [H II] region, the PDR and the molecular cloud, we compared archival Galactic Legacy Infrared Mid-Plane Survey Extraordinaire (GLIMPSE) 8 μm and the Spectral and Photometric Imaging Receiver (SPIRE) 250 μm continuum images with the C_2H emission maps.

Results. We observed a total of three rotational transitions of C_2H with their hyperfine structure components and four rotational transitions of c-C_3H_2 with ortho and para symmetries toward the [H II] region and the PDR of M8. Fragmentation of PAHs seems less likely to contribute to the formation of small hydrocarbons as the 8 μm emission does not follow the distribution of C_2H emission, which is more associated with the molecular cloud toward the north west of Her 36. From the quantitative analysis, we obtained abundances of $\sim 10^{-8}$ and 10^{-9} for C_2H and c-C_3H_2 respectively, and volume densities of the hydrocarbon emitting gas in the range $n(H_2) \sim 5 \times 10^4$–$5 \times 10^6$ cm^{-3}.

Conclusions. The observed column densities of C_2H and c-C_3H_2 are reproduced reasonably well by our PDR models. This supports the idea that in high-UV flux PDRs,

gas-phase chemistry is sufficient to explain hydrocarbon abundances.

4.1 Introduction

Bright O and early B-type stars have strong ultraviolet (UV, hν > 13.6 eV) and far-ultraviolet (FUV, 6 eV < hν < 13.6 eV) fields that give rise to bright [H II] regions and photodissociation regions (PDRs). [H II] regions are comprised of hot ionized gas irradiated by strong UV radiations from nearby bright stars, while PDRs are at the interface of these [H II] regions and cold molecular clouds shielded from the illuminating star (Tielens & Hollenbach, 1985). In PDRs, the heating is regulated by FUV photons which give rise to a rich hydrocarbon chemistry (e.g., Pety et al. 2005). Several studies on small hydrocarbons such as C_2H and C_3H_2 have been done in diffuse clouds (Lucas & Liszt, 2000; Gerin et al., 2011), massive star-forming regions (Beuther et al., 2008), planetary nebulae (Schmidt & Ziurys, 2017), dark clouds (Pratap et al., 1997), and PDRs (Teyssier et al., 2004; Pety et al., 2005; Cuadrado et al., 2015; Nagy et al., 2015). These hydrocarbons play a key role in understanding the carbon chemistry taking place in both the gas phase and on grain surfaces. Several chemical pathways have been proposed for the formation of these hydrocarbons. It was found that in PDRs with low UV flux (G_0 < 100 in units of the Habing (1969) radiation field, where $G_0 = 1$ corresponds to a flux of 1.6×10^{-3} erg cm^{-2} s^{-1} for FUV photons) such as the Horsehead nebula, the observed abundances of hydrocarbons were found to be higher than those predicted by gas-phase chemical PDR models by an order of magnitude (Teyssier et al., 2004). This suggested that the current gas-phase chemistry does not adequately explain the observed high abundances of hydrocarbons, which led to the proposition that additional mechanisms may be responsible for their production. Le Page et al. (2003), Pety et al. (2005), and Montillaud et al. (2013) suggest that one such mechanism is the fragmentation of polycyclic aromatic hydrocarbons (PAHs) due to far-UV radiation. Meanwhile in PDRs with a high UV flux ($G_0 \sim 10^4$–10^5 in Habing units) such as the Orion bar, the observed hydrocarbon abundances can be roughly explained by gas-phase chemistry. The molecular gas gets heated to higher temperatures in high UV flux PDRs, facilitating new gas-phase formation routes, namely endothermic reactions and reactions with activation energy barriers (Cuadrado et al., 2015).

Messier 8 (M8) is among the highest UV flux ($G_0 \sim 10^5$ in Habing units) (Tiwari et al., 2018) PDRs in the Milky Way. It is located in the Sagittarius-Carina arm, near our line of sight toward the Galactic center. Its distance from the sun has been estimated as $\sim$ 1.3 kpc, a value we adopt (Damiani et al., 2004; Arias et al., 2006) (see the discussion in Tothill et al. 2008). The open young stellar cluster NGC6530, the [H II] region NGC6523/33, and large quantities of molecular gas are associated with M8 (Tothill et al., 2008). The brightest star in the open cluster NGC6530 is Herschel 36 (Her 36) at R.A. (α, J2000) = $18^h03^m40^s.3$ and Dec. (δ, J2000) = $-24°22'43''$ (Woolf, 1961), which has three main resolved components: a close massive binary

consisting of an O9 V and a B0.5 V star, and a more distant companion O7.5 star (Arias et al. 2010 and Sanchez-Bermudez et al. 2014).

An extensive survey of M8 at submillimeter, millimeter, and far-infrared wavelengths was reported in Tiwari et al. (2018), where we explored in detail the morphology of the area around Her 36 and determined the physical conditions governing this region. Observations were performed using several receivers of the Stratospheric Observatory for Infrared Astronomy (SOFIA, Young et al. 2012), the Atacama Pathfinder EXperiment (APEX 12 m, Güsten et al. 2006), and the Institut de Radioastronomie Millimétrique (IRAM) 30 m telescopes. M8 has a face-on geometry, where the cold dense molecular cloud lies in the background with Her 36 being still very close to the dense core of the cloud from which it originated. Her 36 is fueling the [H II] region toward the east of it along with 9 Sagitarii (9 Sgr) (another binary with an O3.5 V and an O5-5.5V stars, Rauw et al. 2012) and a foreground veil of warm PDR gas is receding away from Her 36 toward the observer (see the sketch in Fig. 15 of Tiwari et al. 2018). Using various CO transitions from $J = 1 \rightarrow 0$ to $16 \rightarrow 15$ at angular resolutions of $\sim 10''$ (minimum) for CO $J = 6 \rightarrow 5$ to $30''$ (maximum) for CO $J = 2 \rightarrow 1$ (Tiwari et al., 2018, Table 1), we determined the average kinetic temperatures in the region ranging from 100–150 K and the H_2 densities ranging from 10^4–10^6 cm^{-3}, with an H_2 column density of $N(H_2) \sim 3.8 \times 10^{22}$ cm^{-2}.

Several studies have addressed M8 in the X-ray, optical, and IR regimes (Stecklum et al. 1995; Damiani et al. 2004; Arias et al. 2006; Goto et al. 2006; Damiani et al. 2017). Interestingly, Dahlstrom et al. (2013) found anomalously broad diffuse interstellar bands (DIBs) at 5780.5, 5797.1, 6196.0, and 6613.6 along with CH^+ and CH in absorption along the line of sight to Her 36. A bright IR source, Her 36 SE (Goto et al., 2006), lying $0.25''$ south east of Her 36, is responsible for radiative excitation of CH^+ and CH. The broadening of DIBs has been attributed to radiative pumping of closely spaced high-J rotational levels of small polar molecules (Dahlstrom et al. 2013; Oka et al. 2014; York et al. 2014).

With the goal of constraining the physical conditions of the gas responsible for the emission of small hydrocarbons and verifying if gas-phase chemistry alone can explain the observed abundance of small hydrocarbons in M8, we here present an inventory of small hydrocarbons found toward M8 in a comprehensive survey including both observations toward the bright stellar system Her 36 and on-the-fly (OTF) maps in a region of $4' \times 4'$ (corresponding to 1.5×1.5 pc) around Her 36 at millimeter and submillimeter wavelengths. The organization of the paper is as follows. In Sect. 4.2, we summarize the observations done using the Principal Investigator (PI)230 and First Light APEX Submillimeter Heterodyne ($FLASH^+$) receivers of the APEX[1] 12 m

[1]This publication is based on data acquired with the Atacama Pathfinder EXperiment (APEX). APEX is a collaboration between the Max-Planck-Institut für Radioastronomie, the European Southern Observatory, and the Onsala Space Observatory.

Table 4.1: Observed hydrocarbons toward M8.

Species	Transition	Frequency (GHz)	E_{up}/k (K)	Instrument	Beam ($''$)	Critical density[a] (cm^{-3})
C_2H	$N = 1 \rightarrow 0,\ J = 3/2 \rightarrow 1/2,\ F = 1 \rightarrow 1$	87.2841	4.2	IRAM 30m/EMIR	30	2.5×10^5
	$N = 1 \rightarrow 0,\ J = 3/2 \rightarrow 1/2,\ F = 2 \rightarrow 1$	87.3168	4.2	IRAM 30m/EMIR	30	3.2×10^5
	$N = 1 \rightarrow 0,\ J = 3/2 \rightarrow 1/2,\ F = 1 \rightarrow 0$	87.3285	4.2	IRAM 30m/EMIR	30	9.5×10^4
	$N = 1 \rightarrow 0,\ J = 1/2 \rightarrow 1/2,\ F = 1 \rightarrow 1$	87.4019	4.2	IRAM 30m/EMIR	30	1.1×10^6
	$N = 1 \rightarrow 0,\ J = 1/2 \rightarrow 1/2,\ F = 0 \rightarrow 1$	87.4071	4.2	IRAM 30m/EMIR	30	1.8×10^5
	$N = 1 \rightarrow 0,\ J = 1/2 \rightarrow 1/2,\ F = 1 \rightarrow 0$	87.4464	4.2	IRAM 30m/EMIR	30	2.2×10^5
	$N = 3 \rightarrow 2,\ J = 7/2 \rightarrow 5/2,\ F = 3 \rightarrow 3$	261.9781	25.1	APEX/PI230	26	3.2×10^4
	$N = 3 \rightarrow 2,\ J = 7/2 \rightarrow 5/2,\ F = 4 \rightarrow 3$	262.0042	25.1	APEX/PI230	26	8.7×10^5
	$N = 3 \rightarrow 2,\ J = 7/2 \rightarrow 5/2,\ F = 3 \rightarrow 2$	262.0064	25.1	APEX/PI230	26	8.5×10^5
	$N = 3 \rightarrow 2,\ J = 5/2 \rightarrow 3/2,\ F = 3 \rightarrow 2$	262.0649	25.1	APEX/PI230	26	8.9×10^5
	$N = 3 \rightarrow 2,\ J = 5/2 \rightarrow 3/2,\ F = 2 \rightarrow 1$	262.0674	25.1	APEX/PI230	26	8.2×10^5
	$N = 3 \rightarrow 2,\ J = 5/2 \rightarrow 3/2,\ F = 2 \rightarrow 2$	262.0789	25.1	APEX/PI230	26	1.2×10^5
	$N = 3 \rightarrow 2,\ J = 5/2 \rightarrow 5/2,\ F = 3 \rightarrow 3$	262.2086	25.1	APEX/PI230	26	8.4×10^4
	$N = 3 \rightarrow 2,\ J = 5/2 \rightarrow 5/2,\ F = 2 \rightarrow 2$	262.2509	25.1	APEX/PI230	26	4.9×10^4
	$N = 5 \rightarrow 4,\ J = 11/2 \rightarrow 9/2,\ F = 6 \rightarrow 5$	436.661	62.9	APEX/FLASH$^+$ 460	13	2.9×10^6
	$N = 5 \rightarrow 4,\ J = 11/2 \rightarrow 9/2,\ F = 5 \rightarrow 4$	436.6618	62.9	APEX/FLASH$^+$ 460	13	2.9×10^6
	$N = 5 \rightarrow 4,\ J = 9/2 \rightarrow 7/2,\ F = 5 \rightarrow 4$	436.723	62.9	APEX/FLASH$^+$ 460	13	3.3×10^6
	$N = 5 \rightarrow 4,\ J = 9/2 \rightarrow 7/2,\ F = 4 \rightarrow 3$	436.724	62.9	APEX/FLASH$^+$ 460	13	3.2×10^6
c-C_3H_2 ortho	$J_{K_a,K_b} = 2_{1,2} \rightarrow 1_{0,2}$	85.3388	6.4	IRAM 30m/EMIR	30	1.1×10^6
	$J_{K_a,K_b} = 6_{3,4} \rightarrow 5_{2,3}$	285.7956	54.7	APEX/FLASH$^+$ 345	19	8.4×10^6
	$J_{K_a,K_b} = 7_{1,6} \rightarrow 6_{2,5}$	284.998	61.2	APEX/FLASH$^+$ 345	19	8.9×10^6
	$J_{K_a,K_b} = 8_{1,8} \rightarrow 7_{0,7}$	284.8052	64.3	APEX/FLASH$^+$ 345	19	1.0×10^7
c-C_3H_2 para	$J_{K_a,K_b} = 2_{0,2} \rightarrow 1_{1,1}$	82.0935	6.4	IRAM 30m/EMIR	30	9.9×10^5
	$J_{K_a,K_b} = 7_{2,6} \rightarrow 6_{1,5}$	284.9993	61.2	APEX/FLASH$^+$ 345	19	1.0×10^7
	$J_{K_a,K_b} = 8_{0,8} \rightarrow 7_{1,7}$	284.8052	64.3	APEX/FLASH$^+$ 345	19	1.0×10^7

[a] Critical densities are calculated using collision rates available at $T_{kin} = 100$ K for C_2H and at $T_{kin} = 120$ K for c-C_3H_2 from Spielfiedel et al. (2012) and Chandra & Kegel (2000) respectively.

telescope and the Eight MIxer Receiver (EMIR) of the IRAM[2] 30m telescope. In Sect. 4.3, we present the spectra and the velocity integrated maps of the observed transitions of C_2H and c-C_3H_2. The quantitative analysis of the data is described in Sect. 4.4. In Sect. 4.5, we discuss the results and the main conclusions of this work are summarized in Sect. 4.6.

4.2 Observations

4.2.1 APEX data

Observations of the $N = 3 \rightarrow 2$ and $5 \rightarrow 4$ transitions of C_2H and $J_{K_a,K_b} = 6_{3,4} \rightarrow 5_{2,3}$, $7_{1,6} \rightarrow 6_{2,5}$, and $8_{1,8} \rightarrow 7_{0,7}$ ortho and $7_{2,6} \rightarrow 6_{1,5}$ and $8_{0,8} \rightarrow 7_{1,7}$ para transitions of c-C_3H_2 were performed with the APEX 12 m submillimeter telescope during 2015 June–August (project id: M-095.F-0043-2015) and 2016 July and September (project ids: M-097.F-0030-2016 and M-098.F-0002-2016). As shown in Table 5.1, we used the following receivers: PI230 with a velocity resolution of 0.07 km s^{-1}, to map the $N = 3 \rightarrow 2$ of C_2H, which is split into eight hyperfine structure (hfs) components, FLASH$^+$ in the 460 GHz band with a velocity resolution of 0.05 km s^{-1}, to integrate deeply on the $N = 5 \rightarrow 4$ of C_2H, (four hfs components) toward Her

[2]Based on observations carried out with the IRAM 30 m telescope. IRAM is supported by INSU/CNRS, the MPG (Germany), and IGN (Spain)

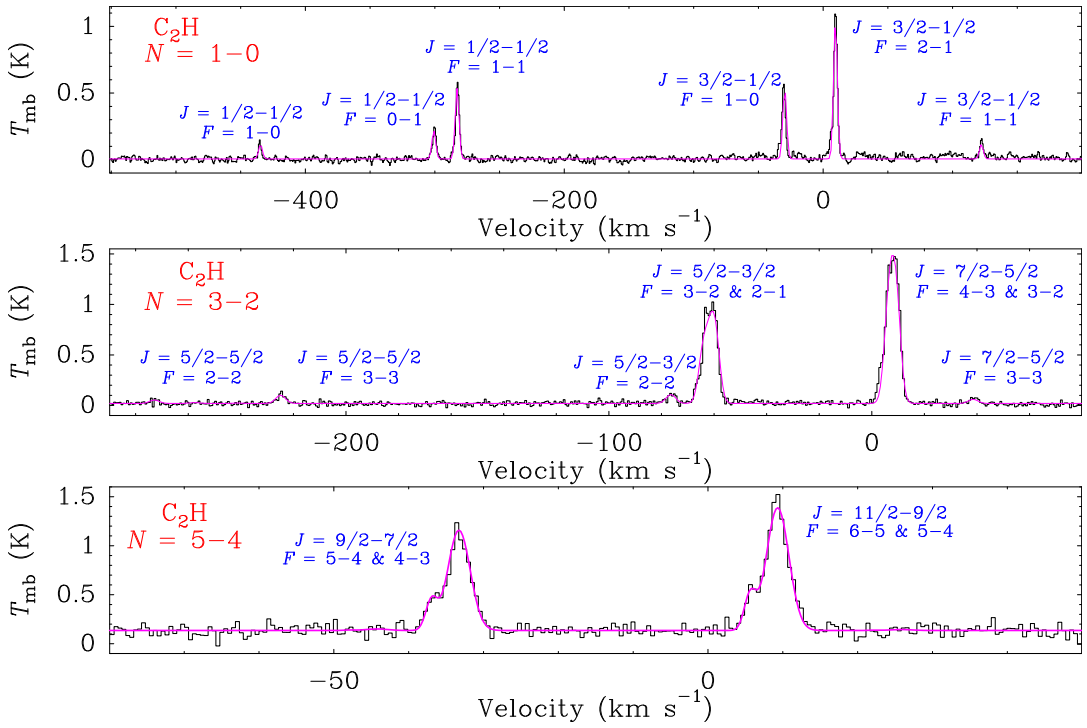

Figure 4.1: Observed hfs components of the N = 1 → 0, 3 → 2, 5 → 4 rotational transitions of C_2H toward Her 36 at R.A. $18^h03^m40^s.3$; Dec. $-24°22'43''$ (J2000). For the $N = 1 \rightarrow 0$ transition all six hfs are fully resolved, while for the $N = 3 \rightarrow 2$ and $5 \rightarrow 4$ transitions, some hfs lines overlap with each other. The $N = 5 \rightarrow 4$ shows an additional spectrally resolved velocity component (2–8 km s^{-1}) compared to other transitions. Only the detected lines are indicated by their quantum numbers J and F.

36, and FLASH$^+$ in the 345 GHz band with a velocity resolution of 0.04 km s^{-1}, to integrate deeply on the $J_{K_a,K_b} = 6_{3,4} \rightarrow 5_{2,3}$, $7_{1,6} \rightarrow 6_{2,5}$ and $8_{1,8} \rightarrow 7_{0,7}$ ortho; and $7_{2,6} \rightarrow 6_{1,5}$ and $8_{0,8} \rightarrow 7_{1,7}$ para transitions of c-C_3H_2 toward Her 36. To increase the signal-to-noise ratio, the data were later smoothed from a velocity resolution of 0.07 km s^{-1} to 0.7 km s^{-1}, 0.05 km s^{-1} to 0.5 km s^{-1}, and 0.04 km s^{-1} to 0.4 km s^{-1}.

The map was observed in OTF total power mode centered on R.A. = $18^h03^m40^s.3$ and Dec. = $-24°23'12''$(J2000), which corresponds to the position of Her 36. It has a size $\sim 240'' \times 240''$. Deep integrations were pointed at Her 36 for $\sim$ 3 minutes, while we integrated 0.7 s per dump for the map. An offset position relative to the center at (30′, –30′) was chosen for reference, similar to the previous observations done in Tiwari et al. (2018). The pointing accuracy ($< 3''$) was maintained by pointing checks on bright sources such as Mars and R Dor with the receivers tuned to CO lines every 1–1.5 hrs. A forward efficiency $\eta_f = 0.95$ was used for all receivers, and the beam coupling efficiencies $\eta_c = 0.62$, 0.69 and 0.56 were used for the PI230, FLASH$^+$340, and FLASH$^+$460 receivers, respectively.

4.2.2 IRAM 30 m data

Observations of the $N = 1 \rightarrow 0$ transition of C_2H and $J_{K_a,K_b} = 2_{1,2} \rightarrow 1_{0,2}$ ortho and $2_{0,2} \rightarrow 1_{1,1}$ transitions of c-C_3H_2 were performed with the IRAM 30 m telescope in August 2016 (project id: 017-16). Most of the 3 mm range was observed using the EMIR receivers (Carter et al., 2012) with a velocity resolution of 0.65 km s^{-1}. Six hfs structure lines of C_2H $N = 1 \rightarrow 0$ transition were mapped and deep integration pointed observations $J_{K_a,K_b} = 2_{1,2} \rightarrow 1_{0,1}$ ortho and $2_{0,2} \rightarrow 1_{1,1}$ para transitions of c-C_3H_2 were performed toward Her 36.

Similar to APEX observations, the map was observed in OTF total power mode centered on Her 36 and has a size of $240'' \times 240''$. Each sub scan lasted 25 s and the integration time on the off-source reference position was 5 s. The offset position relative to the center at (30′, -30′) was similar to that used for APEX observations and the pointing accuracy ($< 3''$) was maintained by pointing at the bright calibrator 1757-240 every 1−1.5 hrs. A forward efficiency $\eta_f = 0.95$ and the beam coupling efficiency $\eta_c = 0.69$ were adopted for EMIR receivers. These values were taken from the (2015) commissioning report[3].

All data reduction employed the Continuum and Line Analysis Single dish Software (CLASS) and GREnoble Graphic (GREG) softwares that are a part of the Grenoble Image and Line Data Analysis Software (GILDAS[4]) package and all observations are summarized in Table 5.1.

4.3 Results

4.3.1 Ethynyl: C_2H

The ethynyl radical (C_2H) was first detected in the interstellar medium (ISM) by Tucker et al. (1974). It is a linear molecule with spin rotation and hyperfine structure. The energy levels are designated as N, J, and F. The coupling between the rotational angular momentum N and the unpaired electron spin S causes spin doubling ($J = N + S$), while the coupling of angular momentum J and spin of the hydrogen nucleus I results in hfs ($F = J + I$) (Cuadrado et al., 2015). The electric dipole selection rules allow hfs splitting to occur only in specific quantum levels. We were able to identify a total of eighteen hfs components of C_2H and the line parameters derived from hfs fitting. The C_2H $N = 1 \rightarrow 0$ and $3 \rightarrow 2$ transitions have a single velocity component, while C_2H $N = 5 \rightarrow 4$ also have a spectrally resolved low velocity (2–8 km s^{-1}) component, in addition to a high velocity (8–15 km s^{-1}) component. This low velocity component is also seen in the CO, [C II] and [C I] spectra and corresponds to the warm foreground veil receding away from Her 36 toward the observer (Tiwari et al., 2018).

[3] www.iram.es/IRAMES/mainWIKI/IRAM30mEfficiencies
[4] www.iram.fr/IRAMFR/GILDAS/

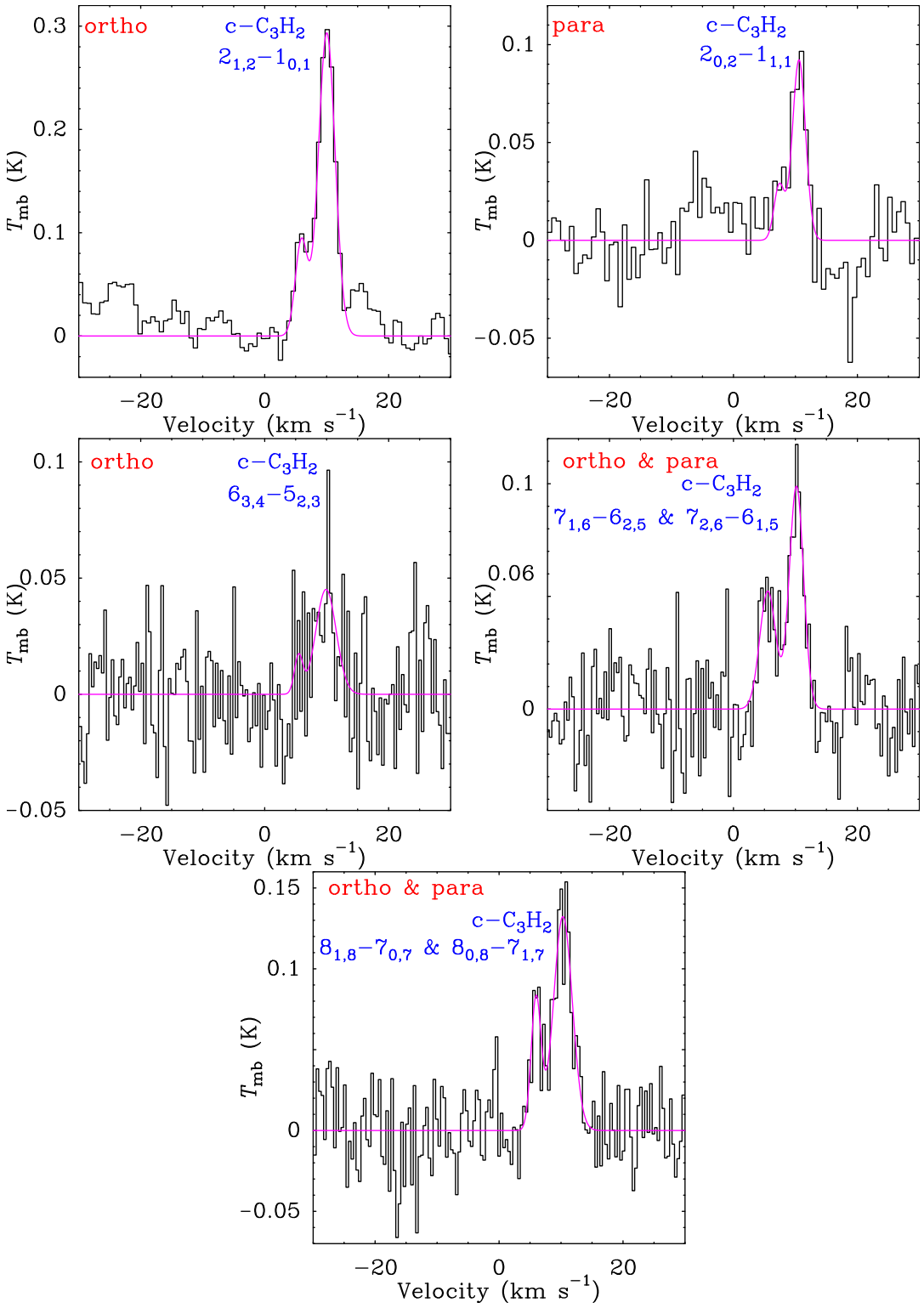

Figure 4.2: Observations of spectrally resolved $J_{\mathrm{K_a,K_b}} = 2_{1,2} \rightarrow 1_{0,1}$ and $6_{3,4} \rightarrow 5_{2,3}$ ortho and $J_{\mathrm{K_a,K_b}} = 2_{0,2} \rightarrow 1_{1,1}$ para transitions of c-C_3H_2 along with the spectrally blended $7_{1,6} \rightarrow 6_{2,5}$ and $8_{1,8} \rightarrow 7_{0,7}$ ortho and $7_{2,6} \rightarrow 6_{1,5}$ and $8_{0,8} \rightarrow 7_{1,7}$ para transitions toward Her 36 at R.A. $18^h03^m40^s.3$; Dec. $-24°22'43''$ (J2000).

The hfs fit parameters of the observed low and high velocity components of C_2H are given in Table 4.2.

The hfs line fitting results for all the transitions are shown in Fig. 4.1. The lowest energy rotational transition $N = 1 \rightarrow 0$ is split into six observable hfs levels that are well separated in frequency. The observed relative intensities are listed in Table B.1 and it can be seen that except for the lowest intensity lines, all match well with the expected relative intrinsic intensities as obtained from the Cologne Database for Molecular Spectroscopy[5] (CDMS). Hence, the lines are optically thin with no hfs emission anomalies and are consistent with an optical depth of $\tau \sim 0.1$. For the $N = 3 \rightarrow 2$ rotational transition, we identified eight hfs components. Among them, some hfs features are not completely resolved and hence, some lines overlap. The $J = 7/2 \rightarrow 5/2$, $F = 4 \rightarrow 3$, and $F = 3 \rightarrow 2$ overlap; and the $J = 5/2 \rightarrow 3/2$, $F = 3 \rightarrow 2$, and $F = 2 \rightarrow 1$ overlap. The observed relative line intensities turn out to be different from the expected relative intensities except for the higher transitions as shown in Table B.1. This suggests optical depth effects and indeed an optical depth of $\tau \sim 1.74$ was calculated. For the $N = 5 \rightarrow 4$ rotational transition, we identified four hfs components where the lines with $J = 9/2 \rightarrow 7/2$, $F = 5 \rightarrow 4$, and $F = 4 \rightarrow 3$ and the lines with $J = 11/2 \rightarrow 9/2$, $F = 6 \rightarrow 5$, and $F = 5 \rightarrow 4$ overlap. The observed relative intensities match well with the expected relative intrinsic intensities and are consistent within optical depth $\tau \sim 0.1$.

Table 4.2: Hfs fit parameters of the observed low and high velocity components of C_2H.

Transition	v^a(km s^{-1})	$\Delta\ v^a$(km s^{-1})	$T_{mb}{}^a$(K)	τ^a
Low velocity component				
$N = 5 \rightarrow 4$	5.9 (0.524)	1.63 (1.74)	0.9 (0.053)	0.78 (0.1)
High velocity component				
$N = 1 \rightarrow 0$	9.5 (0.0025)	3.43 (0.014)	2.5 (0.018)	$\sim 0.1^b$
$N = 3 \rightarrow 2$	8.8 (0.013)	4.52 (0.046)	4.5 (0.031)	1.74 (0.102)
$N = 5 \rightarrow 4$	9.6 (0.524)	3.45 (1.74)	2.6 (0.053)	$\sim 0.1^b$

[a] The values in the parentheses indicate the errors from the fit.
[b] The lower limit value of τ is 0.1 calculated by GILDAS for optically thin emission.

4.3.2 Cyclopropenylidene: c-C_3H_2

Cyclopropenylidene, c-C_3H_2, was first discovered in the ISM by Matthews & Irvine (1985) and Thaddeus et al. (1985). It is a three-membered carbon ring with C_{2v} symmetry (see Spezzano et al. 2012, Fig. 1), with a large dipole moment of 3.4

[5] http://www.astro.uni-koeln.de/cdms/

Debye making it highly polar. It has ortho and para symmetries owing to the two out of plane hydrogen atoms, which are equidistant from the C atoms. It is an oblate asymmetric top with b-type rotational transitions where the main selection rules are ΔK_a and $\Delta K_c = \pm 1$. The levels are ortho and para depending on the odd and even values of $K_a + K_c$ (for a more extensive description see Cuadrado et al. 2015).

We observed two completely resolved ortho transitions $J_{K_a,K_b} = 2_{1,2} \rightarrow 1_{0,1}$ and $6_{3,4} \rightarrow 5_{2,3}$, and one para transition $J_{K_a,K_b} = 2_{0,2} \rightarrow 1_{1,1}$. In addition, we observed $J_{K_a,K_b} = 7_{1,6} \rightarrow 6_{2,5}$ and $8_{1,8} \rightarrow 7_{0,7}$ ortho, and $7_{2,6} \rightarrow 6_{1,5}$ and $8_{0,8} \rightarrow 7_{1,7}$ para transitions where ortho and para lines are blended. Similar to the $N = 5 \rightarrow 4$ transition of C_2H, all observed transitions of c-C_3H_2 have a spectrally resolved low velocity component (centered at ~ 6 km s^{-1}) as can be seen in Fig. 4.2. The line parameters are derived from a two-component gaussian fit to the observed spectra as mentioned in Table 4.3.

Table 4.3: c-C_3H_2 line parameters as calculated from two-component gaussian fit using GILDAS.

Transition	Symmetry	v^a(km s^{-1})	$\Delta\ v^a$(km s^{-1})	$T_{peak}{}^a$(mK)
Low velocity component				
$2_{1,2} \rightarrow 1_{0,1}$	ortho	6.0 (0.22)	2.3 (0.43)	90 (18)
$2_{0,2} \rightarrow 1_{1,1}$	para	7.2 (0.62)	2.0 (0)	40 (17)
$6_{3,4} \rightarrow 5_{2,3}$	ortho	6.3 (1.0)	2.7 (1.3)	20 (23)
$7_{1,6} \rightarrow 6_{2,5}$	ortho	5.5 (0.3)	3.1 (0.7)	50 (13)
$7_{2,6} \rightarrow 6_{1,5}$	para	5.5 (0.3)	3.1 (0.7)	50 (13)
$8_{1,8} \rightarrow 7_{0,7}$	ortho	6.0 (0.2)	1.9 (0.5)	80 (20)
$8_{0,8} \rightarrow 7_{1,7}$	para	6.0 (0.2)	1.9 (0.5)	80 (20)
High velocity component				
$2_{1,2} \rightarrow 1_{0,1}$	ortho	10 (0.07)	3.17 (0.2)	300 (18)
$2_{0,2} \rightarrow 1_{1,1}$	para	10.5 (0.2)	2.6 (0.4)	100 (17)
$6_{3,4} \rightarrow 5_{2,3}$	ortho	10.1 (0.3)	3.3 (1.2)	50 (23)
$7_{1,6} \rightarrow 6_{2,5}$	ortho	10.2 (0.15)	2.7 (0.4)	100 (13)
$7_{2,6} \rightarrow 6_{1,5}$	para	10.2 (0.15)	2.7 (0.4)	100 (13)
$8_{1,8} \rightarrow 7_{0,7}$	ortho	10.3 (0.15)	3.6 (0.4)	130 (20)
$8_{0,8} \rightarrow 7_{1,7}$	para	10.3 (0.15)	3.6 (0.4)	130 (20)

[a] The values in the parentheses indicate the errors from the fit.

4.3.3 Spatial distribution of C_2H and comparison with ancillary data

Figure 4.3 shows velocity integrated intensity maps of the brightest transitions of C_2H $N = 1 \rightarrow 0$, $J = 3/2 \rightarrow 1/2$, $F = 2 \rightarrow 1$ at 87.316 GHz with an rms noise of 0.3 K km s^{-1}, and $N = 3 \rightarrow 2$ $J = 7/2 \rightarrow 5/2$, $F = 4 \rightarrow 3$ at 262.004 GHz with an rms noise of 0.44 K km s^{-1}. The $N = 1 \rightarrow 0$ transition is bright toward the north

west of Her 36 and peaks (in projection) deep into the molecular cloud at ($\Delta\alpha$ = –56″, $\Delta\delta$ = 28″). This position is very close to the secondary APEX Telescope Large Area Survey of the Galaxy (ATLASGAL) 870 μm dust continuum peak toward this region at ($\Delta\alpha$ = –53″, $\Delta\delta$ = 23″) (Tiwari et al., 2018, Fig. 7 (a)), which is probing the cold molecular cloud. The $N = 3 \rightarrow 2$ transition is brightest close to Her 36 at ($\Delta\alpha$ = 0″, $\Delta\delta$ = 12″) with the emission extending toward the north west of Her 36. The hot gas near Her 36 would be able to excite C_2H molecules to rotational levels with higher upper level energies whereas the gas deep in the molecular cloud would be comparatively cooler. It is noteworthy that the extended emission, as shown in Fig. B.1, toward the north west of Her 36 is also seen in low and mid-J CO transitions and in [C I] observed toward M8 by the APEX and IRAM 30 m telescopes (Tiwari et al., 2018).

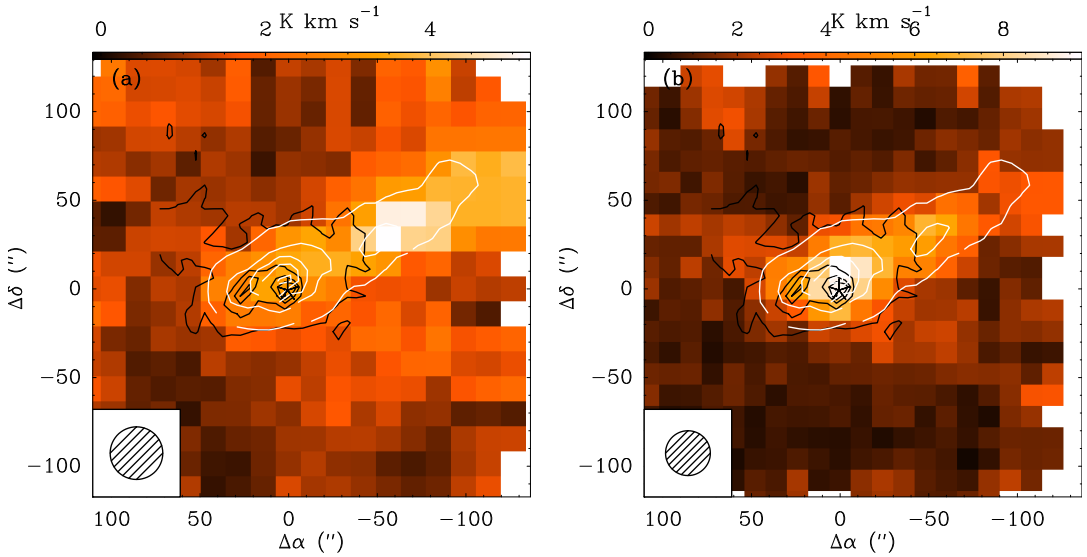

Figure 4.3: Color maps of the velocity integrated intensity of the: (a, upper panel) $N = 1 \rightarrow 0$ and (b, lower panel) $3 \rightarrow 2$ transitions of C_2H toward Her 36, which is the central position ($\Delta\alpha$ = 0, $\Delta\delta$ = 0) at R.A.(J2000) = $18^h03^m40.3^s$ and Dec.(J2000) = –24°22′43″, marked with an asterisk. Both maps are plotted using original beam sizes shown in the bottom left of each map. These maps are overlaid with contours of GLIMPSE 8 μm continuum emission in black, with a beam size of 0.6″ and with contours of SPIRE 250 μm continuum emission in white, with a beam size of 17.9″. For GLIMPSE 8 μm continuum emission, the contour levels are 10% to 100% in steps of 20% of the peak emission and for SPIRE 250 μm continuum emission, the contour levels are 10% to 100% in steps of 10% of the peak emission.

In order to investigate the relation of the dense and cold molecular cloud material to the hot ionized gas in M8, we compared our observed C_2H data with observations obtained from two surveys conducted at different wavelengths. Firstly, we used the 8 μm data from the Galactic Legacy Infrared Mid-Plane Survey Extraordinaire (GLIMPSE, Benjamin et al. 2003) archive observed with Spitzer Space Telescope.

The 8 μm band of the Infrared Array Camera (IRAC) used by Spitzer covers emission from PAHs which are small molecules excited by strong UV radiation. Since the IR emission from these large molecules (or small dust grains) constitutes fluorescence that results from far-UV pumping, it emerges from the surface layers of dense molecular clouds, hence PAH emission probes recent high-mass star formation (Tielens, 2008). Figure 4.3 shows the velocity integrated intensity maps of C_2H $1 \rightarrow 0$ and $3 \rightarrow 2$ transitions in color scale overlaid with GLIMPSE 8 μm contours in black, which peak at Her 36 ($\Delta\alpha = 0''$, $\Delta\delta = 0''$) and at the [C II] emission peak ($\Delta\alpha = 30''$, $\Delta\delta = -2''$). The [C II] data was observed in May 2016 by the SOFIA telescope and have been reported in Tiwari et al. (2018). Secondly, we obtained, from the Herschel Space Archive[6] (HSA), data collected with the Spectral and Photometric Imaging Receiver (SPIRE, Griffin et al. 2010) aboard the Herschel Space Observatory (Pilbratt et al., 2010). The SPIRE data trace interstellar dust. The white contours in Fig. 4.3 represent the SPIRE 250 μm continuum emission, which peaks at Her 36 ($\Delta\alpha = 0''$, $\Delta\delta = 0''$) and is extended in the north west direction with a secondary peak coinciding with the peak of the C_2H $1 \rightarrow 0$ emission ($\Delta\alpha = -56''$, $\Delta\delta = 28''$).

4.4 Analysis

Various transitions of C_2H and c-C_3H_2 observed with the IRAM 30 m and APEX 12 m telescopes allow us to carry out a detailed analysis to determine the temperature and density of the gas responsible for the emission of hydrocarbons in M8 with several complementary methods. We started with estimating the excitation temperature and the total C_2H column density by using its OTF maps of $1 \rightarrow 0$ and $3 \rightarrow 2$ transitions in Sect. 4.4.1. We then calculated column densities and abundances of both C_2H and c-C_3H_2 from rotational diagrams in Sect. 4.4.2. To complete the analysis, we made use of a radiative transfer model to constrain the H_2 densities in M8 in Sect. 4.4.3 and compared our observed results with PDR models in Sect. 4.4.4.

4.4.1 Excitation temperature and column density estimates of C_2H

Assuming a beam filling factor of unity and optically thin emission in both the C_2H, $N = 1 \rightarrow 0$, $J = 3/2 \rightarrow 1/2$, $F = 2 \rightarrow 1$ at 87.316 GHz and $N = 3 \rightarrow 2$ $J = 7/2 \rightarrow 5/2$, $F = 4 \rightarrow 3$ at 262.004 GHz transitions, the excitation temperature can be estimated by

$$T_{\rm ex} = \frac{-20.95}{ln\left(0.144\frac{W_3}{W_1}\right)}\mathrm{K}\,, \tag{4.1}$$

[6] https://irsa.ipac.caltech.edu/applications/Herschel/

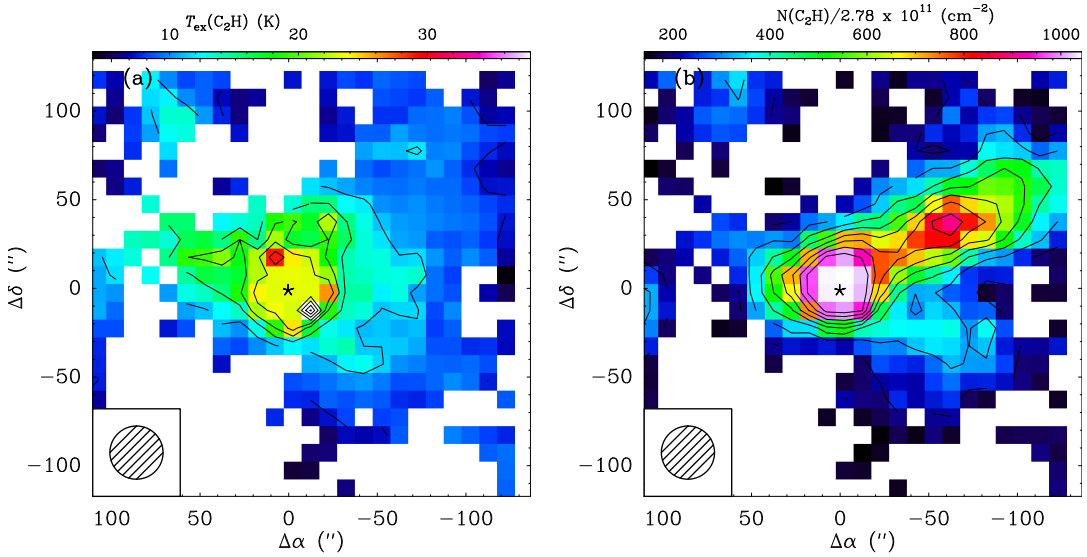

Figure 4.4: (a, upper panel) shows the excitation temperature defining the populations of $N = 1$ and 3 levels and (b, lower panel) shows the total column density of C_2H. The asterisk represents Her 36, which is the central position ($\Delta\alpha = 0$, $\Delta\delta = 0$) at R.A.(J2000) = $18^h03^m40.3^s$ and Dec.(J2000) = –24°22′43″. The contour levels are 10% to 100% in steps of 10% of the corresponding peak emissions. The values of main beam brightness temperatures and that of the velocity integrated intensities for the $N = 1$ and 3 levels used to calculate the $T_{ex}(C_2H)$ and $N(C_2H)$ were extracted from maps convolved to the same resolution of 30″.

where W_1 and W_3 are the velocity integrated intensities in K cm s^{-1} of $N = 1 \rightarrow 0$ and $3 \rightarrow 2$ transitions of C_2H respectively. The resulting T_{ex} distribution is shown in Fig. 5.3 a, and these are only lower limits to the excitation temperature as the beam filling factor is assumed to be unity. The peak of the T_{ex} distribution $\sim$ 38 K $\pm$ 11 K lies in the immediate south west of Her 36 ($\Delta\alpha$ = -15″, $\Delta\delta$ = -13″delta) and T_{ex} decreases with the distance from the star.

Assuming the environment to be in local thermodynamical equilibrium (LTE) such that all transitions have the same excitation temperature and that T_{ex} equals the molecule's rotation temperature, T_{rot}, we calculated the total column density of C_2H using the computed T_{ex} and the velocity integrated intensity, W_3, of $N = 3 \rightarrow 2$ transition of C_2H:

$$N(C_2H) = 2.78 \times 10^{11}(1.9\ T_{ex} + 1.38)\ \exp\left(\frac{25.15}{T_{ex}}\right)\ W_3\ \mathrm{cm}^{-2}\,. \qquad (4.2)$$

Figure 5.3 b shows the resulting C_2H total column density distribution with a peak value of $N(C_2H) \sim (3 \pm 0.26) \times 10^{14}$ cm^{-2} at Her 36 and a secondary peak toward

the north west of Her 36 in the molecular cloud similar to the secondary ATLASGAL peak. This results in an abundance of $N(C_2H)/N(H_2) \sim 8 \times 10^{-8}$, where we adopted $N(H_2) \sim 3.75 \times 10^{22}$ cm^{-2} (Tiwari et al., 2018).

4.4.2 Rotational diagrams of C_2H and c-C_3H_2

In Sect. 4.4.1, we presented the maps of excitation temperature and total column density distribution of C_2H in M8, around Her 36. However, c-C_3H_2 and the higher transition of C_2H were a part of point observations done by integrating deeply toward Her 36. So, we exploit the technique of rotational diagrams to perform a detailed analysis of more transitions as compared to Sect. 4.4.1. Also, here we plot rotational diagrams for both low and high velocity components of all observed transitions of C_2H and c-C_3H_2 observed toward Her 36. Assuming LTE, rotational diagrams ("Boltzmann plots") can be used to estimate the total column densities, $N_{\rm tot}$, of C_2H and c-C_3H_2 and the rotation temperatures, $T_{\rm rot}$, describing their level populations (Goldsmith & Langer, 1999). In a rotational diagram, $ln(N_{\rm u}/g_{\rm u})$ is plotted versus $E_{\rm up}/k$. Here, $ln(N_{\rm u})$ and $g_{\rm u}$ ($\equiv 2J+1$) are the column density in and the degeneracy of the upper energy level, respectively, $E_{\rm up}$ is the upper level energy, and k is the Boltzmann constant.

Given the extended emission seen in the velocity integrated intensity maps in Fig. 4.3, we adopted a beam filling factor of one to make rotational diagrams. Moreover, we assume the hfs lines of each rotational transition to be treated as a single component with a quantum number N. We then calculated the total velocity integrated intensity, the upper level degeneracy $g_{\rm u}$ and the line strength of different transitions as the sum of all the observed hfs components of each $N + 1 \rightarrow N$ transition. Using the weighted average with the relative strength of each line as weight, the hfs-weighted frequency ν was obtained (as in Cuadrado et al. 2015) and the Einstein coefficient A was calculated using Goldsmith & Langer (1999, Eq. 25).

Figures 4.5 a and b show rotational diagrams of C_2H for low (2–8 km s^{-1}) and high (8–15 km s^{-1}) velocity components, respectively. Firstly, under the assumption that the C_2H lines are optically thin, that is, that the optical depth correction term C_τ is unity in Goldsmith & Langer (1999, Eq. 24), we plotted $N_{\rm u}^{\rm thin}/g_{\rm u}$ versus $E_{\rm up}/k$ in red for three transitions toward Her 36. Since the low velocity component could only be spectrally resolved for the $N = 5 \rightarrow 4$ transition, we estimated the low velocity component's line parameters for the other transitions assuming the same velocity and line width as that of $N = 5 \rightarrow 4$. Subsequently, we plotted the corrected diagrams, in blue, by including the optical depth correction values according to Goldsmith & Langer (1999, Eq. 24). The optical depth values were obtained from the hfs fit and are listed in Table 4.2.

Figures 4.5 c, d, e and f show rotational diagrams of the ortho and para species of

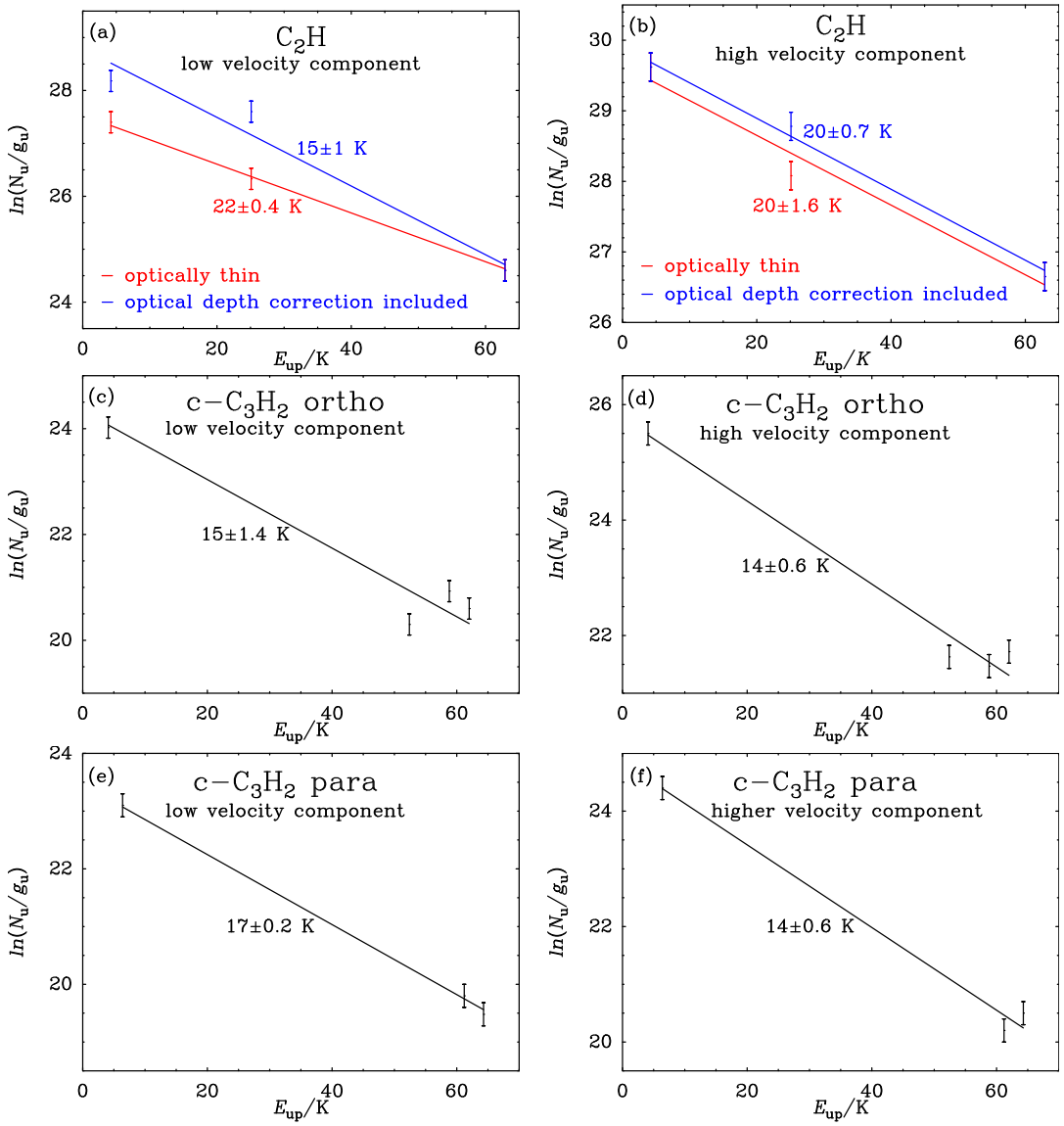

Figure 4.5: Rotational diagrams of various transitions of the $N = 1 \rightarrow 0$, $3 \rightarrow 2$, and $5 \rightarrow 4$ transitions of C_2H (top row); $J = 2 \rightarrow 1$, $6 \rightarrow 5$, $7 \rightarrow 6$, and $8 \rightarrow 7$ transitions of ortho c-C_3H_2 (top and bottom rows); and $J = 2 \rightarrow 1$, $7 \rightarrow 6$, and $8 \rightarrow 7$ transitions of para c-C_3H_2 (bottom row) observed toward Her 36. For C_2H, rotational diagrams are plotted with an assumption of optically thin C_2H (in red) and including the optical depth correction factors (in blue). Fitted values of rotational temperatures are given for each molecule. The error bars were calculated from the maximum noise of the integrated intensities of individual transitions and from calibration uncertainties of 20%.

c-C_3H_2 for the low (2–8 km s^{-1}) and high (8–15 km s^{-1}) velocity components. We first assumed c-C_3H_2 to be optically thin and from $J_{K_a,K_b} = 2_{1,2} \rightarrow 1_{0,1}$ ortho and $J_{K_a,K_b} = 2_{0,2} \rightarrow 1_{1,1}$ para transitions, we calculated the ortho/para ratio: ~ 2.2 for the low velocity component and 3.3 for the high velocity component. These ratios were used to estimate the contributions from ortho and para species to the $J_{K_a,K_b} = 7_{1,6} \rightarrow 6_{2,5}$ and $8_{1,8} \rightarrow 7_{0,7}$ ortho, and $7_{2,6} \rightarrow 6_{1,5}$ and $8_{0,8} \rightarrow 7_{1,7}$ para transitions, where the lines from the two species are blended together as can be seen in Fig. 4.2. From the obtained rotational temperatures, we estimated the column densities of C_2H and c-C_3H_2, which in turn were used to determine the optical depths of c-C_3H_2 (Goldsmith & Langer, 1999, Eq. 27). The estimated optical depth values came out to be very low, validating our assumption of optically thin c-C_3H_2.

The calculated rotational temperatures T_{rot} and column densities $N(X)$ along with their abundances $N(X)/N(H_2)$ of C_2H and c-C_3H_2 are given in Table 4.4. The total column density value of C_2H at the Her 36 position calculated using the rotational diagrams is very similar to that determined in Sect. 4.4.1.

Table 4.4: Physical parameters calculated from rotational diagrams.

Species	Lower velocity component		Higher velocity component		Abundance
	T_{rot} (K)	$N(X)$ (cm^{-2})	T_{rot} (K)	$N(X)$ (cm^{-2})	$N(X)/N(H_2)$
C_2H(optically thin)	22 ± 0.4	(3.8 ± 0.2) × 10^{13}	20 ± 1.6	(2.9 ± 0.1) × 10^{14}	(0.9 ± 0.04) × 10^{-8}
C_2H(optical depth correction included)	15 ± 1	(9.8 ± 0.5) × 10^{13}	20 ± 0.7	(3.8 ± 0.3) × 10^{14}	(1.3 ± 0.1) × 10^{-8}
c-C_3H_2 - ortho	15 ± 1.4	(4 ± 0.1) × 10^{12}	14 ± 0.6	(1.8 ± 0.43) × 10^{13}	(6 ± 1.2) × 10^{-10}
c-C_3H_2 - para	17 ± 0.2	(2.2 ± 0.1) × 10^{12}	14 ± 0.6	(7.2 ± 0.2) × 10^{12}	(2.5 ± 0.1) × 10^{-10}

4.4.3 Non-LTE calculations

In Sects. 4.4.1 and 4.4.2, we obtained the column densities and abundances of C_2H, o-C_3H_2 and p-C_3H_2 under the assumption of LTE. The derived rotational temperatures ($\sim$ 15–20 K) are much lower than the values that one might expect in the vicinity of Her 36 and temperatures derived in our previous study (Tiwari et al., 2018). This could be caused by the fact that the critical densities of the higher E_{up} lines of C_2H and c-C_3H_2 are much higher than those of the lower E_{up} lines of both molecules. This leads to subthermal excitation of the higher E_{up} lines and, consequently, to lower than LTE integrated intensities (and lower N_{up}/g_{up} values). This results in a steepening of the fitted line whose slope gives T_{rot} and an underestimation of that quantity. Therefore the resultant rotation temperature and column densities should only be considered as guiding values. To address this issue, we employ a non-LTE analysis that delivers kinetic temperature and H_2 volume densities of the gas that gives rise to the emission of C_2H and C_3H_2. RADEX is a non-LTE radiative transfer program (van der Tak et al., 2007), which uses the escape probability approximation for a homogeneous medium and takes into account optical depth effects. We chose a uniform sphere geometry. The collision rates used in the modeling are provided

by the Leiden Molecular and Atomic Database[7] (LAMDA; Schöier et al. 2005). The C_2H-H_2 collision rates are calculated by multiplying a factor of 1.36 to the C_2H-He collision rates given by Spielfiedel et al. (2012), while the C_3H_2-H_2 collision rates are given by Chandra & Kegel (2000). We computed grids in kinetic temperatures in the range 20–250 K and H_2 volume densities in the range 10^3–10^8 cm^{-3} and a background temperature of 2.73 K as input parameters, and then calculated brightness temperature ratios of different transitions of C_2H, o-C_3H_2 and p-C_3H_2.

We adopted the line widths from the average spectra of our data of C_2H, o-C_3H_2 and p-C_3H_2: 3, 2.5 and 2.2 km s^{-1}, respectively for the low velocity (2–8 km s^{-1}) component and 3.6, 3.3 and 3 km s^{-1}, respectively for the high velocity (8–15 km s^{-1}) component. For modeling, we used the C_2H, o-C_3H_2, and p-C_3H_2 column densities as estimated from the rotational diagrams in Sect. 4.4.2: 7×10^{13}, 7×10^{12}, and 4×10^{12} cm^{-2}, respectively for the low velocity component and 4×10^{14}, 2×10^{13}, and 7×10^{12} cm^{-2}, respectively for the high velocity component. Figure 4.6 shows the brightness temperature ratios (in different colors) of various transitions of C_2H, o-C_3H_2, and p-C_3H_2 on a $\log_{10}(n(H_2))$ versus T_{kin} plot. The two different contours per color represent the RADEX modeling output values equal to the upper and lower bounds of the value obtained for each ratio from the observations with an error of 20%. For low T_{kin} (20–100 K), a gradient in density is seen, which then almost saturates for higher T_{kin} (100–250 K).

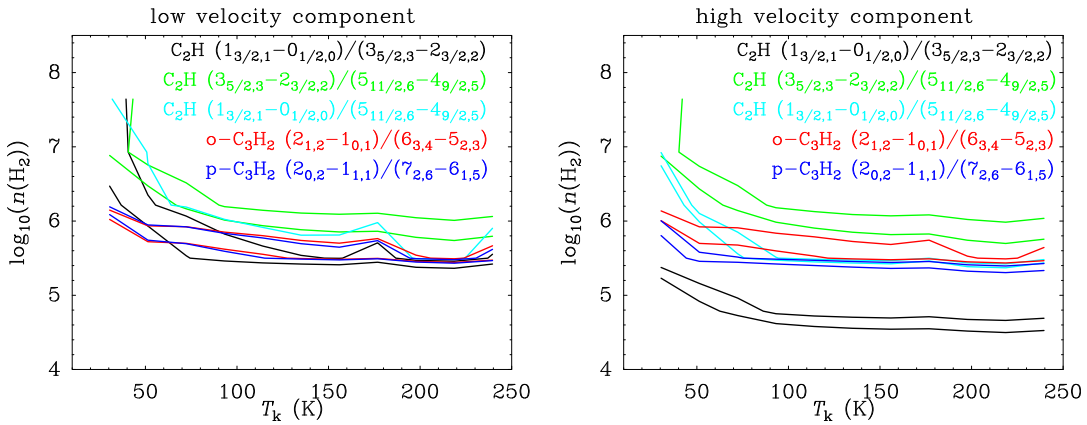

Figure 4.6: Results obtained from RADEX modeling for the main beam brightness temperature ratios of various transitions of C_2H and c-C_3H_2 toward Her 36 in a $\log_{10}(n(H_2))$ versus T_k grid. The left and right panels correspond to the low velocity and the high velocity components, respectively. The two contours per color represent the RADEX modeling output values equal to the upper and lower bounds of the value obtained for each ratio from the observations with an error of 20%.

For very low temperatures, $T_{kin} < 50$ K, the H_2 volume density $n(H_2)$ is as high as up

[7] http://www.strw.leidenuniv.nl/moldata/

to 5×10^7 cm^{-3}. However, in our previous work we determined kinetic temperatures $T_{\rm kin} \sim$ 100–150 K in M8 (Tiwari et al., 2018, Sect. 4.3), which puts a constraint on the volume density $n(H_2)$ values. For the low velocity component shown in Fig. 4.6 left panel, all hydrocarbons probe similar gas that is a part of the foreground veil, which has been found by and discussed in Tiwari et al. (Sect. 5.1 2018, Fig. 15). The foreground veil is being accelerated toward us by the strong radiation and wind of Her 36, which is a part of the cold dense molecular cloud, has H_2 volume density $n(H_2)$ in a range of 5×10^5–5×10^6 cm^{-3}. For the high velocity component shown in Fig. 4.6 b, the different ratios of C_2H probe gas of different densities. For $T_{\rm kin} \sim$ 100–150 K, C_2H $(1 \rightarrow 0)/(5 \rightarrow 4)$ probe the same gas as o-C_3H_2 and p-C_3H_2 with $n(H_2) \sim 1 \times 10^6$ cm^{-3}, while C_2H $(3 \rightarrow 2)/(5 \rightarrow 4)$ probe slightly denser gas with $n(H_2) \sim 5 \times 10^6$ cm^{-1} and C_2H $(1 \rightarrow 0)/(3 \rightarrow 2)$ probe lower density gas with $n(H_2) \sim 5 \times 10^4$ cm^{-3}. This velocity component with an H_2 volume density $n(H_2)$ in the range of 5×10^4–5×10^6 cm^{-3}, consists of the gas very close to Her 36 and also the background material toward the north east of it (Tiwari et al., 2018, Sect. 5.1).

4.4.4 Comparison with PDR models

In order to compare the results obtained with the LTE and non-LTE models, we use PDR models to estimate the relative abundances of the C_2H and c-C_3H_2 species. These PDR models are based on Meijerink & Spaans (2005), which include more than 300 species in the chemical network, photo-electric heating from PAHs and small dust grains, cosmic-ray heating, and other classical heating and cooling mechanism for the thermal and chemical balance. A semi-infinite slab geometry and irradiation from one side without geometrical dilution are assumed. The PDR models do not distinguish between ortho and para molecules, but they provide the total abundance of c-C_3H_2 (and all other available species) self-consistently depending on the depth and visual extinction of the parallel slab. The model uses total gas density, $n_{\rm H} = n({\rm H}) + 2n(H_2)$, as an input parameter and the actual density of the collisional partner, molecular hydrogen $n(H_2)$, is calculated self-consistently along with the densities of other species from chemical and thermal balance equations, and is depth dependent.

We model four scenarios with two different total gas densities, $n_{\rm H}$, and two levels of strength of the impinging radiation field, G_0, in Habing units. In the models we assume solar metallicity and the visual extinction is estimated using the up-to-date relation $N({\rm H}) = 2.21 \times 10^{21}$ cm$^{-2} \times A_{\rm V}$ found by Güver & Özel (2009).

For G_0, we used the values 0.6×10^5 and 1.12×10^5 estimated in our previous paper (Tiwari et al., 2018, Sect. 5.2), using Tielens (2010, Eq. 9.2) for an O star with electron density, $n_{\rm e}$, of 2000–4000 cm^{-3} and electron temperature, $T_{\rm e}$, of 7000–9000 K (Woodward et al., 1986; Esteban et al., 1999). We need to use quite high total gas densities, $n_{\rm H}$, of 10^6 and 10^7 cm^{-3} in order to reach densities of the collision partner $n(H_2)$ similar to the values found in Sect. 4.4.3 using RADEX. Figure 4.7 shows

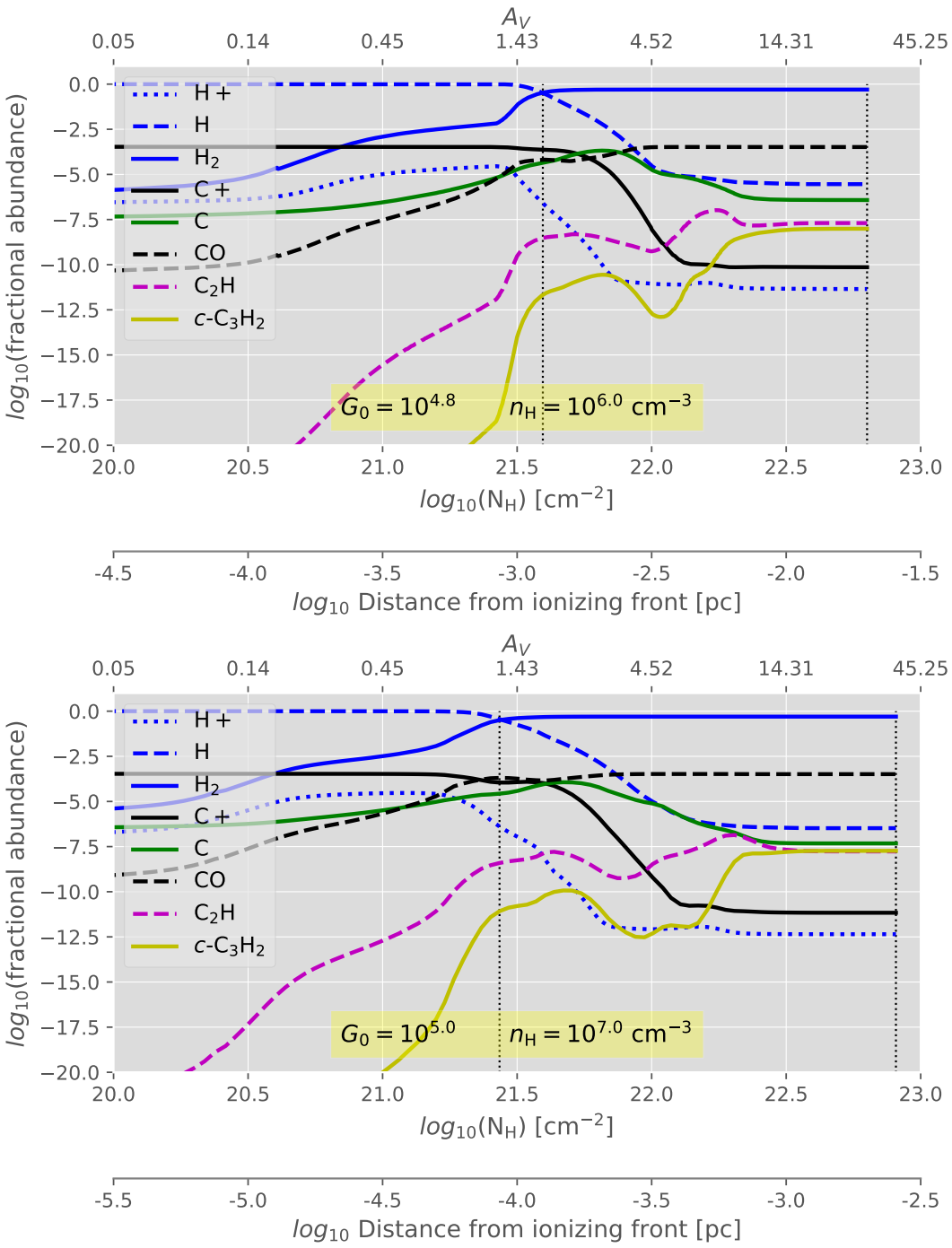

Figure 4.7: PDR models for M8 for $G_0 = 10^{4.8}$ and $n_H = 10^5$ cm^{-3} (left panel) and $G_0 = 10^5$ and $n_H = 10^7$ cm^{-3} (right panel). The fractional abundances (n_X/n_H) are represented by the color codes/lines patterns indicated on the plots and measured by the ordinates. The top abscissa indicates the corresponding visual extinction (A_V) as seen from the ionizing front (the impinging radiation field goes from left to right of the plot). The first bottom abscissa gives the corresponding total hydrogen column density N(H). A second bottom abscissa shows the actual distance (in parsec) from the ionizing front. The vertical dashed lines demarcate the region where most of the hydrogen gas is in molecular form.

the models with the lowest density and impinging radiation field (left) and with the highest density and radiation field (right) tested.

For the highest density model ($n_{\rm H} = 10^7$ cm^{-3}) we get relative abundances between 4×10^{-9} and 2×10^{-8} for C_2H and between 8×10^{-8} and 2×10^{-8} for c-C_3H_2, in the region where H_2 is more abundant than H (i.e., where H_2 becomes the main collision partner, indicated with vertical dashed lines in Fig. 4.7). Integrating from the layer where $n(H_2) \geq$ n(H) to the far edge of the slab, we get column densities of about 2×10^{15} cm^{-2} for C_2H and 10^{15} cm^{-2} for c-C_3H_2. That is, about three times and twenty five times larger than what we found from the rotational diagrams.

For the lowest density model ($n_{\rm H} = 10^6$ cm^{-3}) we get relative abundances between 3×10^{-9} and 2×10^{-8} for C_2H and between 2×10^{-12} and 10^{-8} for c-C_3H_2, in the region where $n(H_2)$ is dominant (i.e., for $A_{\rm V}$ between 1.8 and 28.6 mag, indicated by the vertical dashed lines in Fig. 4.7). The associated column densities are on the order of 10^{15} cm^{-2} for C_2H and 4×10^{14} cm^{-2} for c-C_3H_2. That is, between factors three and ten larger than what we found from the rotational diagrams for each species.

The difference between the observed column densities and those predicted by the homogeneous PDR models can arise from the unresolved clumpiness in the gas, which is not taken into account in the calculations based on our observations. Hence, the column densities estimated from observations should be considered lower limits of the actual column densities of the species.

The slab depth dependent [C_2H/C_3H_2] abundance ratios are shown in Fig. 4.8 for the same models presented in Fig. 4.7. The C_2H molecule is about ten orders of magnitude more abundant over most of the slab's length for all the cases studied. However, the abundance ratio decreases to just about factor two in the lower density model ($n_{\rm H} = 10^6$ cm^{-3}) toward the far edge of the slab. In the higher density model ($n_{\rm H} = 10^7$ cm^{-3}) instead the abundance ratio turns around as the gas cools down and C_3H_2 becomes about four times more abundant than C_2H. Gas temperatures reached at the far edge of the slab are about 45 K for the lower density model and about 60 K for the higher density model. Considering all the region of the slab where H_2 is the most abundant species, the average gas temperatures are about 100 K and 120 K for the lower and higher density PDR models, respectively. These average temperatures are similar to the values (100–150 K) we (Tiwari et al., 2018) obtained for this region of M8.

Despite not considering surface grain chemistry or mechanisms concerning PAH destruction due to UV radiation, the PDR models lead to temperatures comparable to our estimates based on the observations after using the same density values found with the non-LTE radiative transfer models. This is in favor of the argument that gas-phase chemistry is able to roughly explain the abundance of small hydrocarbons in high-UV flux PDRs.

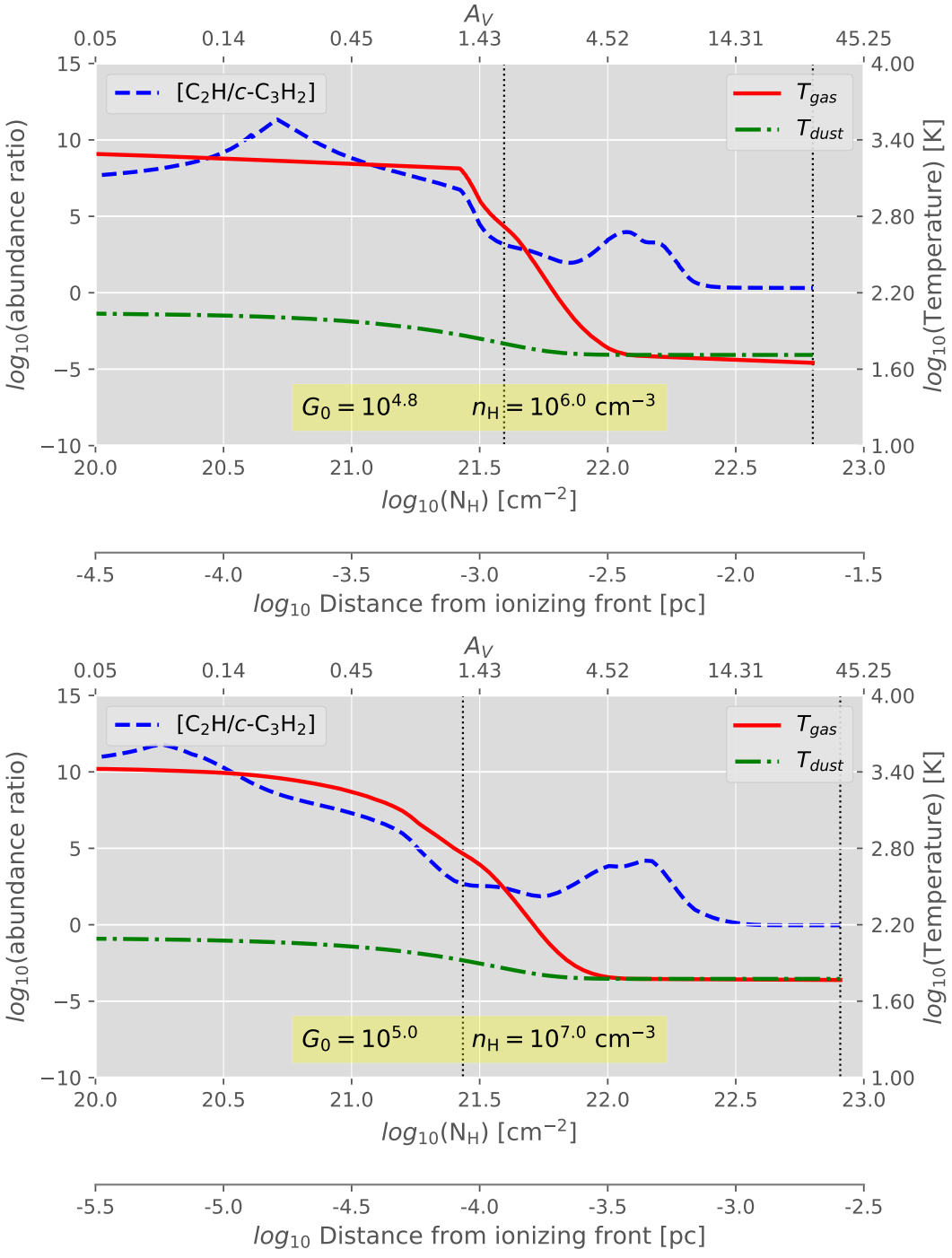

Figure 4.8: Abundance ratios of $[C_2H/c - C_3H_2]$ from the PDR models. The left ordinate corresponds to the abundance ratio while the right ordinate corresponds to the gas and dust temperatures. Other labels are as in Fig. 4.7.

4.5 Discussion

4.5.1 Physical conditions probed by two velocity components

Two spectrally resolved velocity components are seen in the $N = 5 \rightarrow 4$ transition of C_2H (Fig. 4.1) and are very prominent in all transitions of c-C_3H_2 (Fig. 4.2). These two components probe regions of different temperatures and densities. As mentioned before, the low velocity component (2–8 km s^{-1}) is a part of the gas in the foreground veil and the high velocity component (8–15 km s^{-1}) is a part of the gas close to Her 36 and the background molecular cloud. Owing to the prominent foreground veil feature in c-C_3H_2, it seems to be a better probe of the warm PDR as compared to C_2H.

The rotational diagram analysis performed in Sect. 4.4.2, provides us with the column densities and abundances of the low and high velocity components of C_2H and c-C_3H_2. Lower column densities and abundances are found in the foreground veil compared to the high column densities and abundances obtained in the gas close to Her 36 and in the background molecular cloud. As described in Sect. 4.4.3, the non-LTE RADEX modeling provides us with H_2 volume density estimates. The low velocity component (corresponding to the foreground veil) probes the high density gas in the range of 5×10^5–5×10^6 cm^{-3}, while the high velocity component (corresponding to the gas close to Her 36 and in the background molecular cloud) probes both high and low density gas in the range of 5×10^4–5×10^6 cm^{-3}.

4.5.2 Comparison with the Orion Bar PDR

The Orion Bar, an elongated structure in the Orion Nebula (M43), is the most-studied dense PDR (Tielens et al. 1993, Hollenbach & Tielens 1997 & Walmsley et al. 2000). In particular, it is an interesting source to study small hydrocarbon chemistry in the ISM. Hogerheijde et al. (1995), Walmsley et al. (2000), and Andree-Labsch et al. (2017) described the geometry of the Orion Bar where the prominent O stars in the Trapezium illuminate the PDR, whose orientation changes from face-on to an edge-on relative to the line of sight and which appears to be located at the edge of the [H II] blister (Peng et al., 2012). Recent observational studies of small hydrocarbons toward this PDR have been reported by Cuadrado et al. (2015), who studied the chemistry and spatial distribution of C_2H, C_4H, c-C_3H_2, and c-C_3H and by Nagy et al. (2015), who constrained the physical conditions of the C_2H (high transitions from $N = 6 \rightarrow 5$ to $10 \rightarrow 9$) emitting gas toward the Orion Bar. Moreover, Joblin et al. (2018) reported that the formation of CH^+ in PDRs like the Orion Bar opens a hot chemistry channel that leads to the formation of CO.

In Table 4.5, we compared the C_2H and c-C_3H_2 column densities toward M8 that we observe and obtain from modeling with those reported toward the Orion Bar by **?**. We find the observed column densities to be similar in both PDRs, which was expected as we also found such similarities in the H_2 volume density, in the kinetic temperature and in the CO and [C II] luminosities (Tiwari et al., 2018).

Table 4.5: Column densities of C_2H and c-C_3H_2 in M8 and the Orion Bar.

Species	Column densities $\log_{10}(N)$ (cm^{-2})			
	Observed[a]		PDR model[b]	
	M8	Orion	M8	Orion
C_2H	14.6	14.6	15	14.1–14.8
c-C_3H_2	13.5	13.1	14.6–14.9	12.2–12.9

[a] Values for M8, calculated from Table 4.4 and for the Orion Bar, obtained from Cuadrado et al. (2015, Table 7).

[b] Values for M8, obtained from the modeling results presented in Sect. 4.4.4 and for the Orion Bar, obtained from Cuadrado et al. (2015, Table 7).

On the other hand, we found significant differences between the observed and the modeled column density of the c-C_3H_2 molecule. In the case of Orion it is about one order of magnitude lower than estimated from the observations. In the case of M8 the modeled column density is between one and two orders of magnitude larger than estimated from observations, which is in line with the assumption that the column densities we have determined should be considered lower limits. This suggests that there might be a significant difference between the results obtained with the Meudon PDR model used by Cuadrado et al. (2015) and our PDR model based on Meijerink & Spaans (2005). As shown in Appendix B.2, we ran our models for the Orion Bar with the same input parameters ($n_H = 4 \times 10^6$ cm^{-3} and $G_0 = 1.17 \times 10^4$) as used by Cuadrado et al. (2015, Fig. 17, right panel). We believe that the different chemical networks used in each model that lead to the formation and destruction of the c-C_3H_2 molecule, are mainly responsible for their different column density predictions.

4.6 Conclusions

In this paper, we report APEX and IRAM 30 m observations of the $N = 1 \rightarrow 0$, $3 \rightarrow 2$, and $5 \rightarrow 4$ transitions of C_2H and of the $J = 2 \rightarrow 1$, $6 \rightarrow 5$, $7 \rightarrow 6$, and $8 \rightarrow 7$ transitions of c-C_3H_2 toward M8. We presented the spectra of eighteen observed hfs components of C_2H and five observed transitions of ortho and para species of c-C_3H_2 along with the velocity integrated intensity maps of the brightest $N = 1 \rightarrow 0$, $J = 3/2 \rightarrow 1/2$, $F = 2 \rightarrow 1$, and $N = 3 \rightarrow 2$, $J = 7/2 \rightarrow 5/2$, $F = 4 \rightarrow 3$ transitions of C_2H.

As discussed in Sect. 4.4.2, we inferred column densities ranging from 10^{12} to 10^{14} cm^{-2}. C_2H is more abundant than c-C_3H_2 with an abundance $\sim 10^{-8}$. The C_3H_2

ortho/para ratio is calculated to be $\sim$ 2.2 for low velocity component (corresponding to the gas in the warm foreground veil) and 3.3 for high velocity component (corresponding to the gas near Her 36 and the background molecular cloud). We also expect c-C_3H_2 to be a better probe than C_2H for the warm PDR owing to its well-defined low velocity component feature (seen in Fig. 4.2).

Using non-LTE RADEX modeling (Sect. 4.4.3), we constrained the H_2 volume densities of the hydrocarbon emitting gas to 5×10^4 to 5×10^6 cm^{-3}. In Sect. 4.4.4, we compared the observed column densities with updated PDR models and they matched the observed C_2H column densities reasonably well (by a factor of $\sim$ 3) but predict higher values for c-C_3H_2 (by a factor of $\sim$ 10–25). This discrepancy might arise from clumpy gas structure that we do not resolve with our observations. Therefore, the column densities derived from our data should be considered to be lower limits. The spatial distribution of PAH emission does not follow the C_2H emission. This is consistent with PDR models, which do not require PAH fragmentation to explain the observed column densities of C_2H and c-C_3H_2 in M8.

Chapter 5

Using diffuse and dense gas tracers as diagnostic tools to study the deeply embedded star-forming region Messier 8 East

5.1 Introduction

Massive stars contribute significantly in the evolution of the galaxies by injecting radiative and mechanical energy into the interstellar medium (ISM). This energy input stirs the environment around massive stars through stellar winds, ionization and heating of the gas, and supernovae explosions resulting to a change in the chemical composition and structure of the ISM. Hence, interaction of massive stars with their surroundings can affect the star formation process either by ceasing star formation or by triggering it. Formation of cloud and intercloud phases in the ISM leads to disruption of molecular clouds can result in halting star formation, while compression of the surrounding gas or the propagation of photoionisation induced shocks can set off star formation (Urquhart et al. 2007 & Kim et al. 2013). Massive stars also give rise to bright HII regions and photodissociation regions (PDRs). HII regions comprise hot ionized gas irradiated by strong ultraviolet (UV, $h\nu > 13.6$ eV) radiations from a nearby star. PDRs are at the interface of these HII regions and the cold molecular cloud shielded from the illuminating star (Hollenbach & Tielens, 1999), and here the thermal and chemical processes are regulated by far-UV (FUV, 6 eV $< h\nu <$ 13.6 eV) photons. In order to understand how the ISM gets affected from the interaction with massive stars, it is of fundamental importance to study massive star-forming regions.

From the previous chapters, we know that M8 region harbors one of the brightest HII regions and PDRs in our galaxy. It is located relatively nearby at a distance $\sim$ 1.25 kpc ($1'$ corresponds to 0.36 pc) from us (Damiani et al. 2004 & Arias et al. 2006). M8 is associated with two major star-forming regions: the main body of M8 (from now M8 main), powered by the bright stellar system Herschel 36 (Her 36) and the region south-east of M8, M8 east (M8 E), with at least two massive stars being formed in it and which rivals the brightness of M8 at IR and submm wavelengths (Tothill et al., 2008). Using SOFIA, APEX and IRAM 30 m telescopes, we performed an extensive survey of M8 main, as reported in Tiwari et al. (2018) & Tiwari et al. (2019). We described the morphology of the area around Her 36, determined the physical

Table 5.1: Line parameters of various observations toward M8 E.

Species	ν (GHz)	E_{up} (K)	θ ($''$)	peak line flux (K km s^{-1})	rms (K km s^{-1})	n_{crit}[a](cm^{-3})
			$J = 1 \rightarrow 0$			
CO	115.271	5.5	22.5	303.9	1.1	2.2×10^3
^{13}CO	110.201	5.3	23.5	86.9	0.33	1.9×10^3
N_2H^+	93.173	4.5	27.8	20.3	0.21	3.7×10^5
HCN	88.632	4.3	29.3	77.7	0.17	1×10^6
H^{13}CN	86.339	4.1	30.0	9.0	0.12	
HCO$^+$	89.189	4.3	29.1	42.6	0.21	1.9×10^5
H^{13}CO$^+$	86.754	4.2	30.0	4.1	0.16	1.8×10^5
HNC	90.663	4.4	28.6	25.4	0.21	3.2×10^5
HN^{13}C	87.090	4.2	30.0	3.0	0.17	

[a] Critical densities calculated for species whose collisional rate coefficients are provided by LAMDA. For CO and ^{13}CO, the coefficients are determined at 50 K and for N_2H^+, HCN, HCO$^+$, H^{13}CO$^+$ and HNC, the coefficients are determined at 30 K.

conditions of the gas surrounding it and shed some light on the formation process of hydrocarbons in M8 main, which is a high UV flux PDR with $G_0 \sim 10^5$ in Habing units.

M8 E is a massive star-forming region about 5 pc in projected distance away from M8 main and it lies within a large molecular cloud of $\sim$ few arcmin size (roughly 1 pc) (Tothill et al., 2008). A small (< 0.13 pc^2, which is ~ 1 arcmin^2), but quite rich embedded cluster comprising 7 IR sources is associated with the molecular gas. It includes a ZAMS B2 star powering a very small ($0.6''$ in diameter, 750 AU) HII region, known as M8E-Radio, and, only $\sim 7''$ (0.04 pc) away, a massive young stellar object (YSO), M8E-IR, which is likely to become a BO star and dominates the cluster luminosity up to ~ 24 μm (Linz et al., 2008). M8 E has been studied extensively in the millimeter wavelength regime as a candidate for massive protostars (Beltrán et al., 2006). Few submillimeter studies have been done on M8 E by Tothill et al. (2002), Zhang et al. (2005) and Linz et al. (2008). Among them, Zhang et al. (2005) studied high-velocity molecular gas around M8 E by mapping the CO $J = 2 \rightarrow 1$ transition and reported molecular outflow.

5.2 Observations

Observations of the $J = 1 \rightarrow 0$ transition of CO, ^{13}CO, N_2H^+, HCN, H^{13}CN, HCO$^+$, H^{13}CO$^+$, HNC and HN^{13}C were performed using the IRAM 30 m telescope in August 2016. Along with lines from the above mentioned molecules, most of the 3 mm range was observed using the EMIR receivers (Carter et al., 2012) with a velocity resolution of 0.65 km s^{-1}. Mapping observations in OTF total power mode centered on M8E-IR at R.A. (α, J2000) = $18^h04^m53^s.3$ and Dec. (δ, J2000) = $-24°26'42.3''$ (Tothill et al., 2008). The CO, ^{13}CO and N_2H^+ line maps have a size of $\sim 240'' \times 240''$, while the HCN, H^{13}CN, HCO$^+$, H^{13}CO$^+$, HNC and HN^{13}C line maps have a size of $\sim 180'' \times 180''$. Each subscan lasted 25 s and the integration time on the off-source reference position was 5 s. The pointing accuracy ($< 3''$)

was maintained by pointing at the bright calibrator 1757-240 every 1−1.5 hrs. We also did pointed observations, which were integrated deeply toward the M8E-IR position providing us with a better S/N ratio, useful for spectral analysis. A forward efficiency $\eta_{\rm f} = 0.95$ and the beam coupling efficiency $\eta_{\rm c} = 0.69$ were adopted for EMIR receivers. These values were taken from the (2015) IRAM commissioning report.

The reduction of the calibrated data to produce spectra and maps shown throughout the chapter, were done using the Continuum and Line Analysis Single dish Software (CLASS) and GREnoble Graphic (GREG) softwares that are a part of the Grenoble Image and Line Data Analysis Software (GILDAS) package. All observations are summarized in Table 5.1.

5.3 Results

5.3.1 Spatial distribution of the molecular line emission

The line parameters, which include the emission maxima and rms noise as obtained from the velocity integrated intensity maps and the calculated critical densities of the observed molecules, are given in Table 5.1. Figure 5.1 shows velocity integrated intensity maps of $J = 1 \rightarrow 0$ transition lines of CO, ^{13}CO, N_2H^+, HCN, H^{13}CN, HCO$^+$, H^{13}CO$^+$, HNC and HN^{13}C. The intensities of the N_2H^+ and HCN lines were integrated over a velocity range of 0 to 20 km s^{-1} and -5 to 20 km s^{-1}, respectively, in order to cover their hyperfine structure (hfs) components. The emission intensities from all molecules peak at or very close to M8E-IR ($\Delta\alpha = 0''$, $\Delta\delta = 0''$). The distribution of CO emission is spread out the most, while that of N_2H^+ is the most concentrated. The CO and ^{13}CO emission is extending to the south-west and north-east of M8E-IR. Molecules with high critical densities such as HCN, HCO$^+$ and HNC, also have these extended emission but the south-west branch is brighter compared to the north-eastern one. In contrast, only the south-west branch is seen in the lines of their isotopologues, which have similar critical densities. In addition to the brightest emission at M8E-IR, the intensity distribution of N_2H^+ shows a secondary peak in the south-west of M8E-IR ($\Delta\alpha = –55''$, $\Delta\delta = –55''$).

Recent studies have shown that the $J = 1 \rightarrow 0$ transition of N_2H^+ is a more reliable dense gas tracer compared to $J = 1 \rightarrow 0$ transition HCN, HCO$^+$ and HNC (Kauffmann et al. 2017, Pety et al. 2017 & Brinkmann et al. in prep.). Despite having high critical densities, the $J = 1 \rightarrow 0$ transition of HCN, HCO$^+$ and HNC were observed in GMCs Orion A and B from relatively low density gas ($n_{\rm H} \sim 10^3$ cm^{-3}), thus the gas responsible for the emission of these species is not necessarily cold or dense (Kauffmann et al. 2017 & Pety et al. 2017). We also see that the emission distribution of HN^{13}C follows that of N_2H^+ in M8 E, similar to the study done by Nakamura et al. (2019) for OMC-2. Both N_2H^+ and HN^{13}C probe gas with very high visual extinction $A_{\rm v} > 35$ (Pety et al., 2017), hence tracing dust embedded dense cloud cores.

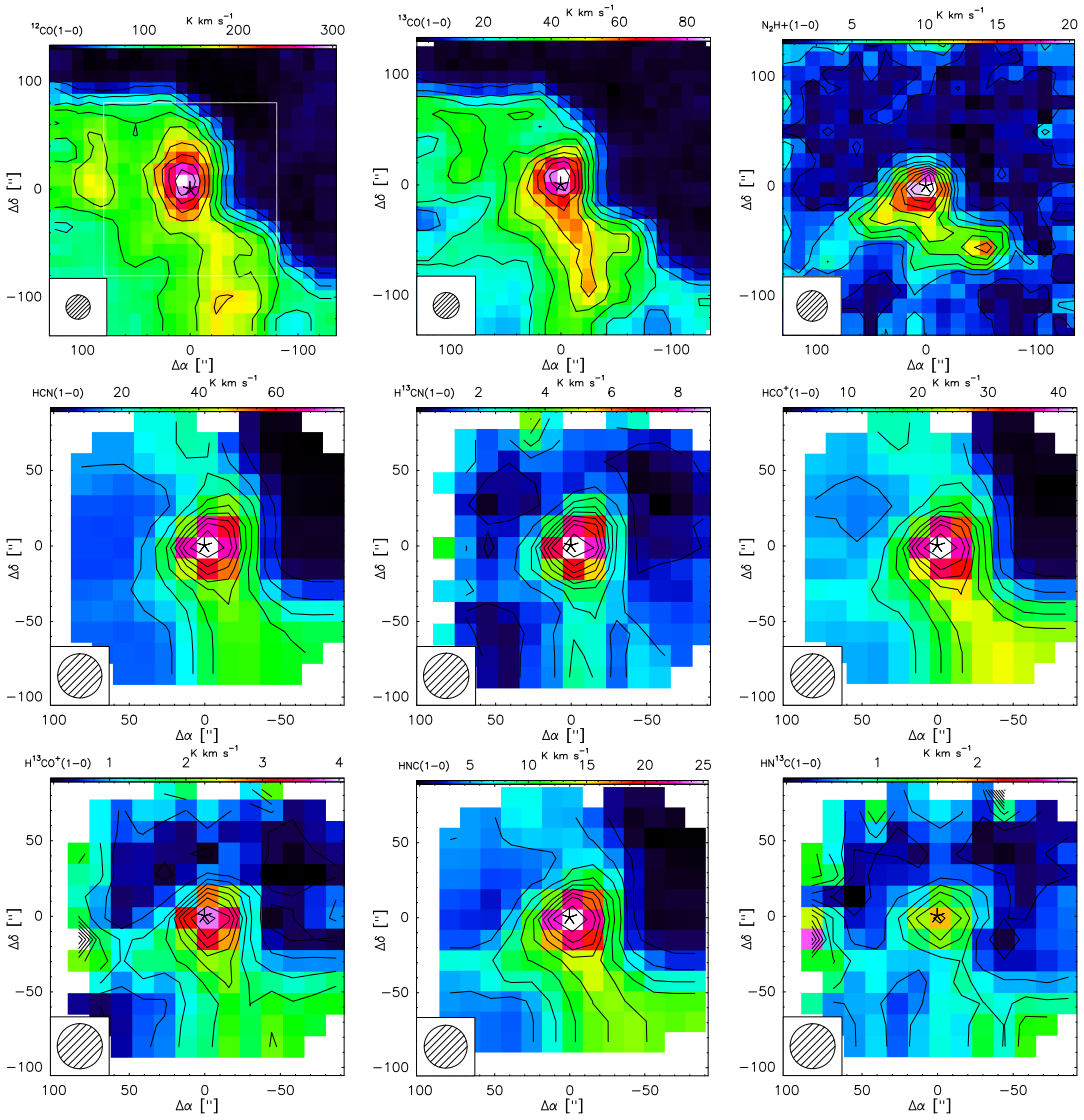

Figure 5.1: Colour maps of the velocity integrated intensity of the $J = 1$ *to* 0 transition of CO, ^{13}CO, N_2H^+, HCN, H^{13}CN, HCO$^+$, H^{13}CO$^+$, HNC and HN^{13}C toward M8 E. The square outlined by the white dashed lines in the map of CO, denotes the area of the smaller maps of HCN, H^{13}CN, HCO$^+$, H^{13}CO$^+$, HNC and HN^{13}C. The central position corresponds to M8E-IR at R.A,(α, J2000) = $18^h04^m53^s.3$ and Dec. (δ, J2000) = $-24°26'42.3''$, marked with an asterisk. The contour levels are from 10% to 100% of the corresponding peak emission given in Table 5.1. All maps are plotted using original FWHM beam sizes shown in the lower left of each map and listed in Table 5.1.

The emission intensity of all molecules decreases dramatically in the north (from $\sim \Delta\delta = 100''$, visible in CO and ^{13}CO maps) and north-west (from $\sim \Delta\alpha = 40''$, visible in all maps) of M8E-IR. This region corresponds to a different molecular cloud (Dame et al., 2001), which has a different LSR velocity ($\sim$ 26 km s^{-1}) seen in the CO and ^{13}CO lines. This other velocity component was also reported by Mitchell et al. (1992) in their CO $J = 2 \rightarrow 1$ spectrum and was suggested to be present along the same line of sight, but unrelated to M8E-IR.

5.3.2 Ancillary data

It is important to understand how the cold dense molecular clouds are related to the hot ionized gas and for this, multi-wavelength studies play a major role. We compared our observed data with the observations available in the IR and submm regimes. First, we extracted the 22 μm dust continuum image from the all-sky WISE catalog. The mid-IR dust continuum probes the warm dust in HII regions, which absorbs UV and far-UV radiation from a nearby massive star and re-emits in the IR regime. The 22 μm emission wavelength is similar to that of the Multiband Infrared Photometer for Spitzer aboard the Spitzer Space Telescope (MIPSGAL, Carey et al. 2009), the 24 μm band, which has been widely studied and is found to be a direct tracer of HII regions as it correlates very well with the 21 cm radio continuum emission because the hot plasma that gives rise to the free-free thermal emission at radio wavelengths is ionised by the same sources that are responsible for the IR emission (Bania et al. 2010 & Anderson et al. 2014). Second, we used the 870 μm dust continuum data from ATLASGAL, which is an unbiased survey covering 420 square degrees of the inner Galactic plane and was performed with the LABOCA instrument of the 12 m APEX telescope. The dust continuum emission in the submillimeter range is probing the dense and cold clumps in the ISM, hence tracing the earliest phases of (high-mass) star formation. Figure 5.2 (a) and (b), show the 22 μm and the 870 μm emission contours overlaid on the velocity integrated intensity map of $J = 1 \rightarrow 0$ transition of ^{13}CO corresponding to the colour scale in the background. Both the IR and submm continuum emission peak very close to M8E-IR (marked with an asterisk) and M8E-radio (marked with a triangle). While the 24 μm IR emission is probing the warm dust heated by the HII region, the 870 μm ATLASGAL emission follows the structure of the ^{13}CO emission distribution better with a bright extension toward the south-west of M8E-IR. To investigate further the nature of the bright south-west extension, we overlay the contours of ATLASGAL 870 μm on the velocity integrated intensity map of N_2H^+ corresponding to the colour scale in the background. As can be seen from Fig. 5.2 (c), The ATLASGAL contours perfectly follow the N_2H^+ emission distribution with the second emission peak of N_2H^+ at ($\Delta\alpha$, $\Delta\delta$) = (–55″, –55″), hence probing the high density gas. Lastly, to explore the PDR environment, we used the 8 μm data from the GLIMPSE archive observed with Spitzer Space Telescope. The 8 μm band of the Infrared Array Camera (IRAC) used by Spitzer traces emission

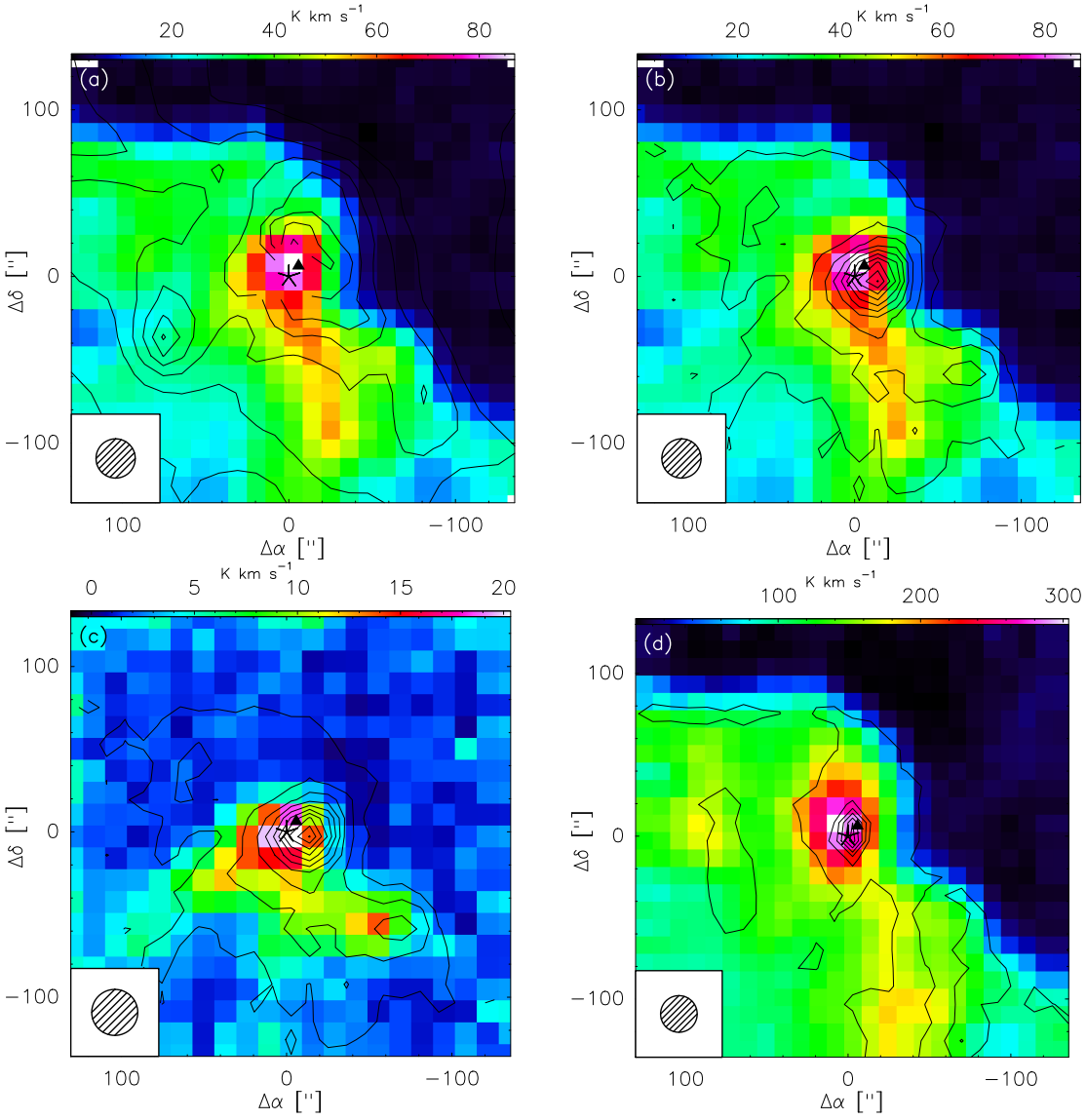

Figure 5.2: Top row: Colour map of the velocity integrated intensity of $J = 1 \rightarrow 0$ transition of ^{13}CO overlaid with contours of: (a), WISE 22 μm mid-IR continuum emission and (b), ATLASGAL 870 μm dust continuum emission toward M8 E. Bottom row: (c), shows the colour map of the velocity integrated intensity of $J = 1 \rightarrow 0$ transition of N_2H^+ overlaid with ATLASGAL 870 μm dust continuum emission and (d), shows the contours of 8 μm dust continuum emission overlaid on the colour map of the velocity integrated intensity map of CO. The central position corresponds to M8E-IR at R.A. (α, J2000) = $18^h04^m53^s.3$ and Dec. (δ, J2000) = $-24°26'42.3''$, marked with an asterisk and the HII region, M8E-radio, at R.A. (α, J2000) = $18^h04^m52^s.8$ and Dec. (δ, J2000) = $-24°26'36''$ is represented with a black triangle. The contour levels are 5% to 100% by steps of 10% in both plots.

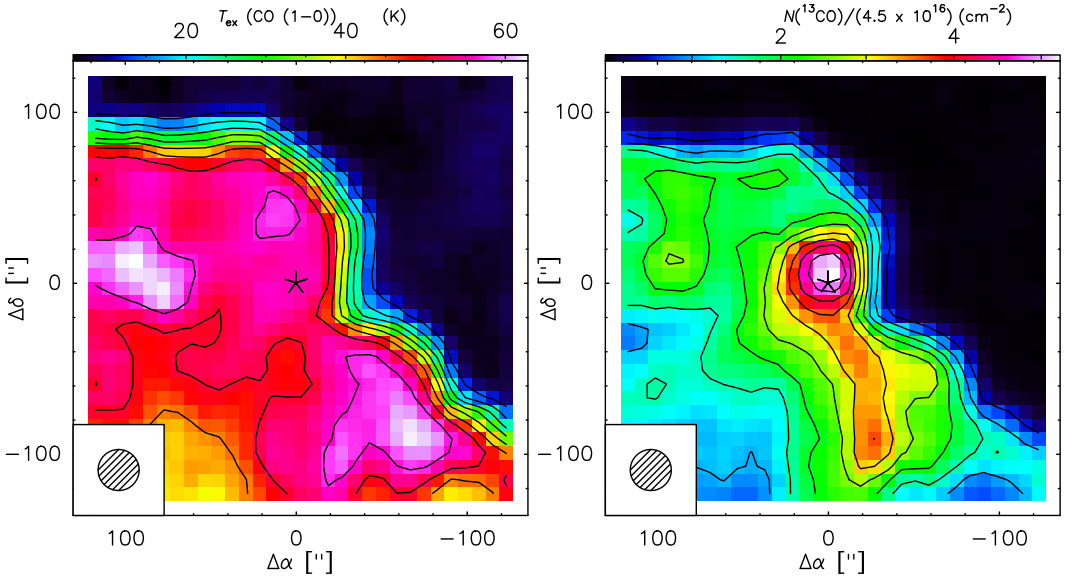

Figure 5.3: Left panel: shows the excitation temperature $T_{\rm ex}$ defined for $J = 1 \rightarrow 0$ transition of CO and ^{13}CO and right panel: shows the total column density of ^{13}CO, $N(^{13}\mathrm{CO})$. The central position corresponds to M8E-IR at R.A. (α, J2000) = $18^h04^m53^s.3$ and Dec. (δ, J2000) = $-24°26'42.3''$, marked with an asterisk. The contour levels are from 10% to 100% in steps of 10% corresponding peak emission (Table 5.1). The values of $T_{\rm mb}$ and that of $\int T_{\rm mb}(^{13}\mathrm{CO})\mathrm{dv}$ for the $J = 1 \rightarrow 0$ transition used to calculate $T_{\rm ex}$ and $N(^{13}\mathrm{CO})$ were extracted from maps convolved to the same resolution of $24''$.

from the PAHs, which are large hydrocarbon molecules (or small dust grains) that get excited by strong UV radiation. The fluorescent IR emission from these PAHs is a result of the FUV pumping and this emission arises from the PDR surface of dense molecular clouds, hence this emission is believed to be related to PDR layers resultant from recent massive star formation activity (Tielens, 2008). Figure 5.2 (d), shows the velocity integrated intensity map of CO in colour scale overlaid with contours of 8 μm dust continuum. It traces the warm CO gas emission distribution.

5.4 Analysis

We used several complementary methods to determine temperature and density of the gas responsible for the emission of various species observed toward M8 E with IRAM 30 m telescope. We started with calculating the excitation temperatures and column densities of CO and ^{13}CO using their $J = 1 \rightarrow 0$ transition in Sect. 5.4.1. In Sect. 5.4.2, we used CH_3CCH, as a probe of the dense gas temperature and used it to determine the column densities of the lines from N_2H^+, HCN, $H^{13}CN$, HCO^+, $H^{13}CO^+$, HNC and $HN^{13}C$ in Sect. 5.4.3. To complete our investigation about the

physical conditions, we made use of the non-LTE radiative transfer models to constrain the volume densities of the warm and cold gas of M8 E in Sect. 5.4.4.

5.4.1 Excitation temperature and column density distributions of CO and ^{13}CO

In the process of radiative transfer, we ignored scattering and assumed that the medium through which the radiation is traveling is uniform at an excitation temperature, $T_{\rm ex}$, such that the radiation source function is equivalent to the Planck function at $T_{\rm ex}$. By using the Rayleigh-Jeans approximation and taking the beam filling factor to be unity, we can express the observed main beam brightness temperature, $T_{\rm mb}$, in terms of $T_{\rm ex}$ (Peng et al., 2012, Eq. 1). A detailed description about radiative transfer can be found in Mangum & Shirley (2015). We took the background temperature to be equal to that of the cosmic background radiation of 2.73 K and it's contribution to the $T_{\rm ex}$ can be neglected as it will be $\leq 2\%$ of the resulting value.

Assuming that $T_{\rm ex}$ for both CO and ^{13}CO is the same and CO is optically thick, we calculated the excitation temperature using the $J = 1 \rightarrow 0$ transition of CO as

$$T_{\rm ex} = \frac{5.53}{ln\big(1 + \frac{5.53}{T_{mb}({\rm CO})}\big)}{\rm K}\,, \tag{5.1}$$

where $T_{\rm mb}$, the main beam brightness temperature, is in K and its values are obtained from the peak temperature map of CO in the velocity range of $\sim$ 0–20 km s^{-1}. Figure 5.3 left panel shows the distribution of the resulting $T_{\rm ex}$ around M8E-IR, peaking in the east and south west of M8E-IR, with a maximum value of $\sim 63 \pm 1$ K.

We used the computed $T_{\rm ex}$ and the velocity integrated intensity flux, $\int T_{\rm mb}(^{13}CO)dv$, to calculate the total column density of ^{13}CO, $N(^{13}{\rm CO})$, by

$$N(^{13}{\rm CO}) = 4.5 \times 10^{13}(T_{\rm ex} + 0.88)\ \exp\left(\frac{5.3}{T_{\rm ex}}\right)\ \int {\rm T_{mb}}(^{13}{\rm CO}){\rm dv\ cm^{-2}}\,. \tag{5.2}$$

where, $T_{\rm ex}$ is in K and $\int T_{\rm mb}(^{13}{\rm CO}){\rm dv}$ is in K km s^{-1}. The resulting $N(^{13}{\rm CO})$ distribution is shown in Fig. 5.3 right panel, peaking at M8E-IR with a maximum value $\sim (2 \pm 0.05) \times 10^{17}$ cm^{-2}. The $N(^{13}{\rm CO})$ distribution peak is different from the $T_{\rm ex}$ peak because column density depends on velocity integrated intensity flux values that rely on the velocity widths, which are largest at M8E-IR. We calculated the H_2 column density, $N(H_2)$, with a peak value of $\sim 1.5 \times 10^{23}$ cm $^{-2}$, by adopting an isotopic ratio of [CO/^{13}CO] $\sim$ 63 (Milam et al., 2005) and a CO abundance ratio of [CO/H_2] $\sim 8.5 \times 10^{-5}$ (Tielens, 2010).

5.4.2 CH_3CCH as a thermometer for cold gas

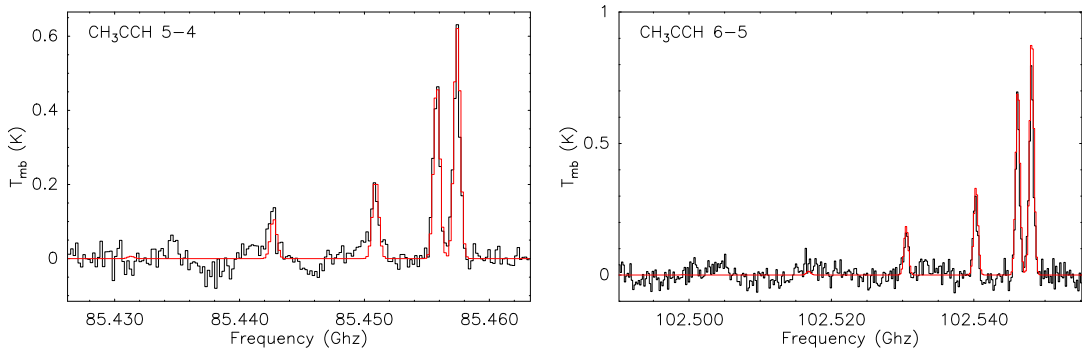

Figure 5.4: Spectra of $J = 5 \rightarrow 4$ and $6 \rightarrow 5$ transitions of CH_3CCH observed toward M8E-IR. In red are the best fit synthetic spectra generated by MCWeeds for the input parameters mentioned in Table 5.2.

Methyl acetylene, CH_3CCH, was first detected by Snyder & Buhl (1973) in Sgr B2. It is a symmetric top molecule with quantum numbers, J and K, which define the total angular momentum and the projection of the angular momentum along the symmetry axis respectively. For a given $J \rightarrow J-1$ transition, there are different K levels that span a wide range in energy above the ground state but have frequencies very close to each other. The electric dipole moment of CH_3CCH is parallel to the symmetry axis, so the only possible $J \rightarrow J-1$ transitions have $\Delta K = 0$. For a given J the different K levels are connected only through collisions and hence the total population in each K ladder is a function of only kinetic temperature of the dense gas responsible for the emission of CH_3CCH. The temperature can be determined from the (measured) relative level populations. This makes CH_3CCH an excellent molecular cloud thermometer (Bergin et al. 1994 and Giannetti et al. 2017). It is found that CH_3CCH has an extended emission region and it traces colder gas compared to CO emitting gas (Fontani et al., 2002).

In order to derive the dense gas temperature, we simultaneously fit the $J = 5 \rightarrow 4$ and $6 \rightarrow 5$ transitions of CH_3CCH. We used MCWeeds (Giannetti et al., 2017), which provides an external interface between Weeds (a CLASS extension for the analysis of millimeter and submillimeter spectral surveys, Maret et al. 2011) and PyMC[1] (a python package to efficiently code a probabilistic model and draw samples from its posterior distribution using Markov chain Monte Carlo techniques, Patil et al. 2010). Weeds generates synthetic spectra by solving the radiative transfer equation assuming LTE and takes into account the finite angular resolution of the observations, but does not optimise algorithms. On the other hand, PyMC implements Bayesian statistical models and fit algorithms. Initial guesses are given for a set of input parameters along with their probability distribution and the range over which they should be varied. According to the best fit model over the given spectrum of a transition of a molecule, MCWeeds gives the new adjusted parameters with their errors (for more details see

[1]https://pymc-devs.github.io/pymc/index.html

Table 5.2: Priors, given input and resulting output from the best-fit models.

	Temperature (K)	Column density (Log(cm^{-2}))	line width (km s^{-1})	velocity (km s^{-1})
		CH_3CCH $J = 5 \rightarrow 4$ & $6 \rightarrow 5$		
Prior	Truncated normal	Normal	Truncated normal	Normal
	$\mu = 50$	$\mu = 14$	$\mu = 5$	$\mu = 0$
Input	$\sigma = 30$	$\sigma = 2$	$\sigma = 3$	$\sigma = 2$
	low = 10, high = 80		low = 1, high = 35	
Output	32.9 (1.4)	14.72 (0.047)	2.03 (0.05)	-0.24 (0.019)
		N_2H^+ $J = 1 \rightarrow 0$		
Prior	Fixed	Normal	Truncated normal	Normal
		$\mu = 14$	$\mu = 5$	$\mu = 0$
Input	value = 33	$\sigma = 2$	$\sigma = 3$	$\sigma = 2$
			low = 1, high = 35	
Output	33	14.11 (0.042)	2.24 (0.03)	-0.28 (0.01)
		HCN $J = 1 \rightarrow 0$		
Prior	Fixed	Normal	Truncated normal	Normal
		$\mu = 14$	$\mu = 5$	$\mu = 0$
Input	value = 33	$\sigma = 2$	$\sigma = 3$	$\sigma = 2$
			low = 1, high = 35	
Output	33	15.24 (0.042)	3.07 (0.08)	-0.37 (0.03)
		$H^{13}CN$ $J = 1 \rightarrow 0$		
Prior	Fixed	Normal	Truncated normal	Normal
		$\mu = 14$	$\mu = 5$	$\mu = 0$
Input	value = 33	$\sigma = 2$	$\sigma = 3$	$\sigma = 2$
			low = 1, high = 35	
Output	33	13.84 (0.037)	2.25 (0.02)	-0.22 (0.008)
		HCO^+ $J = 1 \rightarrow 0$		
Prior	Fixed	Normal	Truncated normal	Normal
		$\mu = 14$	$\mu = 5$	$\mu = 0$
Input	value = 33	$\sigma = 2$	$\sigma = 3$	$\sigma = 2$
			low = 1, high = 35	
Output	33	14.84 (0.027)	2.45 (0.038)	-0.13 (0.009)
		$H^{13}CO^+$ $J = 1 \rightarrow 0$		
Prior	Fixed	Normal	Truncated normal	Normal
		$\mu = 14$	$\mu = 5$	$\mu = 0$
Input	value = 33	$\sigma = 2$	$\sigma = 3$	$\sigma = 2$
			low = 1, high = 35	
Output	33	12.97 (0.045)	2.1 (0.03)	-0.23 (0.01)
		HNC $J = 1 \rightarrow 0$		
Prior	Fixed	Normal	Truncated normal	Normal
		$\mu = 14$	$\mu = 5$	$\mu = 0$
Input	value = 33	$\sigma = 2$	$\sigma = 3$	$\sigma = 2$
			low = 1, high = 35	
Output	33	14.35 (0.05)	2.59 (0.032)	-0.12 (0.007)
		$HN^{13}C$ $J = 1 \rightarrow 0$		
Prior	Fixed	Normal	Truncated normal	Normal
		$\mu = 14$	$\mu = 5$	$\mu = 0$
Input	value = 33	$\sigma = 2$	$\sigma = 3$	$\sigma = 2$
			low = 1, high = 35	
Output	33	13.24 (0.04)	2.1 (0.043)	-0.06 (0.01)

Giannetti et al. 2017 and Thiel et al. 2019).

To fit the spectrum, an input file is provided containing all the initial guesses of the parameters: column density (cm^{-2}), temperature (K), size of the emitting region (arcsec), radial velocity (km s^{-1}) and line width (km s^{-1}), rms noise (K), and calibration uncertainty for the spectral range. The input file also contains the name of the species, the frequency range in which the interested transition lies, the corresponding data file and the priors required to fit the observed spectrum. Using the ATLASGAL 870 μm image, we estimated the source size $\sim 40''$, which is larger

than the beam size ($\sim 30''$) at which CH_3CCH was observed. So, we fix the size of the emitting region = $30''$ (filling the beam completely). Similar to Giannetti et al. (2017), we used loosely informative priors for the parameters of the fit: A normal gaussian function for column densities and line widths, while a truncated normal gaussian function is used for temperatures and velocities. The probability distribution of these functions depend on the values of their mean, μ, and standard deviation, σ (A detailed description about priors can be found in Jaynes & Bretthorst 2003).

The given input (initial guesses) and the obtained output values of the fit parameters used in MCWeeds are listed in Table 5.2. The resulting dense gas temperature comes out to be ~ 32 K, which is quite similar to the kinetic temperature of the molecular gas estimated using NH_3 emission toward M8 E (Molinari et al., 1996). A total CH_3CCH column density, $N(CH_3CCH) \sim 5.3 \times 10^{14}$ cm^{-2} was obtained.

5.4.3 Column density estimates of N_2H^+, HCN, HCO^+, HNC, $H^{13}CN$, $H^{13}CO^+$ and $HN^{13}C$

From the above sections, Sect. 5.4.1 & 5.4.2, we got an estimate of the warm and cold gas temperatures using CO and CH_3CCH respectively. We assume the cold gas temperature (~ 32 K) estimated from CH_3CCH to be similar to the kinetic temperature of the gas responsible for the emission of N_2H^+, HCN, HCO^+, HNC, $H^{13}CN$, $H^{13}CO^+$ and $HN^{13}C$. So, we calculated their total column densities by fitting the synthetic spectra generated by MCWeeds to the observed spectra of their $J = 1 \rightarrow 0$ transition, keeping temperature and size fixed. The input and output parameters are mentioned in Table 5.2. The total column densities determined for the observed species in M8 E are relatively higher than those found in star forming regions with similar kinetic temperatures and with H_2 densities $\sim 10^4$–10^5 cm^{-3} (for example W 51 Watanabe et al. 2017).

5.4.4 Non-LTE analysis

In Sect. 5.4.1, 5.4.2 and 5.4.3, we used several techniques under the assumption of LTE to determine the column densities of the observed species. In order to verify these values and to constrain the volume densities, we used RADEX (van der Tak et al., 2007), which is a non-LTE radiative transfer program. Accounting for non-LTE effects is important while estimating column densities, mainly where it is possible to excite a given molecule even when the emitting region's volume density (called as effective density) is lower than the molecule's critical density. Shirley (2015) compares thoroughly the relevance of critical and effective density. Critical density is computed in the optically thin limit where radiative trapping is ignored (Shirley, 2015), hence it should only be considered as an upper limit for the density needed to excite the molecules (Pety et al., 2017).

Table 5.3: Comparison of column densities determined from RADEX and LTE analysis

Species	non-LTE (RADEX)			LTE
	T_k (K)	$n(H_2)$ (cm^{-3})	N(X) (cm^{-2})	N(X) (cm^{-2})
CO	60	$> 10^3$–10^4	(0.1–1) $\times$ 10^{19}	1.3 $\times$ 10^{19}
^{13}CO	50–60	10^4	1 $\times$ 10^{17}	2 $\times$ 10^{17}
N_2H^+	30–40	10^5–10^6	5 $\times$ 10^{13}	5.2 $\times$ 10^{14}
HCN	30–40	10^6	1 $\times$ 10^{15}	1.7 $\times$ 10^{15}
HCO^+	20	10^4–10^5	(0.1–1) $\times$ 10^{15}	7 $\times$ 10^{14}
$H^{13}CO^+$	20	10^4–10^5	(1–5) $\times$ 10^{12}	9.3 $\times$ 10^{12}
HNC	20–30	10^5	(0.5–1) $\times$ 10^{14}	2.2 $\times$ 10^{14}

RADEX is a code for performing statistical equilibrium calculations that uses escape the probability approximation in an isothermal and homogeneous medium, taking into account optical depth effects. We selected a uniform spherical geometry and the collisional rate coefficients, required for modeling, were taken from the database LAMDA. With the exception for $H^{13}CN$, CH_3CCH and $HN^{13}C$, LAMDA provides collisional rate coefficients for all species analysed in this paper. For CO and ^{13}CO, the collisional rate coefficients with H_2 are adopted from Yang et al. (2010). The N_2H^+–H_2 collisional rate coefficient are calculated (see Schöier et al. 2005) from the N_2H^+-He collisional rate coefficients given by Daniel et al. (2005) for hfs components. The HCN-H_2 collisional rate coefficients are provided by Hernández Vera et al. (2017) and the coefficients for the hfs components are computed using Braine et al (2019, in prep). The $H^{13}CO^+$-H_2 collisional rate coefficients are extrapolated from the HCO^+-H_2 collisional rate coefficients, which are provided by Flower (1999). The HNC-H_2 collisional rate coefficients are calculated by multiplying a factor of 1.37 to the HNC-He collision rates given by Dumouchel et al. (2010).

Assuming a background temperature of 2.73 K and taking the line width values of the above mentioned species from the observed spectra, we ran the models for a set of kinetic temperatures, volume densities and column densities to reach the intensities, which best fit our observed values. We computed grids in kinetic temperatures and volume densities. Guided from the gas temperature estimates that were obtained using LTE methods in Sect. 5.4.1 and 5.4.2, we adopted the values for kinetic temperatures, T_k, in a range of 20–40 K for the gas responsible for the emission of N_2H^+, HCN, HCO^+, $H^{13}CO^+$ and HNC, while for the warmer gas responsible for the emission of CO and ^{13}CO, we used a range of 40–70 K. And, a range of 10^3–10^7 cm^{-3} was taken for the H_2 volume densities. To fit the modeling results to the observed intensity values, we varied column densities of various species.

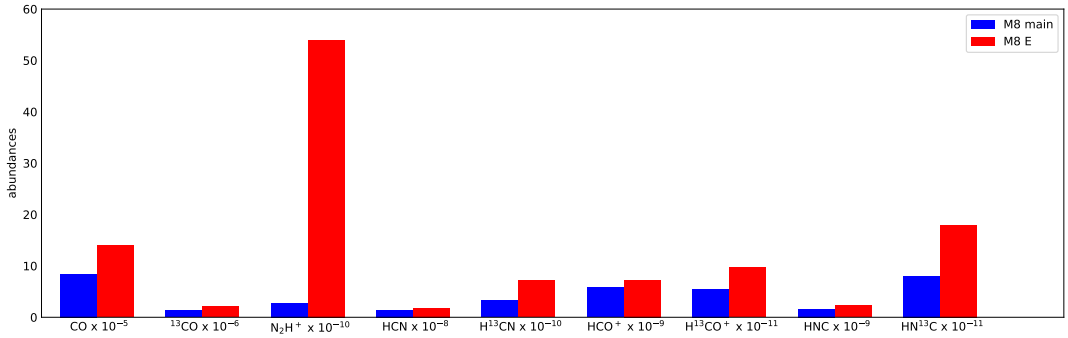

Figure 5.5: Chemical abundances of CO, ^{13}CO, HCN, H^{13}CN, HCO$^+$, H^{13}CO$^+$, HNC and HN^{13}C observed toward M8 E (shown in red) and M8 main (shown in blue).

The results from the RADEX modeling are reported in Table 5.3. We can see that the derived column densities, considering non-LTE conditions, deviate from the values obtained from LTE analysis for some species. For ^{13}CO and HCN, the column densities estimated from RADEX are very similar to the values calculated from LTE methods. While ^{13}CO is probing the gas with volume density, $n(H_2) \sim 10^4$ cm^{-3}, HCN probes denser gas with $n(H_2) \sim 10^6$ cm^{-3}. RADEX predicts lower column densities than those calculated by LTE analysis for CO, N_2H^+, H^{13}CO$^+$ and HNC. For HCO$^+$, both high and low column densities, compared to LTE values, are able to reproduce the observed line intensity. In general, the gas densities probed by all molecules are similar or higher than their critical densities except for HCO$^+$ and H^{13}CO$^+$, for which they probe gas densities below their critical densities as well. It's important to note that we are unable to precisely constrain the physical conditions due to the unavailability of higher transitions and at this stage we can only report the estimates of densities that are found from the non-LTE analysis.

5.5 Discussion

5.5.1 Comparison with M8 main

Given M8 E's proximity to M8 main and the fact that the two rival each other at IR and submillimeter wavelengths (Tothill et al., 2008), it is only natural to compare the two regions based on their chemical abundances and physical conditions. A comparison between the abundances, $N(X)/N(H_2)$, of various species observed toward M8 main and M8 E are presented in Fig. 5.5. For M8 E, the abundances are calculated from the column densities of various species, $N(X)$, obtained from the LTE analysis done in Sect. 5.4.1, 5.4.2 and 5.4.3 and the H_2 column density is calculated using the flux $\sim$ 5588 mJ/beam observed with ATLASGAL 870 μm continuum emission toward M8E-IR and by taking a dust temperature, T_d = 28.6 K (Tothill et al., 2002). The $N(H_2)$ calculated from dust emission is in reasonable

agreement with that calculated in Sect. 5.4.1, within a factor $\sim$ 1.5. For M8 main, we adopted the CO and ^{13}CO column densities as determined from the LTE analysis in Tiwari et al. (2018, Sect. 4.1) and for the other molecules analysed in the work, we used the same techniques as mentioned in Sect. 5.4.2 and 5.4.3. A full description of the 3 mm observations toward M8 main is given in Tiwari et al. (2019, Sect. 2.2).

From Fig. 5.5, it can be seen that in general the abundance of each species is found to be higher in M8 E than in M8 main. Though for most of the molecules the difference is small, for N_2H^+ and $HN^{13}C$, the abundances found toward M8 E are about 25 times and 2 times larger than in M8 main. A major destruction route of N2H+ is via CO, hence N2H+ is more abundant in CO depleted regions. Also, since N_2H^+ is argued to be a better density tracer compared to the other traditional molecules like HCN and HCO^+ (Kauffmann et al. 2017, Pety et al. 2017 and Brinkmann et al. in prep.), we infer that in M8 E, star-formation is occurring in a more densely embedded molecular cloud compared to the warmer and more diffuse PDR dominated environment of M8 main.

5.6 Conclusions

We reported the molecular inventory observed toward M8 E in the 3 mm regime using the EMIR receiver of the IRAM 30 m telescope and for the first time, presented the velocity integrated intensity maps of the $J = 1 \rightarrow 0$ transition of CO, ^{13}CO, N_2H^+, HCN, $H^{13}CN$, HCO^+, $H^{13}CO^+$, HNC and $HN^{13}C$ in this region.

From the ancillary data, analysed in Sect. 5.3.1, we found that the 24 μm IR emission probes the HII region associated with M8 E and the 870 μm submillimeter emission probes the dense gas responsible for star-formation. In Sect. 5.4, using several LTE and non-LTE methods, we determined the warm and cold gas temperatures $\sim$ 50 K and 30 K, respectively and the H_2 volume densities in the range of 10^4 cm^{-3} to 10^6 cm^{-3}. We summarised the differences in the estimated abundances of various species observed toward M8 E and M8, in Sect. 5.5, and we believe that star-formation is occurring in a denser environment in M8 E compared to M8. Furthermore, the $J = 1 \rightarrow 0$ transition of N_2H^+ and $HN^{13}C$ are excellent probes of high density, cold and and relatively young star-forming regions.

Chapter 6

Summary

6.1 Conclusions

We reported a comprehensive survey to explore the HII regions, PDRs and star-forming regions of the luminous Lagoon Nebula, using state-of-the-art submm and far infrared wavelength facilities: the IRAM 30 m and the APEX 12 m telescopes and SOFIA. Using various techniques, we were able to explore the effect of UV and FUV photons on the physical and chemical structure of one of the emission nebula in our Galaxy, M8. In the following, I summarise the work done in this thesis:

- In chapter 3, we characterised the PDR of M8 by analysing the emission from [C II], [C I] and several rotational transitions of CO in the FIR and submm wavelength range. In order to quantify the physical conditions in the PDR of M8, we used LTE and non-LTE methods. Based on our LTE analysis, we determined the column densities of the observed species and estimated masses of cold dust and CO warm gas associated with M8. Using non-LTE radiative transfer models, we constrained the physical conditions of the gas constituting the PDR of M8. Gas temperatures of 100–150 K and volume densities of 10^4–10^6 cm^{-3} are obtained. Furthermore, we found M8 to be a high-UV flux PDR with $G_0 \sim 10^4$–10^5 in Habing units. We achieved our goal of exploring the geometry of M8 by combining the spatial information provided by the ancillary data available in the optical, IR and radio regimes together with the velocity information provided by our observed data. M8 has a face on morphology with the cold molecular cloud behind the bright stellar system of Her 36 and a foreground layer forming a warm PDR veil, which is accelerating toward the observer and away from the ionising source.

- In chapter 4, we began with the task of establishing an inventory of hydrocarbons in M8 by observing several rotational transitions of C_2H and c-C_3H_2 using the IRAM 30 m and APEX telescopes. We then investigated the nature of the gas responsible for the emission of hydrocarbons. From our LTE analysis, we obtained column densities on the order of 10^{13} and 10^{14} cm^{-2} for c-C_3H_2 and C_2H respectively. Since these calculations were performed based on our observational data, which do not account for the unresolved clumpiness in the gas structure, these observed column densities must be considered as lower limits. Models including non-LTE conditions were employed to get the volume

densities ($\sim 5 \times 10^4$–5×10^6 cm^{-3}) of the gas responsible for the emission of hydrocarbons. In order to understand the formation process of hydrocarbons in the PDR of M8, we found that the gas-phase PDR models were able to predict the observed hydrocarbon column densities, within a factor of ~ 3 and 10–25. This suggests that gas-phase chemistry can roughly explain the observed abundances of hydrocarbons in high-UV flux PDRs like M8.

- In chapter 5, we explored the star-forming region of M8 E, which competes with M8 in its brightness at IR and submm wavelengths and is about 5 pc away from M8. We used several diffuse and dense gas tracers in order to determine the physical conditions and to investigate the morphology of the region. The IRAM 30 m telescope was used to perform both pointed and mapping observations of the ground state $J = 1 \rightarrow 0$ rotational transitions of CO, ^{13}CO, N_2H^+, HCN, H^{13}CN, HCO$^+$, H^{13}CO$^+$, HNC and HN^{13}C toward M8 E. Using LTE and non-LTE methods we determined the warm and cold gas temperatures to be $\sim$ 50 and 30 K respectively and volume densities were obtained in the range of $\sim$ 10^4–10^6 cm^{-3}. We presented a comparison between M8 and M8 E based on the abundances of the analysed species and we find that more densely embedded star formation is taking place in M8 E. Furthermore, owing to the differences seen in the observed abundances in M8 and M8 E, we favour the $J = 1 \rightarrow 0$ transition of N_2H^+ over HCN and HCO$^+$ in probing high density, cold and and relatively young star-forming regions. On the contrary, HCN and HCO$^+$ probe high density gas in warmer regions.

6.1.1 Overview

We successfully identified different evolutionary stages of massive star formation in M8. We did a multi-wavelength study using the best observing facilities in the world (HST, WISE, APEX, IRAM 30 m, SOFIA telescopes) to study the PDR of M8 in detail. Unlike the well-studied Orion Bar (Hogerheijde et al., 1995) and the PDR of M17 (Pérez-Beaupuits et al., 2015), M8 has a face on geometry with the warm PDR layer in front of the bright stellar system, which is close to its natal molecular cloud in the background. PDRs like M8 and the Orion Bar are among the highest UV-flux PDRs so far studied in our galaxy with very similar physical conditions. Combining the results from this thesis to our previous knowledge regarding the formation processes of small hydrocarbons in PDRs, we found gas-phase chemistry to be responsible for the observed hydrocarbon abundances in high-UV flux PDRs. On the contrary, fragmentation of PAHs in PDRs could be responsible for the higher abundance of hydrocarbons observed in low-UV flux PDRs like the Horsehead Nebula (Teyssier et al., 2004). Lastly, in our classification of diffuse and dense gas tracers while studying the embedded star-forming region of M8 E, we find the $J = 1 \rightarrow 0$ transition of N_2H^+ to be a better probe (similar to Kauffmann et al. 2017 and Pety et al. 2017) of cold high density gas in star-forming regions, in contrast to the same transition of HCN and HCO$^+$, which trace dense gas

in warmer regions.

6.2 Outlook

The results we obtained from the research work presented in this thesis allowed us to understand the ISM in the vicinity of bright hot stars better. But despite the progress we made, there are new interesting questions that were raised and we look forward to addressing them in the future. Two interesting follow-up projects to the science reported in chapters 3 and 4 are:

- What is the role of [O I] in tracing dense PDRs? Cooling in PDRs occurs mainly through fine-structure lines of the abundant atoms and ions. The PDR model calculations for different densities predict that at low densities ($< 10^4$ cm^{-3}) and FUV radiation field G_0 ($< 10^4$, in Habing units), [C II] is the dominant cooling line while at high densities ($> 10^4$ cm^{-3}) and G_0 ($> 10^4$, in Habing units) when temperature exceeds 100 K, the [O I] 63 μm and 145 μm fine structure lines becomes the major cooling lines (Hollenbach & Tielens, 1999). Recent studies on the Orion Bar report that [O I] alone is responsible for 72% of the power emitted by the main cooling lines (H, CO, [C II]) in a PDR (Bernard-Salas et al., 2012), making [O I] very important in determining the complete cooling budget in a PDR. We believe that if observed with high spectral resolution, [O I] can also trace the dense gas structure of a PDR. In chapter 3, we have used [C II] and various CO transitions to characterize the PDR of M8, which is a high UV flux PDR with $G_0 \sim 10^5$ (in Habing units) and $n(\mathrm{H_2}) \sim 10^4$–$10^6$ cm^{-3}. However, we still need [O I] observations to complete our study of the PDR of M8. We plan to observe [O I] 63 μm and 145 μm with the SOFIA telescope to determine the total cooling budget and to probe the dense gas structures in M8.

- Observational study of the embedded star-forming region of M8 E: In chapter 5, we presented the 3 mm wavelength data observed with IRAM 30 m telescope toward M8 E. We were able to estimate the gas temperatures and column densities of various observed species. But in order to constrain the physical conditions better, we need multiple transitions of the species observed with IRAM 30 m telescope. For this, we will propose to observe higher rotational transitions with the APEX telescope to have a better grasp of the physical parameters of the gas in M8 E.

Appendix A

Appendix to chapter 3

Contents

A.1 [C II] column density

For optically thin, thermalized [C II] emission and neglecting the effects from the background, the observed antenna temperature is found to be:

$$T_{\rm A}^{*} = 3.43 \times 10^{-16} \left[1 + 0.5e^{91.25/T_{\rm kin}}\right]^{-1} \frac{N([\text{C II}]\ )}{\delta v}\ \text{K}, \tag{A.1}$$

where $T_{\rm kin}$ is the kinetic temperature, $N([\text{C II}]\ )$ is [C II] column density in cm^{-2} and δv is the line width in km s^{-1}.

Appendix B

Appendix to chapter 4

Contents

B.1 Identified lines of hydrocarbons

Table B.1: Line intensities of the observed hfs transitions of C_2H line taken from CDMS.

Transition	Frequency	S_{ij} [a]	T_{mb} [b]	Relative Intensities	
$(J,F)_{N=p+1} \rightarrow (J,F)_{N=p}$	GHz		K	LTE[c]	Obs.[d]
C_2H $N = 1 - 0$ with IRAM 30m/EMIR					
(3/2,1) → (1/2,1)	87.284	0.17	0.16	0.042	0.055
(3/2,2) → (1/2,1)	87.316	1.67	1.10	0.416	0.392
(3/2,1) → (1/2,0)	87.328	0.83	0.57	0.207	0.204
(1/2,1) → (1/2,1)	87.401	0.83	0.58	0.208	0.208
(1/2,0) → (1/2,1)	87.407	0.33	0.25	0.083	0.088
(1/2,1) → (1/2,0)	87.446	0.17	0.15	0.042	0.052
C_2H $N = 3 - 2$ with APEX/PI230					
(7/2,3) → (5/2,3)	261.978	0.110	0.006	0.009	0.013
(7/2,4) → (5/2,3)	262.004	3.857	1.45	0.321	0.290
(7/2,3) → (5/2,2)	262.006	2.886	1.37	0.240	0.270
(5/2,3) → (3/2,2)	262.064	2.755	1.00	0.230	0.197
(5/2,2) → (3/2,1)	262.067	1.800	0.948	0.150	0.186
(5/2,2) → (3/2,2)	262.078	0.242	0.102	0.020	0.020
(5/2,3) → (5/2,3)	262.208	0.223	0.123	0.019	0.024
(5/2,2) → (5/2,2)	262.250	0.091	0.005	0.008	0.010
C_2H $N = 5 - 4$ with APEX/FLASH$^+$					
(11/2,6) → (9/2,5)	436.661	5.910	0.8	0.298	0.296
(11/2,5) → (9/2,4)	436.662	4.921	0.7	0.248	0.259
(9/2,5) → (7/2,4)	436.723	4.837	0.665	0.245	0.246
(9/2,4) → (7/2,3)	436.724	3.890	0.535	0.196	0.198

[a] Theoretical line strengths.
[b] Observed main beam temperatures.
[c] $S_{ij}/\sum S_{ij}$, assuming optically thin transitions ($\tau < 1$).
[d] $T_{mb_{ij}}/\sum T_{mb_{ij}}$.

B.2 Spatial distribution of [C I] and CO $J = 6 \rightarrow 5$ relative to C_2H $N = 1 \rightarrow 0$

As shown in Fig. B.1, [C I] emission (in color) peaks close to Her 36 and has a bright extended emission toward the north west of it. This extended emission is also traced by CO $J = 6 \rightarrow 5$ emission (white contours) as well as by C_2H $N = 1 \rightarrow 0$ emission (black contours).

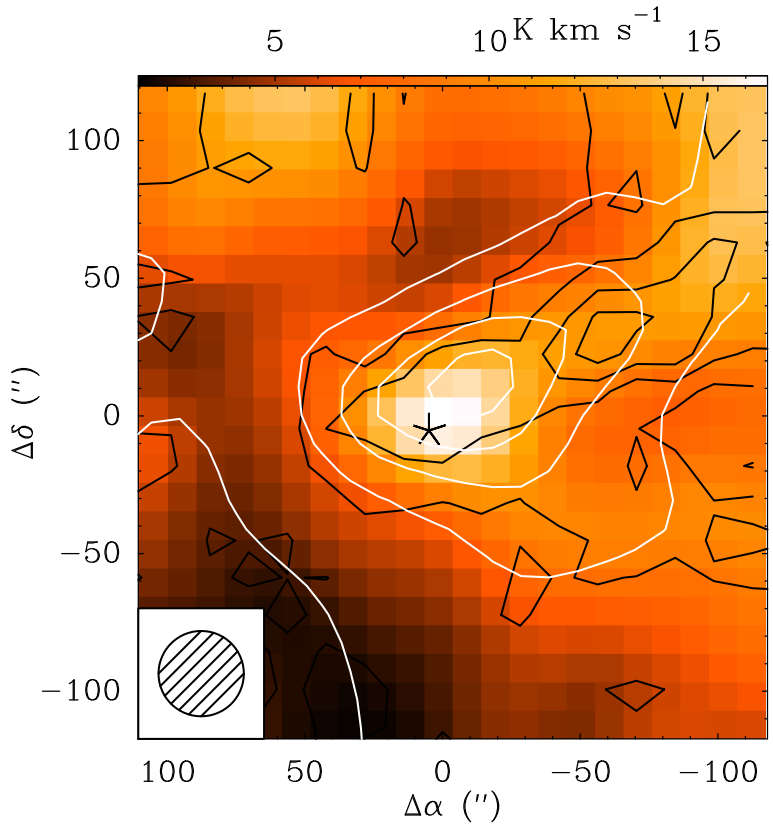

Figure B.1: Color map of velocity integrated intensity of the [C I] 609 μm line overlaid with velocity integrated intensity map contours of C_2H (in black) and CO $J = 6 \rightarrow 5$ (in white). Her 36 is the central position ($\Delta\alpha = 0$, $\Delta\delta = 0$) at R.A.(J2000) = $18^h03^m40.3^s$ and Dec.(J2000) = –24°22′43″, marked with an asterisk. For both C_2H and CO $J = 6 \rightarrow 5$, the contour levels are 10% to 100% in steps of 20% of the peak emission. All maps were convolved to the same resolution of 30″.

B.3 PDR modeling results for Orion Bar conditions

To investigate the different c-C_3H_2 column density values obtained by our PDR models (Meijerink & Spaans, 2005) for M8 and by the Meudon code for the Orion Bar, we ran our models using the same input parameters as Cuadrado et al. (2015, Fig. 17, right panel) for their high density clump ($n_H = 4 \times 10^6$ cm^{-3} and $G_0 = 1.17 \times 10^4$). The

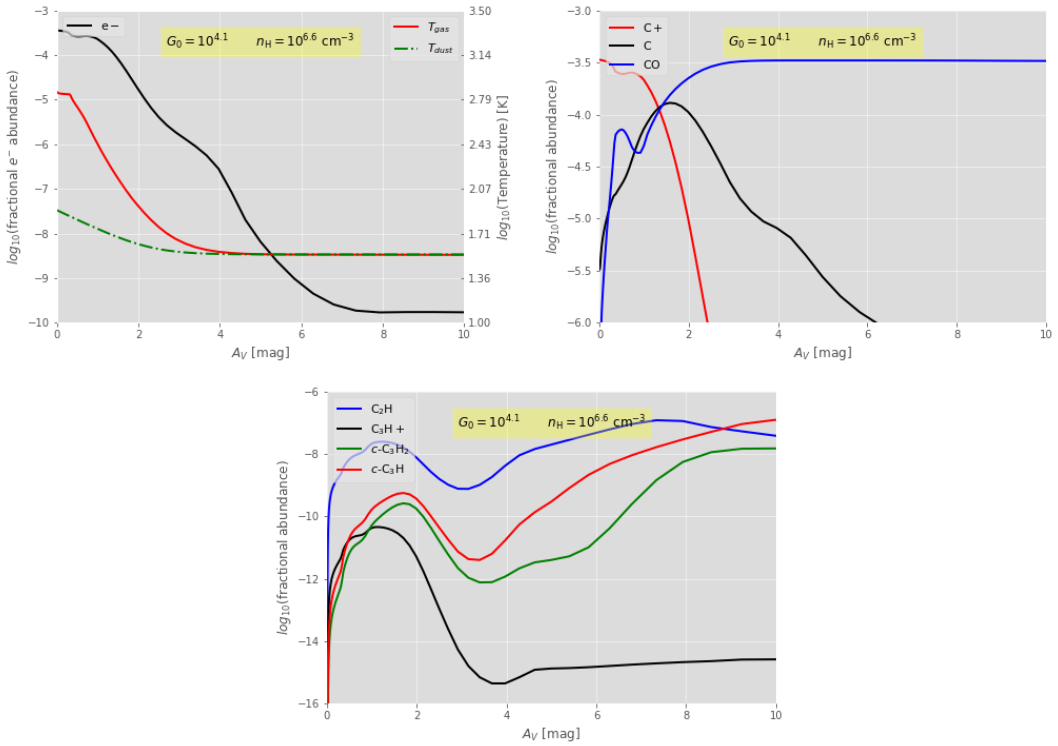

Figure B.2: Results of our PDR modeling for a high density clump in the Orion Bar ($n_{\rm H} = 4 \times 10^6$ cm^{-3} and $G_0 = 1.17 \times 10^4$). In all panels, the abscissa gives visual extinction. The top panel shows the dependence of the electron abundance (black solid line/ left ordinate), gas temperature (red solid line/ right ordinate), and dust temperature (red line, green dash-dot/ right ordinate). The middle panel plots the fractional abundances of ionized and neutral carbon and CO as red, black, and blue lines, respectively. The bottom panel plots the fractional abundances of C_2H, C_2H^+, c-C_3H_2, and c-C_3H as ionized and neutral carbon and CO as blue, black, green, and red lines, respectively.

modeling results are presented in Fig. B.2. Clearly our models do not produce the same results as the Meudon code (Cuadrado et al., 2015, Fig. 17, right panel). The differences in both models lie in the initial abundances of various species, in their evolution profiles, and in the temperature profiles throughout the slab ($A_v = 0$ to 10). Differences may arise due to distinct chemical networks used in both models. The Meudon code run by Cuadrado et al. (2015) uses a total of 130 species and 2800 gas-phase reactions. The Meijerink & Spaans (2005) model, on the other hand, uses a total of 309 species and 4453 gas-phase reactions. The different initial abundances of the neutral and ionized carbon at the edge ($A_v = 0$) of our PDR model and that of the Meudon code may also contribute to the higher column density prediction of c-C_3H_2. Furthermore, it is worth mentioning that the Meudon code includes the updated state-to-state reactions of vibrationally excited H_2 with [C II], [O I], OH (Agúndez et al., 2010). It has also

upgraded the carbon-bearing species network and used the most recent branching ratios for ion-molecule, neutral-neutral, dissociative recombination, and charge exchange reactions for carbon chains and hydrocarbon species as described in Chabot et al. (2013). These updates are missing in our PDR models. The actual impact of these exchange reactions cannot be measured until the PDR model by Meijerink & Spaans (2005) is updated.

Bibliography

Agúndez M., Cernicharo J., Guélin M., 2010, ApJ, 724, L133 (Cited on page 103.)

Agúndez M., Goicoechea J. R., Cernicharo J., Faure A., Roueff E., 2010, ApJ, 713, 662 (Cited on page 9.)

Anderson L. D., Armentrout W. P., Johnstone B. M., Bania T. M., Balser D. S., Wenger T. V., Cunningham V., 2015, ApJS, 221, 26 (Cited on pages 5 and 7.)

Anderson L. D., Bania T. M., 2009, ApJ, 690, 706 (Cited on page 6.)

Anderson L. D., Bania T. M., Balser D. S., Cunningham V., Wenger T. V., Johnstone B. M., Armentrout W. P., 2014, ApJS, 212, 1 (Cited on pages 5 and 85.)

Anderson L. D., Bania T. M., Balser D. S., Rood R. T., 2011, ApJS, 194, 32 (Cited on pages 6 and 7.)

Andree-Labsch S., Ossenkopf-Okada V., Röllig M., 2017, A&A, 598, A2 (Cited on pages 54 and 77.)

Arias J. I., Barbá R. H., Gamen R. C., Morrell N. I., Maíz Apellániz J., Alfaro E. J., Sota A., Walborn N. R., Moni Bidin C., 2010, ApJ, 710, L30 (Cited on page 12.)

Arias J. I., Barbá R. H., Gamen R. C., Morrell N. I., Maíz Apellániz J., Alfaro E. J., Sota A., Walborn N. R., Moni Bidin C., 2010, ApJ, 710, L30 (Cited on pages 28 and 59.)

Arias J. I., Barbá R. H., Maíz Apellániz J., Morrell N. I., Rubio M., 2006, MNRAS, 366, 739 (Cited on pages 30, 58, 59 and 81.)

Arias J. I., Barbá R. H., Maíz Apellániz J., Morrell N. I., Rubio M., 2006, MNRAS, 366, 739 (Cited on pages 10 and 28.)

Bania T. M., Anderson L. D., Balser D. S., Rood R. T., 2010, ApJ, 718, L106 (Cited on pages 6 and 85.)

Battersby C., Ginsburg A., Bally J., Longmore S., Dunham M., Darling J., 2014, ApJ, 787, 113 (Cited on page 3.)

Beichman C. A., 1988, Astrophysical Letters and Communications, 27, 67 (Cited on page 6.)

Belloche A., Müller H. S. P., Garrod R. T., Menten K. M., 2016, A&A, 587, A91 (Cited on page 4.)

Beltrán M. T., Brand J., Cesaroni R., Fontani F., Pezzuto S., Testi L., Molinari S., 2006, A&A, 447, 221 (Cited on page 82.)

Benjamin R. A., Churchwell E., Babler B. L., Bania T. M., Clemens D. P., Cohen M., Dickey J. M., Indebetouw R., Jackson J. M., 2003, PASP, 115, 953 (Cited on pages 7 and 66.)

Bergin E. A., Goldsmith P. F., Snell R. L., Ungerechts H., 1994, ApJ, 431, 674 (Cited on page 89.)

Bernard-Salas J., Habart E., Arab H., Abergel A., Dartois E., Martin P., 2012, A&A, 538, A37 (Cited on page 97.)

Beuther H., Bihr S., Rugel M., Johnston K., Wang Y., Walter F., Brunthaler A., Walsh A. J., Ott J., Stil J., Henning T., Schierhuber T., 2016, Astronomy and Astrophysics, 595, A32 (Cited on page 6.)

Beuther H., Semenov D., Henning T., Linz H., 2008, ApJ, 675, L33 (Cited on page 58.)

Beuther H., Zhang Q., Bergin E. A., Sridharan T. K., 2009, AJ, 137, 406 (Cited on page 4.)

Bok B. J., Reilly E. F., 1947, The Astrophysical Journal, 105, 255 (Cited on page 15.)

Bron E., Le Bourlot J., Le Petit F., 2014, A&A, 569, A100 (Cited on page 24.)

Bron E., Le Petit F., Le Bourlot J., 2016, A&A, 588, A27 (Cited on page 24.)

Bronfman L., Casassus S., May J., Nyman L. Å., 2000, Astronomy and Astrophysics, 358, 521 (Cited on page 2.)

Burton M. G., 2002, PASA, 19, 260 (Cited on page 29.)

Burton M. G., Hollenbach D. J., Tielens A. G. G. M., 1990, ApJ, 365, 620 (Cited on page 9.)

Carey S. J., Noriega-Crespo A., Mizuno D. R., Shenoy S., Paladini R., Kraemer K. E., Price S. D., Flagey N., 2009, PASP, 121, 76 (Cited on page 85.)

Carey S. J., Noriega-Crespo A., Mizuno D. R., Shenoy S., Paladini R., Kraemer K. E., Price S. D., Flagey N., Ryan E., Ingalls J. G., 2009, PASP, 121, 76 (Cited on page 7.)

Carilli C. L., Walter F., 2013, ARA&A, 51, 105 (Cited on page 49.)

Carter M., Lazareff B., Maier D., Chenu J.-Y., Fontana A.-L., Bortolotti Y., Boucher C., Navarrini A., Blanchet S., Greve A., John D., Kramer C., Morel F., Navarro S., Peñalver J., Schuster K. F., Thum C., 2012, A&A, 538, A89 (Cited on pages 35, 62 and 82.)

Chabot M., Béroff K., Gratier P., Jallat A., Wakelam V., 2013, ApJ, 771, 90 (Cited on page 104.)

Chandra S., Kegel W. H., 2000, , 142, 113 (Cited on pages 60 and 72.)

Chen L., de Grijs R., Zhao J. L., 2007, AJ, 134, 1368 (Cited on pages 12 and 28.)

Csengeri T., Bontemps S., Wyrowski F., Belloche A., Menten K. M., Leurini S., Beuther H., Bronfman L., Commerçon B., Chapillon E., Longmore S., Palau A., Tan J. C., Urquhart J. S., 2018, A&A, 617, A89 (Cited on page 4.)

Cuadrado S., Goicoechea J. R., Cernicharo J., Fuente A., Pety J., Tercero B., 2017, A&A, 603, A124 (Cited on pages 10 and 23.)

Cuadrado S., Goicoechea J. R., Pilleri P., Cernicharo J., Fuente A., Joblin C., 2015, A&A, 575, A82 (Cited on pages 10, 58, 62, 65, 69, 77, 78, 102 and 103.)

Dahlstrom J., York D. G., Welty D. E., Oka T., Hobbs L. M., Johnson S., Friedman S. D., Jiang Z., Rachford B. L., Sherman R., Snow T. P., Sonnentrucker P., 2013, ApJ, 773, 41 (Cited on pages 29 and 59.)

Dame T. M., Hartmann D., Thaddeus P., 2001, ApJ, 547, 792 (Cited on page 85.)

Damiani F., Bonito R., Prisinzano L., Zwitter T., Bayo A., Kalari V., Jiménez-Esteban F. M., Costado M. T., Jofré P., Randich S., Flaccomio E., Lanzafame A. C., Lardo C., Morbidelli L., Zaggia S., 2017, A&A, 604, A135 (Cited on pages 30, 53 and 59.)

Damiani F., Flaccomio E., Micela G., Sciortino S., Harnden Jr. F. R., Murray S. S., 2004, ApJ, 608, 781 (Cited on pages 28, 30, 58, 59 and 81.)

Damiani F., Flaccomio E., Micela G., Sciortino S., Harnden F. R. J., Murray S. S., 2004, ApJ, 608, 781 (Cited on page 10.)

Daniel F., Dubernet M. L., Meuwly M., Cernicharo J., Pagani L., 2005, MNRAS, 363, 1083 (Cited on page 92.)

Dobbs C. L., 2008, MNRAS, 391, 844 (Cited on page 2.)

Downes D., Wilson T. L., Bieging J., Wink J., 1980, , 40, 379 (Cited on page 6.)

Draine B. T., 1978, ApJS, 36, 595 (Cited on page 24.)

Draine B. T., 2003, ARA&A, 41, 241 (Cited on page 23.)

Draine B. T., 2011, Physics of the Interstellar and Intergalactic Medium (Cited on pages 18 and 42.)

Dumouchel F., Faure A., Lique F., 2010, MNRAS, 406, 2488 (Cited on page 92.)

Esteban C., Peimbert M., Torres-Peimbert S., García-Rojas J., Rodríguez M., 1999, ApJS, 120, 113 (Cited on pages 54 and 73.)

Fallscheer C., Beuther H., Zhang Q., Keto E., Sridharan T. K., 2009, A&A, 504, 127 (Cited on page 3.)

Flower D. R., 1999, MNRAS, 305, 651 (Cited on page 92.)

Fontani F., Cesaroni R., Caselli P., Olmi L., 2002, A&A, 389, 603 (Cited on page 89.)

Fuente A., Rodriguez-Franco A., Martin-Pintado J., 1996, A&A, 312, 599 (Cited on page 10.)

Gerin M., Kaźmierczak M., Jastrzebska M., Falgarone E., Hily-Blant P., Godard B., de Luca M., 2011, A&A, 525, A116 (Cited on page 58.)

Giannetti A., Leurini S., Wyrowski F., Urquhart J., Csengeri T., Menten K. M., König C., Güsten R., 2017, A&A, 603, A33 (Cited on pages 89, 90 and 91.)

Ginsburg A., Glenn J., Rosolowsky E., Ellsworth-Bowers T. P., Battersby C., Dunham M., Merello M., Shirley Y., Bally J., Evans II N. J., Stringfellow G., Aguirre J., 2013, ApJS, 208, 14 (Cited on page 3.)

Goicoechea J. R., Le Bourlot J., 2007, A&A, 467, 1 (Cited on page 24.)

Goicoechea J. R., Pety J., Cuadrado S., Cernicharo J., Chapillon E., 2016, Nature, 537, 207 (Cited on page 8.)

Goicoechea J. R., Teyssier D., Etxaluze M., Goldsmith P. F., Ossenkopf V., Gerin M., Bergin E. A., Black J. H., Cernicharo J., Cuadrado S., Encrenaz P., 2015, ApJ, 812, 75 (Cited on page 54.)

Goldsmith P. F., Langer W. D., 1999, ApJ, 517, 209 (Cited on pages 18, 21, 45, 69 and 71.)

Gonzalez Garcia M., Le Bourlot J., Le Petit F., Roueff E., 2008, A&A, 485, 127 (Cited on page 24.)

Goto M., Stecklum B., Linz H., Feldt M., Henning T., Pascucci I., Usuda T., 2006, ApJ, 649, 299 (Cited on pages 28, 29, 30 and 59.)

Gratier P., Pety J., Guzmán V., Gerin M., Goicoechea J. R., Roueff E., Faure A., 2013, A&A, 557, A101 (Cited on page 10.)

Griffin M. J., Abergel A., Abreu A., Ade P. A. R., André P., Augueres J.-L., Babbedge T., Bae Y., Baillie T., Baluteau J.-P., Barlow M. J., 2010, A&A, 518, L3 (Cited on page 67.)

Guan X., Stutzki J., Graf U. U., Güsten R., Okada Y., Requena-Torres M. A., Simon R., Wiesemeyer H., 2012, A&A, 542, L4 (Cited on page 32.)

Güsten R., Nyman L. Å., Schilke P., Menten K., Cesarsky C., Booth R., 2006, A&A, 454, L13 (Cited on pages 32 and 59.)

Güver T., Özel F., 2009, MNRAS, 400, 2050 (Cited on page 73.)

Guzmán V. V., Pety J., Gratier P., Goicoechea J. R., Gerin M., Roueff E., Le Petit F., Le Bourlot J., 2014, Faraday Discussions, 168, 103 (Cited on page 10.)

Habing H. J., 1968, Bull. Astron. Inst. Netherlands, 19, 421 (Cited on page 24.)

Habing H. J., 1969, Bull. Astron. Inst. Netherlands, 20, 177 (Cited on page 58.)

Herbst E., van Dishoeck E. F., 2009, ARA&A, 47, 427 (Cited on page 4.)

Hernández Vera M., Lique F., Dumouchel F., Hily-Blant P., Faure A., 2017, MNRAS, 468, 1084 (Cited on page 92.)

Heyminck S., Graf U. U., Güsten R., Stutzki J., Hübers H. W., Hartogh P., 2012, A&A, 542, L1 (Cited on page 30.)

Hogerheijde M. R., Jansen D. J., van Dishoeck E. F., 1995, Submm Observations of Molecular Lines in the Orion Bar: Towards a Physical Model. p. 201 (Cited on pages 9, 54, 77 and 96.)

Hoglund B., Mezger P. G., 1965, Science, 150, 339 (Cited on page 6.)

Hollenbach D., Salpeter E. E., 1971, ApJ, 163, 155 (Cited on page 22.)

Hollenbach D. J., Tielens A. G. G. M., 1997, ARA&A, 35, 179 (Cited on pages 53, 54 and 77.)

Hollenbach D. J., Tielens A. G. G. M., 1999, Reviews of Modern Physics, 71, 173 (Cited on pages 4, 7, 8, 9, 28, 54, 81 and 97.)

Hughes V. A., MacLeod G. C., 1989, AJ, 97, 786 (Cited on page 6.)

Jansen D. J., Spaans M., Hogerheijde M. R., van Dishoeck E. F., 1995, A&A, 303, 541 (Cited on pages 10 and 54.)

Joblin C., Bron E., Pinto C., Pilleri P., Le Petit F., Gerin M., Le Bourlot J., Fuente A., 2018, A&A, 615, A129 (Cited on page 77.)

Kauffmann J., Bertoldi F., Bourke T. L., Evans II N. J., Lee C. W., 2008, A&A, 487, 993 (Cited on page 53.)

Kauffmann J., Goldsmith P. F., Melnick G., Tolls V., Guzman A., Menten K. M., 2017, A&A, 605, L5 (Cited on pages 83, 94 and 96.)

Kennicutt R. C., 2005, in Cesaroni R., Felli M., Churchwell E., Walmsley M., eds, Massive Star Birth: A Crossroads of Astrophysics Vol. 227 of IAU Symposium, The role of massive stars in astrophysics. pp 3–11 (Cited on page 2.)

Keto E., Zhang Q., Kurtz S., 2008, The Astrophysical Journal, 672, 423 (Cited on page 5.)

Kim C.-G., Ostriker E. C., Kim W.-T., 2013, ApJ, 776, 1 (Cited on pages 2 and 81.)

Kippenhahn R., Weigert A., Weiss A., 2012, Stellar Structure and Evolution (Cited on page 1.)

Klein B., Hochgürtel S., Krämer I., Bell A., Meyer K., Güsten R., 2012, A&A, 542, L3 (Cited on page 32.)

Kraus J. D., 1966, Radio astronomy (Cited on page 19.)

Kurtz S., Franco J., 2002, in Henney W. J., Franco J., Martos M., eds, Revista Mexicana de Astronomia y Astrofisica Conference Series Vol. 12, Ultracompact H II Regions. pp 16–21 (Cited on page 4.)

Lada C. J., Gottlieb C. A., Gottlieb E. W., Gull T. R., 1976, ApJ, 203, 159 (Cited on pages 28 and 30.)

Le Bourlot J., Le Petit F., Pinto C., Roueff E., Roy F., 2012, A&A, 541, A76 (Cited on pages 10, 22 and 23.)

Le Bourlot J., Pineau Des Forets G., Roueff E., Flower D. R., 1993, A&A, 267, 233 (Cited on page 24.)

Le Page V., Snow T. P., Bierbaum V. M., 2003, ApJ, 584, 316 (Cited on page 58.)

Le Petit F., Barzel B., Biham O., Roueff E., Le Bourlot J., 2009, A&A, 505, 1153 (Cited on page 24.)

Le Petit F., Nehmé C., Le Bourlot J., Roueff E., 2006, ApJS, 164, 506 (Cited on pages 10, 23 and 24.)

Linz H., Henning T., Stecklum B., Men'shchikov A., van Boekel R., Follert R., Feldt M., 2008, in Beuther H., Linz H., Henning T., eds, Massive Star Formation: Observations Confront Theory Vol. 387 of Astronomical Society of the Pacific Conference Series, Dissecting Massive YSOs with Mid-Infrared Interferometry. p. 132 (Cited on page 12.)

Linz H., Stecklum B., Follert R., Henning T., van Boekel R., Men'shchikov A., Pascucci I., Feldt M., 2008, in Journal of Physics Conference Series Vol. 131 of Journal of Physics Conference Series, Mid-infrared interferometry of massive young stellar objects. p. 012024 (Cited on page 82.)

Lockman F. J., 1989, ApJS, 71, 469 (Cited on page 6.)

Lockman F. J., Pisano D. J., Howard G. J., 1996, ApJ, 472, 173 (Cited on page 6.)

Lucas R., Liszt H. S., 2000, A&A, 358, 1069 (Cited on page 58.)

Lynds B. T., Oneil Jr. E. J., 1982, ApJ, 263, 130 (Cited on page 30.)

Mangum J. G., Shirley Y. L., 2015, PASP, 127, 266 (Cited on pages 18 and 88.)

Mangum J. G., Shirley Y. L., 2016, PASP, 128, 029201 (Cited on page 42.)

Maret S., Hily-Blant P., Pety J., Bardeau S., Reynier E., 2011, A&A, 526, A47 (Cited on page 89.)

Masqué J. M., Dzib S., Rodríguez L. F., 2014, ApJ, 797, 60 (Cited on page 28.)

Matthews H. E., Irvine W. M., 1985, ApJ, 298, L61 (Cited on page 64.)

Meijerink R., Spaans M., 2005, A&A, 436, 397 (Cited on pages 23, 24, 73, 78, 102, 103 and 104.)

Milam S. N., Savage C., Brewster M. A., Ziurys L. M., Wyckoff S., 2005, ApJ, 634, 1126 (Cited on pages 45, 49 and 88.)

Mitchell G. F., Hasegawa T. I., Schella J., 1992, ApJ, 386, 604 (Cited on page 85.)

Molinari S., Brand J., Cesaroni R., Palla F., 1996, A&A, 308, 573 (Cited on page 91.)

Molinari S., Swinyard B., Bally J., Barlow M., Bernard J. P., Martin P., Moore T., Noriega-Crespo A., Plume R., Testi L., 2010, PASP, 122, 314 (Cited on page 3.)

Montillaud J., Joblin C., Toublanc D., 2013, A&A, 552, A15 (Cited on page 58.)

Nagy Z., Ossenkopf V., Van der Tak F. F. S., Faure A., Makai Z., Bergin E. A., 2015, A&A, 578, A124 (Cited on pages 58 and 77.)

Nakamura F., Oyamada S., Okumura S., Ishii S., Shimajiri Y., Tanabe Y., Tsukagoshi T., Kawabe R., Momose M., Urasawa Y., 2019, PASJ, p. 32 (Cited on page 83.)

Oka T., Welty D. E., Johnson S., York D. G., Dahlstrom J., Hobbs L., 2014, ApJ, 793, 68 (Cited on pages 29 and 59.)

Pabst C. H. M., Goicoechea J. R., Teyssier D., Berné O., Ochsendorf B. B., Wolfire M. G., Higgins R. D., Riquelme D., Risacher C., Pety J., Le Petit F., Roueff E., Bron E., Tielens A. G. G. M., 2017, A&A, 606, A29 (Cited on page 28.)

Patil A., Huard D., Fonnesbeck C., 2010, Journal of Statistical Software, Articles, 35, 1 (Cited on page 89.)

Peng T.-C., 2010, PhD thesis, Universitat Bonn (Cited on page 21.)

Peng T.-C., Wyrowski F., Zapata L. A., Güsten R., Menten K. M., 2012, A&A, 538, A12 (Cited on pages 42, 49, 53, 77 and 88.)

Pérez-Beaupuits J. P., Güsten R., Spaans M., Ossenkopf V., Menten K. M., Requena-Torres M. A., Stutzki J., Wiesemeyer H., Guevara C., 2015, in EAS Publications Series Vol. 75 of EAS Publications Series, Excitation conditions and energetics of the dense gas in M17 SW. pp 205–206 (Cited on page 55.)

Pérez-Beaupuits J. P., Güsten R., Spaans M., Ossenkopf V., Menten K. M., Requena-Torres M. A., Wiesemeyer H., Stutzki J., Guevara C., Simon R., 2015, A&A, 583, A107 (Cited on page 55.)

Pérez-Beaupuits J. P., Spaans M., Hogerheijde M. R., Güsten R., Baryshev A., Boland W., 2010, A&A, 510, A87 (Cited on page 55.)

Pérez-Beaupuits J. P., Stutzki J., Ossenkopf V., Spaans M., Güsten R., Wiesemeyer H., 2015, A&A, 575, A9 (Cited on pages 37, 40, 42 and 96.)

Pérez-Beaupuits J. P., Wiesemeyer H., Ossenkopf V., Stutzki J., 2012, Astronomy and Astrophysics, 542, L13 (Cited on page 9.)

Pety J., Guzmán V. V., Orkisz J. H., Liszt H. S., Gerin M., Bron E., Bardeau S., Goicoechea J. R., Gratier P., Le Petit F., 2017, A&A, 599, A98 (Cited on pages 83, 91, 94 and 96.)

Pety J., Teyssier D., Fossé D., Gerin M., Roueff E., Abergel A., Habart E., Cernicharo J., 2005, A&A, 435, 885 (Cited on pages 23 and 58.)

Phillips J. P., Ramos-Larios G., 2008, MNRAS, 391, 1527 (Cited on page 5.)

Pilbratt G. L., Riedinger J. R., Passvogel T., Crone G., Doyle D., Gageur U., Heras A. M., Jewell C., Metcalfe L., Ott S., Schmidt M., 2010, A&A, 518, L1 (Cited on page 67.)

Povich M. S., Churchwell E., Bieging J. H., Kang M., Whitney B. A., Brogan C. L., Kulesa C. A., Cohen M., Babler B. L., Indebetouw R., Meade M. R., Robitaille T. P., 2009, ApJ, 696, 1278 (Cited on page 55.)

Pratap P., Dickens J. E., Snell R. L., Miralles M. P., Bergin E. A., Irvine W. M., Schloerb F. P., 1997, ApJ, 486, 862 (Cited on page 58.)

Rathborne J. M., Jackson J. M., Simon R., 2006, ApJ, 641, 389 (Cited on page 3.)

Rauw G., Nazé Y., Gosset E., Stevens I. R., Blomme R., Corcoran M. F., Pittard J. M., Runacres M. C., 2002, A&A, 395, 499 (Cited on page 29.)

Rauw G., Sana H., Spano M., Gosset E., Mahy L., De Becker M., Eenens P., 2012, A&A, 542, A95 (Cited on pages 12, 29 and 59.)

Reifenstein E. C., Wilson T. L., Burke B. F., Mezger P. G., Altenhoff W. J., 1970, A&A, 4, 357 (Cited on page 6.)

Risacher C., Güsten R., Stutzki J., Hübers H.-W., Bell A., Buchbender C., Büchel D., Csengeri T., Graf U. U., Heyminck S., Higgins R. D., Honingh C. E., 2016, A&A, 595, A34 (Cited on page 30.)

Röllig M., Abel N. P., Bell T., Bensch F., Black J., Ferland G. J., Jonkheid B., Kamp I., Kaufman M. J., Le Bourlot J., Le Petit F., 2007, A&A, 467, 187 (Cited on pages 22 and 23.)

Sanchez-Bermudez J., Alberdi A., Schödel R., Hummel C. A., Arias J. I., Barbá R. H., Maíz Apellániz J., Pott J. U., 2014, A&A, 572, L1 (Cited on page 12.)

Sanchez-Bermudez J., Alberdi A., Schödel R., Hummel C. A., Arias J. I., Barbá R. H., Maíz Apellániz J., Pott J.-U., 2014, A&A, 572, L1 (Cited on pages 28 and 59.)

Schmidt D. R., Ziurys L. M., 2017, ApJ, 850, 123 (Cited on page 58.)

Schöier F. L., van der Tak F. F. S., van Dishoeck E. F., Black J. H., 2005, A&A, 432, 369 (Cited on pages 23, 46, 72 and 92.)

Schuller F., Menten K. M., Contreras Y., Wyrowski F., Schilke P., Bronfman L., Henning T., Walmsley C. M., Beuther H., 2009, A&A, 504, 415 (Cited on pages 3 and 45.)

Shirley Y. L., 2015, PASP, 127, 299 (Cited on page 91.)

Shu F. H., Allen A., Shang H., Ostriker E. C., Li Z.-Y., 1999, in Lada C. J., Kylafis N. D., eds, NATO Advanced Science Institutes (ASI) Series C Vol. 540, Low-Mass Star Formation: Theory. p. 193 (Cited on page 1.)

Simon R., Stutzki J., Sternberg A., Winnewisser G., 1997, A&A, 327, L9 (Cited on page 9.)

Snyder L. E., Buhl D., 1973, Nature Physical Science, 243, 45 (Cited on page 89.)

Solomon P. M., Downes D., Radford S. J. E., Barrett J. W., 1997, ApJ, 478, 144 (Cited on page 49.)

Spezzano S., Tamassia F., Thorwirth S., Thaddeus P., Gottlieb C. A., McCarthy M. C., 2012, ApJS, 200, 1 (Cited on page 64.)

Spielfiedel A., Feautrier N., Najar F., Ben Abdallah D., Dayou F., Senent M. L., Lique F., 2012, MNRAS, 421, 1891 (Cited on pages 60 and 72.)

Stacey G. J., Jaffe D. T., Geis N., Grenzel R., Harris A. I., Poglitsch A., Stutzki J., Townes C. H., 1993, ApJ, 404, 219 (Cited on page 55.)

Stecklum B., Henning T., Eckart A., Howell R. R., Hoare M. G., 1995, ApJ, 445, L153 (Cited on pages 29, 30 and 59.)

Stutzki J., Stacey G. J., Genzel R., Harris A. I., Jaffe D. T., Lugten J. B., 1988, ApJ, 332, 379 (Cited on page 9.)

Tauber J. A., Tielens A. G. G. M., Meixner M., Goldsmith P. F., 1994, ApJ, 422, 136 (Cited on page 54.)

Teyssier D., Fossé D., Gerin M., Pety J., Abergel A., Roueff E., 2004, A&A, 417, 135 (Cited on pages 58 and 96.)

Thaddeus P., Gottlieb C. A., Hjalmarson A., Johansson L. E. B., Irvine W. M., Friberg P., Linke R. A., 1985, ApJ, 294, L49 (Cited on page 64.)

Thiel V., Belloche A., Menten K. M., Giannetti A., Wiesemeyer H., Winkel B., Gratier P., Müller H. S. P., Colombo D., Garrod R. T., 2019, A&A, 623, A68 (Cited on page 90.)

Tielens A. G. G. M., 2008, ARA&A, 46, 289 (Cited on pages 7, 23, 67 and 87.)

Tielens A. G. G. M., 2010, The Physics and Chemistry of the Interstellar Medium (Cited on pages 8, 9, 45, 54, 73 and 88.)

Tielens A. G. G. M., Hollenbach D., 1985, ApJ, 291, 722 (Cited on pages 9, 22, 23, 24, 28, 53, 54 and 58.)

Tielens A. G. G. M., Meixner M. M., van der Werf P. P., Bregman J., Tauber J. A., Stutzki J., Rank D., 1993, Science, 262, 86 (Cited on page 77.)

Tiwari M., Menten K. M., Wyrowski F., Pérez-Beaupuits J. P., Lee M. Y., Kim W. J., 2019, A&A, 626, A28 (Cited on pages 81 and 94.)

Tiwari M., Menten, K. M. Wyrowski, F. Pérez-Beaupuits, J. P. Wiesemeyer, H. Güsten, R. Klein, B. Henkel, C. 2018, A&A, 615, A158 (Cited on pages 58, 59, 61, 62, 66, 67, 69, 71, 73, 75, 77, 81 and 94.)

Tothill N. F. H., Gagné M., Stecklum B., Kenworthy M. A., 2008, The Lagoon Nebula and its Vicinity. p. 533 (Cited on pages 10, 12, 28, 29, 30, 36, 45, 53, 58, 81, 82 and 93.)

Tothill N. F. H., White G. J., Matthews H. E., McCutcheon W. H., McCaughrean M. J., Kenworthy M. A., 2002, ApJ, 580, 285 (Cited on pages 11, 30, 82 and 93.)

Tucker K. D., Kutner M. L., Thaddeus P., 1974, ApJ, 193 (Cited on page 62.)

Turner J. L., Ho P. T. P., Beck S. C., 1998, AJ, 116, 1212 (Cited on page 5.)

Urquhart J. S., König C., Giannetti A., Leurini S., Moore T. J. T., Eden D. J., Pillai T., Thompson M. A., Braiding C., Burton M. G., Csengeri T., Dempsey J. T., Figura C., Froebrich D., Menten K. M., Schuller F., Smith M. D., Wyrowski F., 2018, MNRAS, 473, 1059 (Cited on page 45.)

Urquhart J. S., Thompson M. A., Morgan L. K., Pestalozzi M. R., White G. J., Muna D. N., 2007, A&A, 467, 1125 (Cited on pages 2 and 81.)

van der Tak F. F. S., Black J. H., Schöier F. L., Jansen D. J., van Dishoeck E. F., 2007, A&A, 468, 627 (Cited on pages 46, 71 and 91.)

van der Werf P. P., Goss W. M., O'Dell C. R., 2013, ApJ, 762, 101 (Cited on page 9.)

van der Wiel M. H. D., Jacobsen S. K., Jørgensen J. K., Bourke T. L., Kristensen L. E., Bjerkeli P., Murillo N. M., Calcutt H., Müller H. S. P., Coutens A., Drozdovskaya M. N., Favre C., Wampfler S. F., 2019, A&A, 626, A93 (Cited on page 4.)

van Zadelhoff G. J., Dullemond C. P., van der Tak F. F. S., Yates J. A., Doty S. D., Ossenkopf V., Hogerheijde M. R., Juvela M., Wiesemeyer H., Schöier F. L., 2002, A&A, 395, 373 (Cited on page 24.)

Walmsley C. M., Natta A., Oliva E., Testi L., 2000, A&A, 364, 301 (Cited on pages 53, 54 and 77.)

Watanabe Y., Nishimura Y., Harada N., Sakai N., Shimonishi T., Aikawa Y., Kawamura A., Yamamoto S., 2017, ApJ, 845, 116 (Cited on page 91.)

Westerhout G., 1958, Bull. Astron. Inst. Netherlands, 14, 215 (Cited on page 6.)

White G. J., Nisini B., Correia J. C., Tothill N. F. H., Huldtgren M., Lorenzetti D., Saraceno P., 1998, in Yun J., Liseau L., eds, Star Formation with the Infrared Space Observatory Vol. 132 of Astronomical Society of the Pacific Conference Series, ISO Observations of M8, The Lagoon Nebula. p. 113 (Cited on page 54.)

White G. J., Tothill N. F. H., Matthews H. E., McCutcheon W. H., Huldtgren M., McCaughrean M. J., 1997, A&A, 323, 529 (Cited on pages 12, 29 and 30.)

Wilson T. L., Mezger P. G., Gardner F. F., Milne D. K., 1970, A&A, 6, 364 (Cited on page 6.)

Wood D. O. S., Churchwell E., 1989, ApJS, 69, 831 (Cited on page 6.)

Woodward C. E., Pipher J. L., Helfer H. L., Sharpless S., Moneti A., Kozikowski D., Oliveri M., Willner S. P., Lacasse M. G., Herter T., 1986, AJ, 91, 870 (Cited on pages 28, 30, 37, 40, 53, 54 and 73.)

Woolf N. J., 1961, PASP, 73, 206 (Cited on pages 28 and 58.)

Wright E. L., Eisenhardt P. R. M., Mainzer A. K., Ressler M. E., Cutri R. M., Jarrett T., Kirkpatrick J. D., Padgett D., McMillan R. S., 2010, AJ, 140, 1868 (Cited on page 7.)

Yang B., Stancil P. C., Balakrishnan N., Forrey R. C., 2010, ApJ, 718, 1062 (Cited on page 92.)

York D. G., Dahlstrom J., Welty D. E., Oka T., Hobbs L. M., Johnson S., Friedman S. D., Jiang Z., Rachford B. L., Snow T. P., Sherman R., Sonnentrucker P., 2014, in Cami J., Cox N. L. J., eds, The Diffuse Interstellar Bands Vol. 297 of IAU Symposium, Anomalously Broad Diffuse Interstellar Bands and Excited CH^+ Absorption in the Spectrum of Herschel 36. pp 89–93 (Cited on pages 29 and 59.)

Young E. T., Becklin E. E., Marcum P. M., Roellig T. L., De Buizer J. M., Herter T. L., Güsten R., Dunham E. W., Temi P., Andersson B.-G., 2012, ApJ, 749, L17 (Cited on pages 30 and 59.)

Zhang Q., Hunter T. R., Brand J., Sridharan T. K., Cesaroni R., Molinari S., Wang J., Kramer M., 2005, ApJ, 625, 864 (Cited on page 82.)

Zhang Q., Wang Y., Pillai T., Rathborne J., 2009, ApJ, 696, 268 (Cited on page 4.)

Zinnecker H., Yorke H. W., 2007, ARA&A, 45, 481 (Cited on page 1.)

Zuckerman B., Evans N. J. I., 1974, ApJ, 192, L149 (Cited on page 2.)